2010

Development of a Rigid Body Computational Model for Investigation of Wrist Biomechanics

Benjamin Majors
Virginia Commonwealth University

DEVELOPMENT OF A RIGID BODY COMPUTATIONAL MODEL FOR INVESTIGATION OF WRIST BIOMECHANICS

A Thesis submitted in partial fulfillment of the requirements for the degree of Master of Science in Biomedical Engineering at Virginia Commonwealth University.

By

BENJAMIN JUDSON MAJORS
B.S., Clemson University, 2007

Director: Jennifer S. Wayne, Ph.D.
Department of Biomedical Engineering and Orthopaedic Surgery

Virginia Commonwealth University
Richmond, Virginia
December, 2010

Acknowledgement

There are many people I would like to acknowledge for helping and supporting my work here at VCU. First, and most importantly, I would like to thank my advisor, Dr. Jennifer Wayne, for her time and professional input. Her guidance, support and wisdom have been exceptional. I would also like to acknowledge Dr. Gerald E. Miller and Dr. Jonathan E. Isaacs for taking the time and effort to serve on my committee. I would like to thank Dr. Curtis Hayes and the VCU Department of Radiology for providing the CT scans that were an integral part of this research.

I would also like to thank everyone in the Orthopaedics Research Laboratory, especially those whose research includes computational modeling. Without the guidance and support Kevin Elmore, Joseph Iaquinto, and Edward Sprately, this process would have been much less enjoyable. Thanks are also due to others within the BME program, including Charles Taylor. Additionally, I would like to thank my parents and sisters for their encouragement in my academic endeavors. Finally, I must thank my wife, Tricia. Without her support and understanding, none of this would have been possible, and I owe her the most sincere thank you of all.

Table of Contents

List of Tables

List of Figures

List of Abbreviations

2-D	Two Dimensional
3-D	Three Dimensional
ADAMS	Automatic Dynamic Analysis of Mechanical Systems
ADM	Abductor Digiti Minimi
AP	Anterior-Posterior
APL	Abductor Pollicis Longus
CAD	Computer Aided Design
CH	Capitohamate
CT	Capitotrapezoid
CT	Computed Tomography
DIC	Dorsal Intercarpal
DICOM	Digital Imaging and Communications in Medicine
DP	Distal Pole
DRC	Dorsal Radiocarpal
DRUJ	Distal Radioulnar Joint
ECRB	Extensor Carpi Radialis Brevis
ECRL	Extensor Carpi Radialis Longus
ECU	Extensor Carpi Ulnaris
EDC	Extensor Digitorum Communis
EDQ	Extensor Digiti Quanti
EIP	Extensor Indicis Proprius
EPB	Extensor Pollicis Brevis
EPL	Extensor Pollicis Longus
FCR	Flexor Carpi Radialis
FCU	Flexor Carpi Ulnaris
FR	Flexor Retinaculum
GSTIFF	Gear Stiff Integrator
HM	Hamatometacarpal
HU	Hounsfield Units
IP	Interfacet Prominence
ISB	International Society of Biomechanics
LRL	Long Radiolunate
LT	Lunotriquetral
LVDT	Linearly Variable Displacement Transducer
MIMICS	Materialise's Interactive Medical Imaging Control System
ML	Medial-Lateral
PH	Pisohamate
PM	Pisometacarpal
PT	Pisotriquetral

RBM	Rigid Body Modeling
RC	Radiocapitate
RS	Radioscaphoid
RSC	Radioscaphocapitate
RSL	Radioscapholunate
SC	Scaphocapitate
SL	Scapholunate
SRL	Short Radiolunate
STL	Stereolithography
STT	Scaphotrapeziotrapezoidal
TC	Triquetrocapitate
TFCC	Triangular Fibrocartilage Complex
TH	Triqutrohamate
TT	Trapeziotrapezoidal
UC	Ulnocapitate
UL	Ulnolunate
UT	Ulnotriquetral

Abstract

DEVELOPMENT OF A RIGID BODY COMPUTATIONAL MODEL FOR INVESTIGATION OF WRIST BIOMECHANICS

By Benjamin Judson Majors, B.S.

A Thesis submitted in partial fulfillment of the requirements for the degree of Master of Science in Biomedical Engineering at Virginia Commonwealth University.

Virginia Commonwealth University, 2010

Major Director: Jennifer S. Wayne, Ph.D.
Professor, Biomedical Engineering and Orthopaedic Surgery; Director, Orthopaedic Research Laboratory

The wrist is one of the most complex joints in the human body. As such, the wrist joint is difficult to model due to the number of bones involved and its intricate soft tissue interactions. Many studies have attempted modeling the wrist previously; however, the majority of these studies simplify the joint into two-dimensions or idealized mechanical joints to reduce the complexity of the simulation. While these approaches still yield valuable information, the omission of a third-dimension or geometry defined movements limits the models' usefulness in predicting joint function under non-idealized conditions. Therefore, the goal of this study was to develop a computational model of the wrist joint complex using commercially available software, whereby joint motion and behavior is dictated by highly accurate three-dimensional articular contact, ligamentous constraints, muscle loads, and external perturbations only. As such, a computational model of the human wrist was created using computed tomography (CT) images of a cadaver right upper extremity. Commercially available medical imaging software

and three-dimensional computer aided design (CAD) software were used to reconstruct the osteoarticular surfaces and accurately add soft tissue constraints, as well as calculate kinematic motion simulations. The model was able to reproduce physiologic motion including flexion/extension and radial/ulnar deviation. Validation of the model was achieved by comparing predicted results from the model to the results of a published cadaveric experiment that analyzed wrist function under effects of various surgical procedures. The model was used to replicate the exact testing conditions prescribed for the experiment, and the model was able to accurately reproduce the trends and, in many instances, the magnitudes of the range of motion measurements in the study. Furthermore, the model can now be used to predict the magnitudes for the joint contact forces within the wrist as well as the tension developed in ligaments in hopes locating potential areas of concern after these surgical procedures have been conducted, including further development of arthritis in the wrist and ligament breakdown.

1. INTRODUCTION

1.1 MODELING OF MUSCULOSKELETAL SYSTEMS

Computer simulation techniques for biological systems can be employed to estimate a wide variety of physiologic parameters that may be challenging to obtain experimentally including pressures, strains, and forces. Furthermore, the data obtained can be helpful in explaining the results obtained from motion analyses. These models reduce the need for expensive experiments that sometimes require a large sample size of specimens, and these virtual 3-D models can be easily manipulated to obtain any parameters of interest. Further, once validated, these models have unlimited usability, and they are powerful investigative tools with many real world applications. For musculoskeletal models, these include the design of joint prostheses, preoperative planning of surgical procedures, and understanding the mechanics of injury and pathologies such as degenerative arthritis.

While it is possible to conduct cadaveric studies to measure certain musculoskeletal joint features, these experimental approaches have limitations. Joint kinematic studies can be done by tracking bones in three dimensional space using markers, and joint pressure measurement can be achieved using pressure sensitive film. Ligament tensions and strains can be analyzed by attaching various strain gauges and tensiometers to the native ligament soft tissues. While these techniques offer the benefit of working with natural tissues and provide insightful information, they require invasive disruption of the joint to insert measurement devices that may damage the integrity of the joint. Further, experimental setup for these studies is expensive and time

consuming. Computational models represent an effective alternative to cadaveric studies as they have the advantage of comparing the direct impact of changes to the carpal structure without the complication of difficult changes to the experimentation equipment, and performing changes on the same model geometry permits direct comparison of the alterations. Commonly, biomechanical computational models have been divided into either finite element analysis (FEA) [12,13,16,22,37,38,48,68,83,86] or rigid body modeling. [6,17,24,27,28,30,32,34-36,39,41,43,45,47,48,50-52,61,67,69,74,78,84]

In all computational musculoskeletal models, assumptions and simplifications must be made, and these could potentially affect the accuracy of the results. Often, researchers have constrained joint degrees of freedom (DOF), reduced the model to two dimensions, ignored the contributions of various ligaments, or fused bones together within the joint. Although these simplifications decrease computation time and may be justified in various ways, the native anatomical joint may not always function in the same manner as the simplified joint. [7] By not allowing the osteoarticular geometry and soft tissue constraints alone to govern motion in the model, the model's usefulness to predict joint function in non-idealized motions is limited.

1.2 CURRENT METHODS OF COMPUTATIONAL MODELING

Finite element modeling and rigid body modeling are both current and effective computational methods with different approaches in methodology. Finite element modeling has been applied to estimate stress distributions within bone and cartilage layers in the articulations under static loading conditions. While in rigid body models, the bone structure is represented as rigid bodies, and soft tissue structures are represented as spring elements. Both of these methods, having been applied to a variety of musculoskeletal joints, are effective methods for investigating joint soft tissue function. Further, there are a number of computational software packages available to investigate joint kinematics once a modeling methodology has been chosen.

Finite element analysis has been an effective method for analyzing joint contact areas and stress distributions in human structures such as bone. [13,72] This continuum based numerical analysis technique breaks down the investigated bodies into discrete elements, and assigns material properties at each node. FEA is a widely used and highly valuable research tool, however, there are many limitations regarding its use in analyzing contact problems in human joints, especially in multiple-body contact force analysis such as the wrist, elbow and ankle joints. FEA is sensitive to the values of material properties – many of which are difficult to obtain in biological materials, and often, nonphysiologic constraints have to be implemented to obtain convergence. [13] Additionally, the complexity and many unknowns present in FEA models cause the processing time required to solve very fine meshes to be very large. If the purpose of the analysis is not to find the actual stress inside the cartilage and bone, but only to obtain the kinematics and dynamic biomechanical function of the joint, a simpler approach can be performed. [3] As an alternative to FEA, rigid body models are highly efficient and often converge to a solution considerably faster than the corresponding FEA model. [45]

In rigid body modeling, ligaments span the space between adjacent bones connecting the bones to each other; this is where deformation mainly occurs in joints such as the wrist. In this situation, it can be assumed that the bones are rigid bodies and that the ligaments are linear springs interposed between the rigid bodies. This modeling approach was first developed within the field of civil engineering by Kawai and Takeuchi. [44] Since, the method has been applied to numerous musculoskeletal models. [6,17,24,27,28,30,32,34-36,39,41,43,45,47,48,50-52,61,67,69,74,78,84]

In RBSM, when a load is applied to a musculoskeletal joint, the deformations of the ligaments are much greater than the deformations of the bone and cartilage, therefore the bones can be considered rigid bodies. This assumes that each body is inelastic and incompressible, and such assumptions are appropriate when studying stiff materials with observable stresses that result in less than 1% total strain. [31] A set of equilibrium equations is formulated between the articular surfaces, the spring ligaments, and the external forces. Many of these models constrain joint movement to a smaller number of DOF's to increase computational efficiency. These models idealize the joints and make them much simpler; for example, the knee may be approximated as a simple hinge. The limitation of this approach is apparent in the absence of allowing only the joint geometry and soft tissue to dictate motion. The more realistic and experimentally relevant approach is to allow totally unconstrained motion with no predefined limits on the degrees of freedom in the joint.

Even fewer biomechanical models have been developed where motion is totally controlled by contact between the articular surfaces and soft tissue constraints. While modeling the biomechanics of the knee, Wismans et al [84] were among the first to model a musculoskeletal joint this way. Ligamentous and muscular soft tissues were represented as force

vectors spanning the joint, and cartilaginous soft tissues were not considered. Bony contacts were assumed to be rigid and constant. Other models have followed this methodology for modeling joint motion, and the importance of model validation has been expressed throughout the computational modeling literature. Regardless of the model's assumptions and results, the model should be compared to experimental data before it can be used in a predictive or useful situation. There are many musculoskeletal rigid body models that require underlying computer code to develop and implement. This code is complex, and the models require the programmer to have exceptional knowledge of the model's constituative equations and algorithms. Further, the software is commonly written in house, which makes it difficult to access and utilize outside of the lab where it was created.

There are, however, a small number of rigid body modeling software packages that are capable of investigating the kinematics of musculoskeletal joints. Packages currently being used include SIMM (Software for Interactive Musculoskeletal Modeling, Musculographics Inc., USA), VIMS (Virtual Interactive Musculoskeletal System, BioMed Central Ltd., USA), and MSC ADAMS (Automatic Dynamic Analysis of Mechanical Systems, MSC Software Corp, USA). Each of these modeling software packages are able to solve the equations associated with RBM, but SIMM and VIMS are either limited or unavailable commercially. [14,15]

The SIMM software package does not allow unconstrained joint motion. Instead, function is simplified and joint motion is reduced to idealized mechanical joints with few DOF's. [14] The program has been used to investigate the roles of specific muscles and how they vary under different geometric conditions. [23,40] VIMS does allow full geometry based simulations, but it requires the use of proprietary software packages that are not commercially available at this time. [15] Because both of these programs are limited and/or proprietary, a commercially

available software program is an appealing alternative to SIMM and VIMS. SolidWorks (SolidWorks Corp., Concord, MA) employs the use of an add-in called COSMOSMotion (Structural Research and Analysis Corp, Santa Monica, CA) that provides three-dimensional rigid body dynamics simulation. SolidWorks and COSMOSMotion are common, commercially available computer-aided design (CAD) tools. At the core of the COSMOSMotion rigid body dynamic simulation package is the ADAMS solver.

The ADAMS solver does not require the reduction of musculoskeletal joints to simplified idealized joints. The motion between bodies is dictated by algorithms with user-defined contact parameters to characterize the interactions between the two parts. [1] This allows the musculoskeletal model's surface geometry, ligamentous constraints, and applied loads dictate joint kinematics. Because of SolidWorks wide-spread use, the program supports a wide variety of engineering formats including: Parasolid, IGES, DXF and STL. This versatility prevents the user from needing special software to create the initial rigid body solids. Further, the ADAMS solver is seamlessly incorporated into COSMOSMotion and SolidWorks. This fact allows for solid body creation and rigid body simulation in the same software package, and therefore, results and design alteration are easily achieved without converting, compressing, or importing/exporting functions. [48,49]

1.3 RIGID BODY MODELING OF THE WRIST

As loads are transmitted from the hand to the forearm, the carpal bones of the wrist and their supporting ligaments are prone to injuries due to their small size and the high loads to which they are exposed. The use of computational models represents an effective method of allowing researchers the ability to determine how the loads are transmitted through the wrist and use that information to develop new therapies capable of minimizing patient suffering and restoring joint function. However, the wrist joint is difficult to model due to the number of bones involved and its complex soft tissue interactions. Only a few studies have attempted to simulate forces and motion in the wrist joint using RBM. [3,28,41-43,52,74] When analyzing multiple body contact, the rigid body modeling method is particularly attractive because of its relative computational efficiency. As stated before, this technique represents the structure of the wrist as a collection of rigid bodies, representing the bones of the carpus that are interconnected by linear tensile spring elements, representing the ligaments. Force vectors are then applied to the model to simulate physiological wrist muscle loads to produce motion.

The majority of the previous studies were simplified to two dimensions. Horii et al [41] was one of the first groups to create a two-dimensional rigid body model of the wrist, using it to examine how different surgical procedures used for treating Kienböck's disease modify the force distribution across the carpus. Manal et al [52] and Schuind et al [74] both created separate rigid body models of the wrist from two dimensional posterior-anterior radiographs to investigate pressure transmission through a juvenile idiopathic arthritic wrist and a normal wrist, respectively. The primary limitations in each of these studies are the omission of a third dimension, and thus preclusion of the intricate interaction between the bony geometries, as well

as limiting the simulation to a static, neutral loading position. Ide and An also conducted similar 2D RBM studies. [3,42]

Subsequent studies using the RBM method have accounted for 3-dimensional joint geometry and loading conditions, and therefore provide a more accurate representation of rigid body carpal kinematics. Iwasaki et al [43] looked at the biomechanical effects of Kienböck's disease of the carpus by analyzing the effects of limited intercarpal fusion in a 3D rigid body on force transmission through the carpus. Joint force, joint peak pressure, and ligament tension were also explored. Here, only a static grip maneuver was simulated as the loading condition, and other loading conditions were not considered; this served as the study's main limitation.

Fischli et al [28] conducted a study in which a 3D rigid body model was used to predict 3D carpal bone kinematics in extension, and radial/ulnar deviation (flexion motion was excluded), but several questionable simplifications were included in the study. The metacarpals were fused to bones in the distal carpal row, and the pisiform was fused to the triquetrum. While the third metacarpal and capitate can be considered one functioning unit [64], there is considerable motion at the carpometacarpal joint and piso-triquetral joint. [56] Further, motion was modeled in an inverse dynamics scenario, where a particular carpal bone's location (determined by radiograph) was matched in the model by prescribing the muscular soft tissue forces to end up in a similar position. On the contrary, model motion should employ a forward dynamic scenario, whereby model geometry and structure dictate function without prescribing soft tissue artifacts. [46]

Carpal bones translate and rotate with six degrees of freedom, and each motion affects the stress distribution and articulations of neighboring bones and soft tissue structures. Therefore,

simplifying the wrist to two dimensions or static positions hinders its capability in widespread predictive use. Further, fusion of the pisiform to the triquetrum, as well as the distal carpal row to the metacarpals, eliminates motion at these articulations and therefore decreases overall carpal bone motion. While each study provides relevant information and insight into aspects of wrist biomechanics, no one model provides accurate three-dimensional articular contact with motion dictated only by the osteoarticular bony surfaces and soft tissue ligamentous constraints in a forward dynamics scenario.

1.4 OBJECTIVES

The goal of this thesis was to develop and validate a computational model of the wrist joint for purpose of investigation of the joints biomechanics and its complex bony and soft tissue interactions. Joint behaviour and kinematics were dictated only by highly accurate 3D osteoarticular contact, ligamentous constraints, and muscle loading as opposed to prescribing joint motion as a reduced, idealized degree of freedom joint. Osteoarticular surfaces and soft tissue constraints were derived from computed tomography of a cadaveric human upper extremity and reported physiologic literature, respectively. The model utilized commercially-available software to accurately represent and simulate joint function. Finally, the model was validated against an experimental cadaveric study examining wrist range of motion after the fusion and excision of various carpal bones in the wrist. [65] Validation included comparing the results of this experimental study with results obtained from the computational model.

2. WRIST ANATOMY

2.1 SKELETAL ANATOMY

The wrist joint is not a single joint, as commonly described, but rather, it is a complex combination of several joints that articulate to produce a composite effect seen as the normal range of motion of the wrist. The bones comprising the wrist joint complex are the distal radius, the distal ulna, the eight carpal bones and the bases of the five metacarpal bones (Figure 2.1-1). The unique features of our wrist found in these individual joints separate us from other mammals and provide the controlling ability our opposable thumb and index finger mobility. The ability to grasp objects and move them with force and precision rests on the configurations of these wrist carpal joints.

2.1.1 Bony Anatomy

The most proximal bones contributing to the mechanics of the wrist joint are the two long bones of the forearm: the radius and ulna. The distal ends of these long bones articulate with the proximal carpal row. On the radius, there are two separate articular facets, called fossae, separated by a sagittal ridge called the interfacet prominence (Figure 2.1-2). The scaphoid fossa can be triangular or oval shaped and has a smaller radius of curvature than that of the lunate fossa.[20] The lunate fossa is rectangular in shape, and the entire surface of the distal radius is covered with cartilage. The lateral edge of the distal radius contains a prominence called the

radial styloid, which extends further distally than the rest of the radius (Figure 2.1-1). It has a pyramid shape and is the site of a few ligament insertions constraining the carpus. The radius' articulation with the ulna is called the sigmoid fossa or ulnar notch of the radius. It is a concave semicylindrical surface and provides articulation with the convex surface of the ulna as well as provides attachment points for the distal radioulnar ligaments, distal radioulnar joint capsule, and articular disc of the triangular fibrocartilage complex (TFCC).

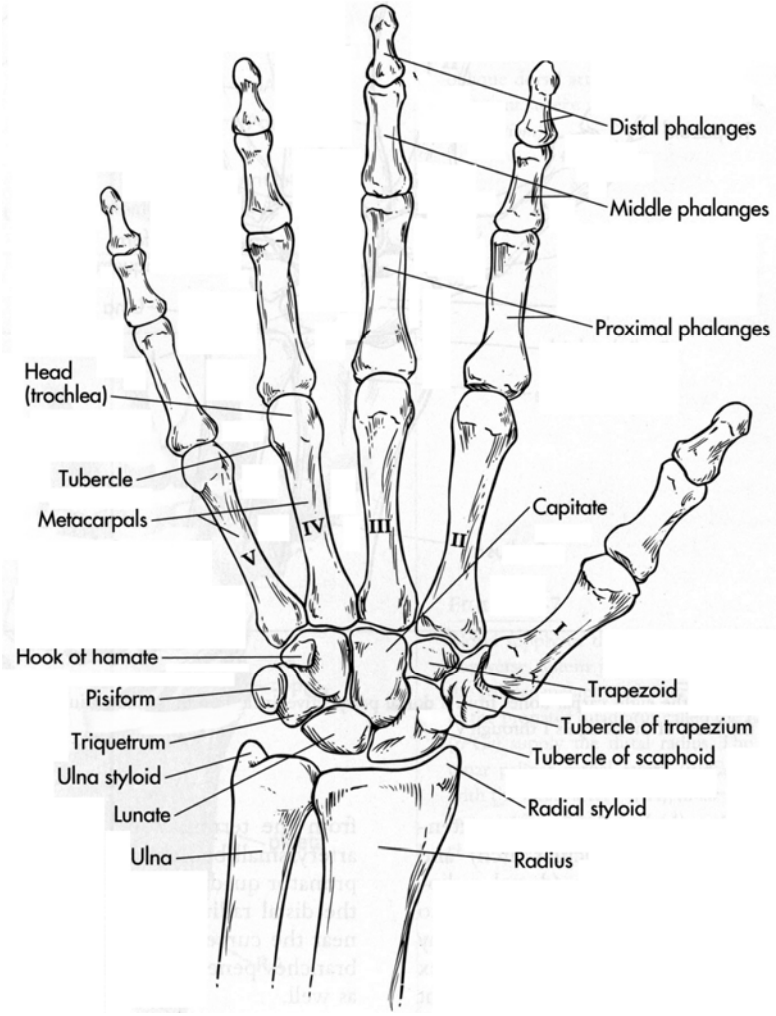

Figure 2.1-1: Palmar aspect of the bony anatomy of the wrist and hand [20]

The distal end of the ulna consists of the rounded ulnar head that articulates with the sigmoid notch of the radius. It has a conical shape, and articular cartilage covers almost seventy-five percent of the total surface. There are three parts to the distal ulna: a lateral surface for articulation with the articular disc of the TFCC, a central depression for the attachment of the apex of the disc, and a medial prominence called the ulnar styloid (Figure 2.1-2). The ulnar styloid provides attachment for the ulnocarpal ligaments as well as components of the TFCC.[63]

The eight carpal bones of the wrist are typically divided into two horizontal anatomic groups of four bones each: a proximal row and a distal row. Beginning radially, the proximal row consists of the scaphoid, lunate, triquetrum, and pisiform. The distal row is comprised of the trapezium, trapezoid, capitate, and hamate. The distal carpal row has been considered as one relatively fixed or constrained group of bones in kinematic and load studies.[80,81] The proximal carpal row is, by comparison, much less constrained.

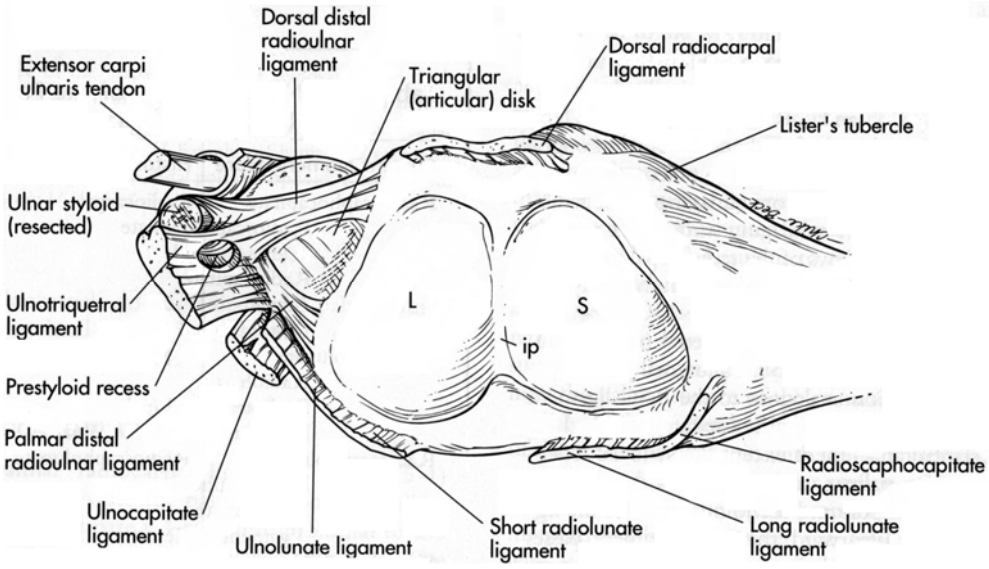

Figure 2.1-2: Distal perspective of the radiocarpal joint [20]

Beginning on the radial side of the proximal row, the scaphoid is one of the largest bones in the carpus, and it is the largest in the proximal row. The scaphoid has a medial and distal concavity that provides an important stabilizing link between the proximal and distal carpal rows.[20,29,77] It has four distinct articular surfaces which cover the majority of the scaphoid surface. A proximal, convex surface articulates with the scaphoid fossa of the distal radius. Just medial to this exists another articular surface that is semilunar in shape and articulates with the lateral aspect of the lunate. A concave, oval-shaped facet exists on the distal and medial aspect of the scaphoid, articulating with the lateral portion of the head of the capitate. The distal portion of the scaphoid also articulates with the trapezoid and trapezium, by way of a convex surface, and this surface represents the fourth articular surface of the scaphoid. On the palmar aspect of the scaphoid, there is a rounded prominence extruding between the proximal and distal articular surfaces. This prominence, called the scaphoid tuberosity, provides attachment for a few strong ligaments as well as a pivot point for the flexor carpi radialis (FCR). [25] The narrower and shorter dorsal surface is also non-articulating and is located below the extensor tendons.

Similar to the scaphoid, the lunate has four articular surfaces: proximal, distal, lateral, and medial. Two-thirds of the proximal articular surface of the lunate articulates with the lunate fossa of the distal radius, while the medial one-third of the proximal surface articulates with the articular disc of the TFCC. The distal articular surface of the lunate is biconcave and articulates with the capitate by way of a large lateral facet and the hamate by way of a smaller medial facet. The lunate articulates with the scaphoid laterally and the triquetrum medially through flat and semilunar surfaces. The lunate also has two nonarticular surfaces on the palmar and dorsal sides. The palmar aspect of the bone is rough and trapezoidal in shape and is the site of attachment for several ligaments. The dorsal aspect is triangular and smaller than the palmar aspect. The distal

edges of the two nonarticular surfaces have a stabilizing role with respect to the head of the capitate during wrist flexion and extension.[20]

The triquetrum has multiple ligamentous insertions and four articular surfaces: distal, radial, proximal, and anterior. The distal articular surface articulates with the hamate bone and has a helicoidal surface. The radial articular surface articulates with the lunate, and is flat and semilunar in shape. The proximal surface is small, triangular and convex, and it articulates with the articular disc of the TFCC. The anterior articular surface has two areas: a lateral surface containing ligamentous attachments and a distal surface for the pisiform. This distal portion of the anterior articular surface is flat, oval-shaped and covered by cartilage. The dorsal facet of the triquetrum is divided into two by a transverse ridge. These two areas, one proximal and one distal, are triangular in shape. The transverse ridge is important because it receives several ligamentous attachments.[19] The sheath of the extensor carpi ulnaris (ECU) travels over the dorsal aspect, and the dorsal surface continues around the bone until it meets the edge of the articular surface for the pisiform.

The pisiform, sometimes considered a sesamoid bone, is a carpal bone into which the flexor carpi ulnaris (FCU) inserts. The pisiform has only one posterior slightly concave, oval-shaped articular surface that articulates with the triquetrum. Therefore, the pisiform is the only carpal bone that has a single articulation and the only carpal bone with a tendon insertion from a forearm muscle. The remaining anterior surface of the pisiform is rough, rounded, and fully covered by soft tissue attachments.[66] Soft tissue structures inserting on the anterior aspect include the flexor carpi ulnaris, flexor retinaculum, abductor digiti minimi (ADM), extensor retinaculum, pisotriquetral joint capsule, pisohamate (PH) ligament, and pisometacarpal (PM) ligament.

Beginning radially in the distal row, the trapezium is the most mobile bone, yet it is tightly bound to the trapezoid and has four articular surfaces.[32] There is a saddle-shaped articular surface for articulation with the first metacarpal. A small triangular, medial articular surface exists on the distal end of the trapezium for articulation with the second metacarpal. The articular surface between the trapezium and the trapezoid is a somewhat quadrilateral facet. The fourth articular surface is a concave proximal surface that articulates with the distal pole of the scaphoid. On the palmar side of the trapezium, there is a groove for the FCR tendon as well as a vertical prominence called the tubercle of the trapezium or trapezial ridge (Figure 2.1-1). This tubercle is the where strong ligaments, including the flexor retinaculum (FR), insert.

The smallest bone of the distal row is the trapezoid, which lies just ulnar to the trapezium. The trapezoid has four articular surfaces (proximal, distal, lateral and medial) and two non-articulating surfaces (palmar and dorsal). The proximal articular surface is slightly concave and continues with the concavity of the trapezium's proximal articulation with the distal pole of the scaphoid. The distal articular surface has two facets separated by a sagittal ridge that fits deep into a notch in the in the base of the second metacarpal forming a tight junction. The lateral and medial articular surfaces are flat and bound to their corresponding facets of the trapezium and capitate, respectively. The palmar non-articular surface is rectangular and fully covered by ligaments, while the dorsal aspect is a flat, pentagram-shaped surface covered by extensor tendons.[32]

The capitate is the largest carpal bone and is the keystone of the transverse carpal arch.[32] There are numerous articular surfaces on the capitate as it contacts seven different bones. The proximal one-third of the bone is covered by cartilage and is referred to as the head of the capitate. The head contains three different articular facets: one lateral for the scaphoid, one

proximal for the lunate, and a third medial for the hamate. The distal portion of the bone is called the body of the capitate. On the radial side of the body of the capitate, there is a flat surface covered in cartilage for articulation with the trapezoid, while on the ulnar side there is a facet for articulation with the hamate. The distal articular surface of the capitate has contact with three metacarpal bones: a central facet that contacts the third metacarpal, a small lateral face that contacts the styloid process of the second metacarpal and a third small facet for the fourth metacarpal base.

The hamate is the most medial carpal bone of the distal row. The distal surface of the hamate articulates with the bases of the fourth and fifth metacarpal bones by way of a saddle-shaped surface covered with cartilage. The hamate has a lateral and proximal articulating surface with the triquetrum, as well as a lateral articulating surface with the capitate. The palmar non-articulating surface of the hamate has a prominent rounded projection called the hook of the hamate (Figure 2.1-1). The tip of the hook is the site of attachment for several important structures including the flexor retinaculum, PH ligament and HM ligament. The lateral aspect of the hook is the medial wall of the carpal tunnel (Figure 2.1-3) that serves as a conduit for several flexor tendons. The dorsal non-articulating aspect is a triangular-shaped that has interaction with the sheath of the ECU.[20]

The bases of the five metacarpal bones are broad with blunt ends. They articulate with each other by means of flat medial and lateral facets, with palmar and dorsal intermetacarpal ligaments connecting their respective non-articular surfaces. The second metacarpal base has a sagittal notch for the trapezoid, with an ulnar and dorsal prominence called the metacarpal styloid process that matches the shape of the distal articular facet of the capitate.[79] Because the joint between the four ulnar metacarpals and the carpal bones is compact and tight, there is

limited motion between them. By contrast, there is substantial motion at the first carpometacarpal joint. [21] This joint is much less stable and provides thumb apposition.

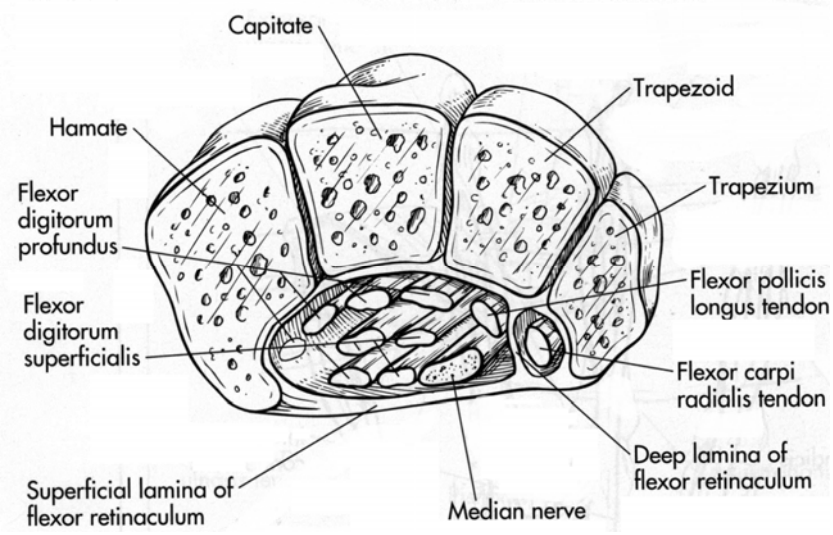

Figure 2.1-3: Cross-section view of carpal tunnel from dorsal perspective [20]

2.1.2 Joints of Wrist

There are four distinct joints in the wrist that combine to provide its full range of motion (Figure 2.1-4). The distal radioulnar joint is the most proximal of the joints formed by the distal interactions between the radius and ulna. The radiocarpal joint is formed by the articulations of the distal radius and ulna with the proximal carpal row. The articulation between the proximal and distal carpal rows forms the midcarpal joint. And most distally, the articulation between the distal carpal row and the bases of the metacarpals comprise the carpometacarpal joint.

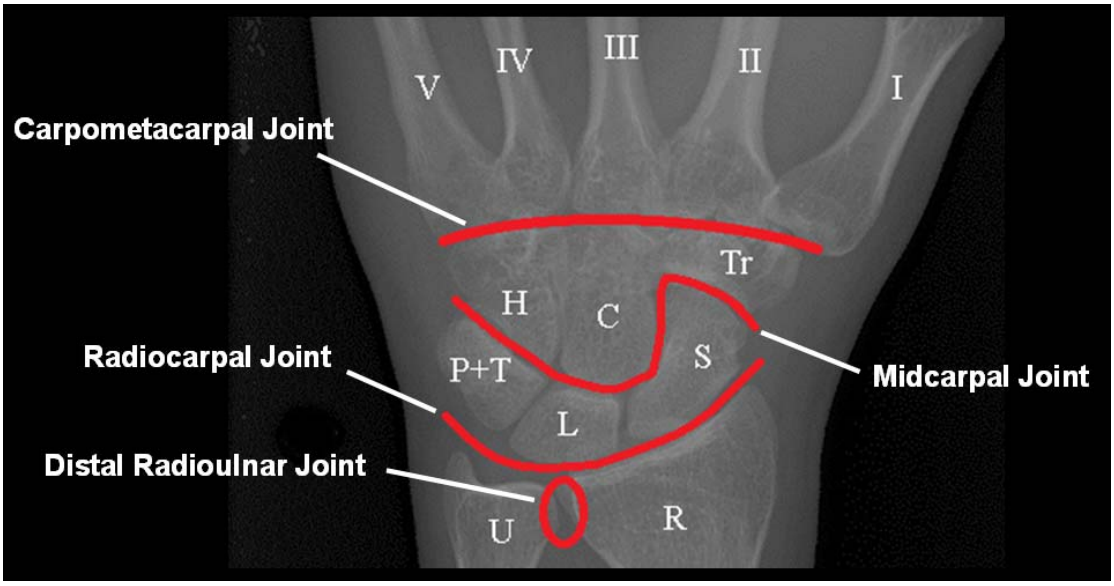

Figure 2.1-4: Joints of the wrist

The most proximal joint of the wrist is the distal radioulnar joint (DRUJ). The distal radioulnar joint provides the proximal articulation for the carpus and consists of the distal radius and ulna with the TFCC. The articular surface between the radius and ulna is the sigmoid notch, where the generally concave cylindrical surface of the radius articulates with the generally convex cylindrical surface of the ulna. The second part of the DRUJ is the triangular fibrocartilage complex. The DRUJ is bounded by the TFCC, which represents the most distal extent of the DRUJ, and contains an articular disc bound by several ligaments.[11] The entire DRUJ is surrounded dorsally, volarly and proximally by a fibrous joint capsule. [26]

The radiocarpal joint is formed by the articulations of the radius with the scaphoid and lunate as well as the interaction between the ulna, TFCC, pisiform and triquetrum. The distal surface of the radius can be divided into a triangular articular fossa for interaction with the scaphoid and a rectangular fossa for interaction with the lunate. Separating these two fossae is a ridge termed the interfacet prominence (IP), which coincides just proximal to the scapholunate joint. The proximal surface of the scaphoid has a higher radius of curvature than that of the

proximal lunate, while the articulating surface of the proximal triquetrum is relatively flat. The triquetrum does not necessarily articulate with another bone however. Rather, it rests on the articular disc of the TFCC.[4] The fibrocartilage disc of the TFCC joins the articular cartilage of the lunate fossa to form a gently concave boundary to the radiocarpal joint. Filling the ulnar gap between the TFCC and the triquetrum is a wedge shaped soft tissue called the meniscus homologue.

The midcarpal joint is the articulation between the proximal and distal carpal rows, and is sigmoidal in shape, with a concave-distal arc radially and a concave-proximal arc ulnarly. The midcarpal joint is a combination of three different types of articulation. Laterally, the distal surface of the scaphoid is convex and articulates with the concavity formed by the trapezium, trapezoid and capitate. The central part of the midcarpal joint is formed by the articulations of the distal scaphoid and distal lunate, both of which together form a concave surface, and the convex head of the capitate. Medially, the articulation between the triquetrum and hamate is helicoid or screw shaped in configuration.[4]

The carpometacarpal joint attaches the hand to the carpus by way of the first though fifth metacarpals. The joint is a tight ligamentous complex that connects the four ulnar metacarpal bases to their corresponding carpal bones forming a single articular compartment. The junction between the third metacarpal and the capitate is considered to be rigid, and as such, the distal carpal row and metacarpals tend to move in a similar fashion. [64]

2.2 LIGAMENTOUS ANATOMY

The ligamentous anatomy of the wrist is extensive and varies across the literature and between subjects. These facts make defining and describing the carpal ligaments a project in itself, and the following definition represents the most logical division and definition when attempting to classify the ligaments of the wrist. The carpal ligaments may be divided into two groups based on their location of origin: extrinsic and intrinsic.[76] Extrinsic ligaments have an attachment on bones outside of the carpus as well as an attachment on the carpal bones, while intrinsic ligaments attach entirely within the confines of the carpus.

2.2.1 Extrinsic Ligaments

Extrinsic ligaments cross the radiocarpal joint, midcarpal joint, or both and can be considered capsular ligaments.[20] There are extrinsic ligaments originating on both the radius and the ulna. The palmar radiocarpal ligaments originate on the palmar rim of the radius and insert very deeply. These ligaments form a continuous capsular enclosure for the radiocarpal joint. There are three distinct extrinsic palmar radiocarpal ligaments that have been defined and represented in this model. From radial to ulnar, these ligaments are the radioscaphocapitate (RSC) ligament, long radiolunate (LRL) ligament, and short radiolunate (SRL) ligament. The ulnar region of the radiocarpal joint has three extrinsic ligaments originating from the palmar extent of the TFCC, the ulnolunate (UL) ligament, the ulnotriquetral (UT) ligament and the ulnocapitate (UC) ligament. The dorsum has one extrinsic radiocarpal ligament, the dorsal radiocarpal (DRC) ligament, which arises from the dorsal rim of the distal radius (Figure 2.2-1).

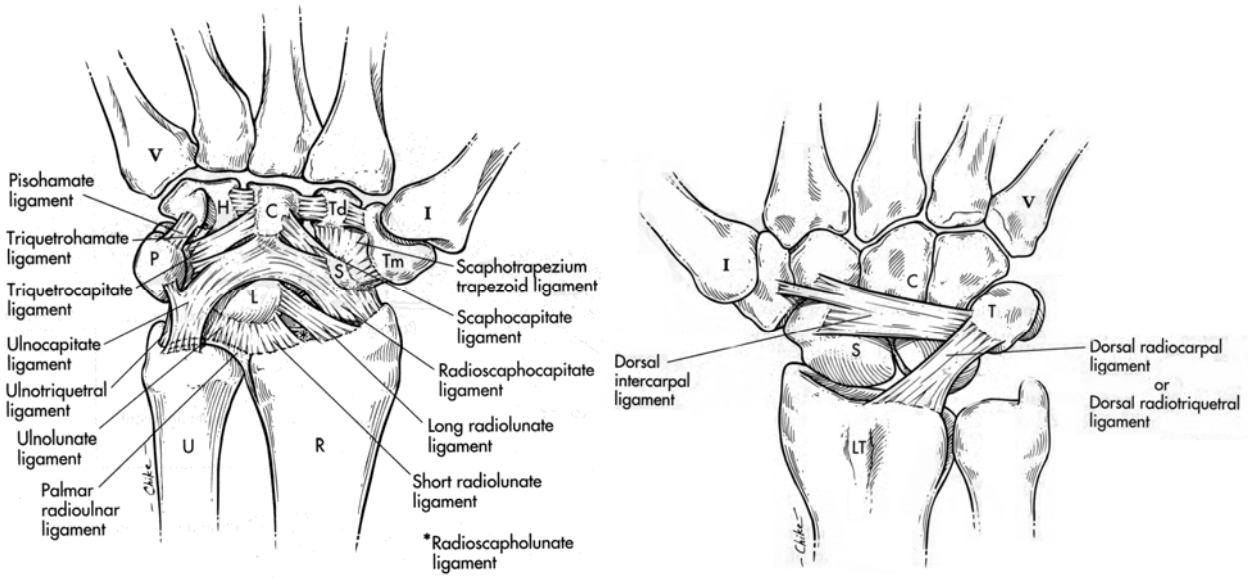

Figure 2.2-1: Palmar and dorsal view of extrinsic and midcarpal intrinsic wrist ligaments [20]

The RSC ligament is the most radial of the palmar radiocarpal ligaments, and it originates from the radial styloid and the palmar lip of the radius (Figure 2.2-1). The RSC ligament courses distally and ulnarly and has several insertion areas, but the ligament does not have any distinguishable divisions for the various insertions. The most radial insertion is on the scaphoid with insertion on the lateral aspect of the scaphoid waist. Medially, the RSC inserts into the proximal surface of the distal pole of the scaphoid and spreads medially throughout the region of the proximal pole of the scaphoid. The remaining medial portion of the RSC continues ulnarly and distally to insert onto the proximal pole of the scaphoid with a few of the fibers actually inserting onto the body of the capitate. Just ulnar to the RSC ligament is the LRL ligament (Figure 2.2-1). The LRL ligament connects the radius to the lunate, and it originates on the palmar ridge of the distal radius, spanning the majority of the width of the scaphoid fossa. Radially, the LRL overlaps the most superficial fibers of the RSC ligament to form a continuous capsule. The LRL ligament passes palmar to the proximal pole of the scaphoid and over the scapholunate interosseous ligament. The LRL ligament inserts in the radial half of the palmar

horn of the lunate. The third palmar extrinsic ligament located on the radial side of the wrist is the SRL ligament, and it arises from the palmar margin of the lunate fossa (Figure 2.2-1). The SRL is thick and courses distally and ulnarly to insert into the proximal aspect of the palmar horn of the lunate. Ulnarly, the SRL ligament blends with fibers from the TFCC and the UL ligament. This ligament appears to be the principal stabilizer of the lunate, as it is the structure that is responsible for maintaining the proximity of the lunate to the distal radius in lunate dislocation.[4]

On the ulnar side of the wrist, the UL ligament arises from the region of origin of the palmar radioulnar ligament (Figure 2.2-1). This ligament is continuous with the SRL ligament, and distally, the ligament cannot be distinguished from the SRL ligament as it courses distally to attach to the proximal aspect of the horn of the lunate. The UL ligament shares a common insertion with the UT ligament and is considered a part of the TFCC. Ulnar to the UL ligament, the UT ligament also originates from the region of the palmar radioulnar ligament (Figure 2.2-1). The UT ligament is complex and quite variable between subjects. [20] The most radial fibers course directly distally and insert into the proximal and palmar margin of the triquetrum. The majority of the UT fibers form the ulnar wall of the radiocarpal joint. This ulnar region of the UT ligament is thick and thins only as the dorsal portion of the radiocarpal joint is reached. The UT ligament contributes to the floor of the sixth extensor tendon compartment on the dorsum of the wrist. The majority of the ligament inserts into the medial aspect of the triquetrum before continuing as part of the TFCC. The UT continues distally as a continuous structure to attach to the hook of the hamate and base of the fifth metacarpal respectively. The final ligament originating on the ulnar side of the wrist is the UC ligament, which some consider part of an arcuate or deltoid ligament (Figure 2.2-1).[4] The UC ligament originates from the base of the

radial styloid and part of the palmar radioulnar ligament. It courses distally with some fibers inserting on the triquetrum and pisiform. Many fibers continue distally past this point around the distal margin of the palmar horn of the lunate. At this point, the UC fibers begin to blend with the terminal fibers of the RSC ligament. The blending of the RSC and UC ligament give the appearance of a deltoid ligament. From a functional point of view, the palmar ligaments depict a "V" shape formed by the extrinsic RSC, UC, and UL ligaments with the intrinsic TC, TH, and SC ligaments.[71]

Only one extrinsic ligament exists on the dorsum of the wrist, the DRC ligament (Figure 2.2-1). The DRC ligament originates from the dorsal margin of the distal radius just distal to Lister's tubercle. This band courses ulnarly and distally to insert on the dorsal rim of the triquetrum. This ligament forms the floor of the fourth, fifth and sixth extensor tendon compartments. At the DRC ligament's termination, fibers from the DRC blend with fibers from the dorsal intercarpal (DIC) ligament (Figure 2.2-1).

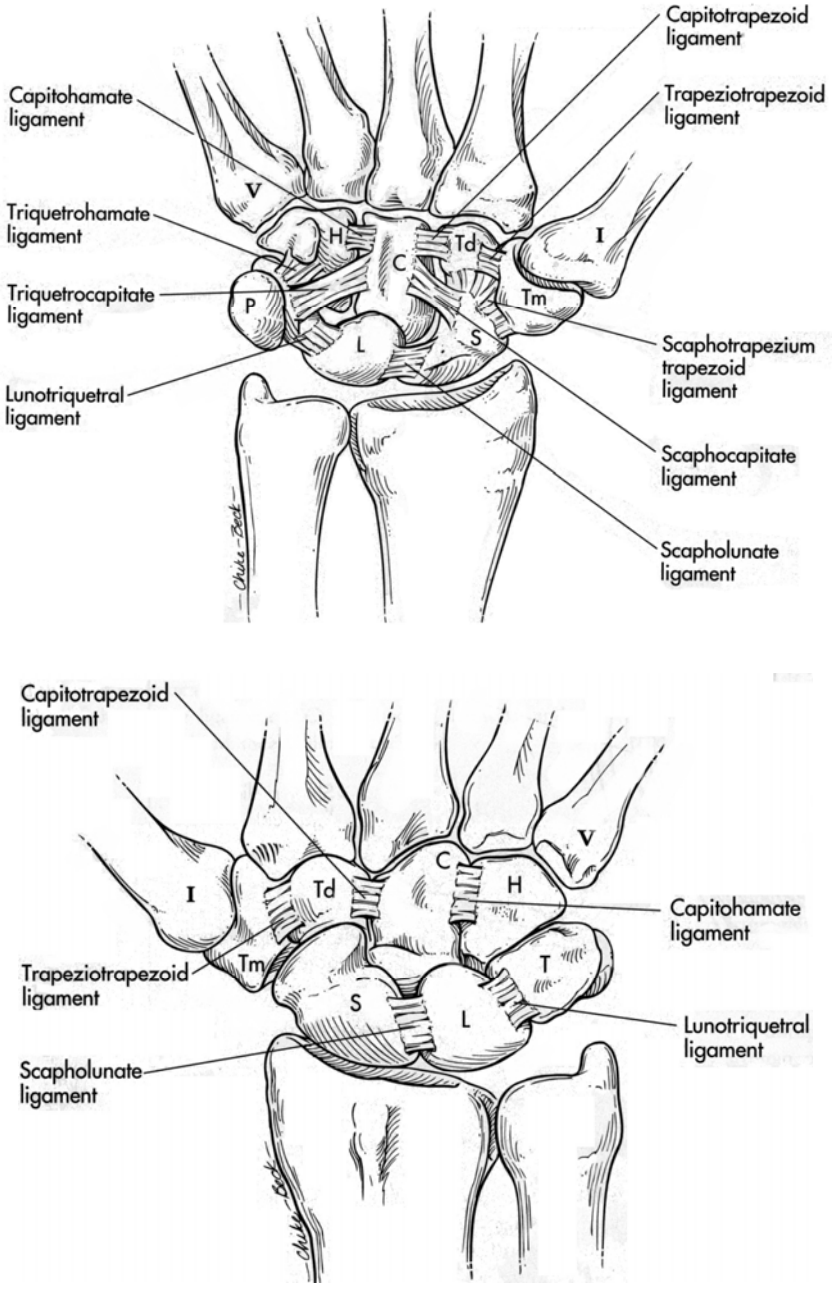

Figure 2.2-2: Palmar (top) and dorsal (bottom) views of the intrinsic ligaments [20]

2.2.2 Intrinsic Ligaments

Intrinsic ligaments (Figure 2.2-2) play an important role in stabilization, mobility, and mechanical integrity. The difference between ligaments that span the mid-carpal joint and those that do not can be seen in the specific roles of the ligaments. There are only a few intrinsic ligaments that span the mid-carpal joint, which could explain the relatively great mobility between the proximal and distal carpal rows. These ligaments are most importantly stabilizers. The palmar intrinsic midcarpal ligaments are the scaphotrapziotrapezoid (STT) ligament, the scaphocapitate (SC) ligament, the triquetrocapitate (TC) ligament, the triquetrohamate (TH) ligament, and the pisohamate (PH) ligament. The only midcarpal ligament on the dorsum of the carpus is the dorsal intercarpal (DIC) ligament. The intrinsic ligaments that do not span the mid-carpal joint, called interosseous ligaments, are confined to either the proximal or distal carpal rows and play a substantial role in maintaining the mechanical integrity of each row. The proximal row intercarpal ligaments are the scapholunate (SL) ligament, the lunotriquetral (LT) ligament, and the pisotriquetral (PT) ligament, while the distal row interosseous ligaments and the trapeziotrapezoidal (TT) ligament, the capitotrapezoid (CT) ligament, and the capitohamate (CH) ligament.

Beginning radially, the first intrinsic ligament that crosses the mid-carpal joint is the STT ligament (Figure 2.2-2). The STT fibers originate from the palmar surface of the distal pole of the scaphoid and fans out to form two bands: one that attaches to the trapezium and another that attaches to the trapezoid. Each band courses distally to insert into the palmar proximal surface of the trapezium near the tubercle of the trapezium and the proximal palmar surface of the trapezoid. Just ulnar to the STT, the SC ligament originates at the waist of the scaphoid just distal to the course of the RSC (Figure 2.2-2). It courses distally and ulnarly to insert onto the

radial half of the palmar surface of the head of the capitate near the insertion of the capitotrapzoid ligament. The STT and SC ligaments have been shown to play an important role as major distal stabilizers of the scaphoid.[4] The TC ligament originates from the triquetrum on the ulnar side of the wrist (Figure 2.2-2). Its origin is adjacent to the attachments of the LT and UT ligaments. The TC ligament courses distally and radially toward the body of the capitate where it attaches to the ulnar side of the capitate, and it terminates just proximal to the interosseous CH ligament. Ulnar and distal to the TC ligament, the TH ligament spans the midcarpal joint between the triquetrum and hamate. The TH ligament originates from fibers in the distal half of the pisotriquetral joint ligament on the distal-palmar portion of the triquetrum. The TH lies just palmar to the PH ligament and inserts broadly on the body of the hamate near the base of the hamulus, with no major insertion onto the proximal pole of the hamate. The PH ligament originates from the distal half of the pisiform just above the pisotriquetral joint (Figure 2.2-1). The PH ligament is a direct continuation of the tendon of the FCU muscle tendon beyond the pisiform. It courses distally to the hook of the hamate where it terminates by inserting into the tip of the hamulus. Just ulnar to the origin of the PH, there also exists the pisometacarpal (PM) ligament that acts as a second direct continuation of the FCU that spans the distance between the distal pisiform and proximal base of the fifth metacarpal. Both the PM ligament and PH ligament are similar in structure and function: both are cordlike and meant to act as continuations of the FCU. [20]

On the dorsum of the hand, the only ligament spanning the midcarpal joint is the dorsal intercarpal ligament (Figure 2.2-1). The DIC ligament originates on the dorsal surface of the triquetrum, continuous with fibers from the DRC. It courses distally and obliquely radially towards the dorsal scaphoid, trapezium and trapezoid. The main part of the ligament fans out and

inserts into the dorsal ridge of the waist of the scaphoid. Other fibers continue radially and distally to insert into the dorsal cortices of the trapezoid and, to a lesser extent, the trapezium.

The interosseous intrinsic ligaments within the proximal and distal carpal rows of the wrist are composed of dorsal and palmar regions and connect two adjacent carpal bones. Within the proximal row, there are three interosseous ligaments: the SL ligament, the LT ligament, and the PT ligament. Both the SL and LT ligaments have true palmar and dorsal components, with the palmar regions being longer than the dorsal regions.

The SL ligament is a “C”-shaped ligament that spans the interval between the dorsal, proximal and palmar edges of the scapholunate joint surface (Figure 2.2-2). The SL ligament has a dorsal region and palmar region. The dorsal region is a thick ligament that spans the space between the dorsal horn of the lunate and the proximal pole of the scaphoid. The palmar region of the SL ligament is thinner and courses distally from the proximal lunate to the scaphoid. Ulnar to the SL ligament is the LT ligament. The LT ligament is very similar to the SL ligament, in that it is also “C”-shaped. It also has a dorsal and palmar region. The main difference between the SL and LT ligament is in the size and orientation. The dorsal and palmar regions of the LT ligament are relatively thick. The dorsal region interdigitates with fibers from the DRC ligament at the level of insertion on the triquetrum. The palmar region of the LT ligament originates at the ulnar edge of the horn of the lunate and courses ulnarly across the lunotriquetral joint space. It inserts into the palmar surface of the triquetrum combining with fibers from the UC, PT, and TC ligaments. The third proximal row intrinsic ligament is the pisotriquetral ligament. The PT ligament is a horseshoe shaped structure that wraps around the perimeter of the pisiform-triquetrum joint. The ligament connects the lateral, distal, and medial edges of the joint. The PT

ligament is composed of short parallel fibers directly connecting the edges of the pisiform and triquetrum.

Individual intrinsic ligaments within the distal row are found on the palmar and dorsal surfaces of the adjacent carpal bones. Within the distal carpal row, there are three interosseous ligaments: the TT ligament, the CT ligament, and the CH ligament. These ligaments span the joint and are not easy to separate anatomically.

The TT ligament connects the trapezium to the trapezoid on both the palmar and dorsal cortical surfaces (Figure 2.2-2). The proximal and distal surfaces of the TT joint are in open communication with the STT and first and second metacarpal joints respectively. Ulnar to the TT ligament is the CT ligament. The CT ligament consists of palmar and dorsal regions composed of short, transversely oriented fibers spanning the joint space. The palmar region attaches to the body of the capitate just distal to the attachments of the SC and TC ligaments. The dorsal ligament band is present on only the distal half of the surface of the capitate. Deep within the articular surface between the capitate and trapezoid is a matched offset or recess in the articular surfaces. Spanning this joint space is the deep CT ligament (Figure 2.2-3). The ligament courses obliquely dorsal to palmar from the trapezoid to the capitate. Finally, the CH ligament is the last intrinsic ligament in the distal carpal row. The CH ligament, like the CT ligament, has a palmar and dorsal component as well as a deep region. The dorsal and palmar regions of the CH ligament connect the dorsal and palmar outermost parts of the hamate and capitate bodies. The palmar region is located distal to the insertions of the TC and TH ligaments. The capitohamate joint has a non-articular recess created from the “pan-handling” of the articular surfaces. The recess is located at the palmar and distal extreme of the ulnar surface of the capitate and the

radial surface of the hamate. The deep region of the capitohamate ligament is located in this recess and fills the entirety of this non-articular region (Figure 2.2-3).

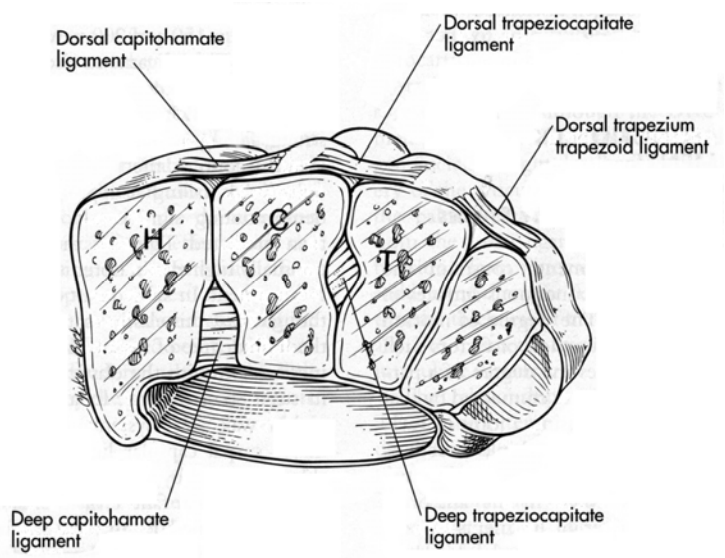

Figure 2.2-3: Transverse section of wrist through the distal carpal [20]

2.2.3 The Triangular Fibrocartilage Complex

The triangular fibrocartilage complex is sometimes considered an extrinsic ligamentous structure connecting the ulnar side of the carpus to the distal ulna, although its structure and function make it unique. Components of the TFCC stabilize the distal radioulnar joint, translate and diffuse forces from the wrist to the ulna, and stabilize the lunate within the radiolunate fossa.[71] The complex consists of the articular fibrocartilage disc, dorsal and volar radioulnar ligaments, ulnolunate ligament, ulnotriquetral ligament, meniscal homologue, and the extensor carpi ulnaris tendon sheath (Figure 2.2-5).

The TFCC is a biconcave structure that stretches from the sigmoid notch of the radius to the ulnar styloid process. It can attach to both or either the fovea at the base of the styloid and the tip of the styloid. The dorsal and volar radioulnar ligaments attach the dorsal and volar margins of the sigmoid notch and form the dorsal and volar borders, respectively, of the articular disc. The UL and UT ligaments extend from the volar ulnolunate ligament to the volar aspect of the lunate and triquetrum, respectively and do not necessarily insert on the distal ulna. In the central portion between the dorsal and volar radioulnar ligaments, there exists a weight-bearing cartilaginous disc that articulates with the lunate and triquetrum.

While the function and structure of the TFCC is somewhat unclear, it has been accepted that the TFCC has a nonhomogeneous structure with a central cartilaginous portion and peripheral fibrous portion with multiple areas of support. The TFCC may function as a buffer or cushion between the distal end of the ulna and the radioulnar carpal joint.[71] The triangular fibrocartilage complex also serves as the primary ligament of support for the radius to the ulnar side of the carpus with the TFCC carrying about 20% of the axial load from the wrist to the

forearm.[20] What is unclear is the exact role of the TFCC in maintaining support for the distal radioulnar joint compared with other associated structures.

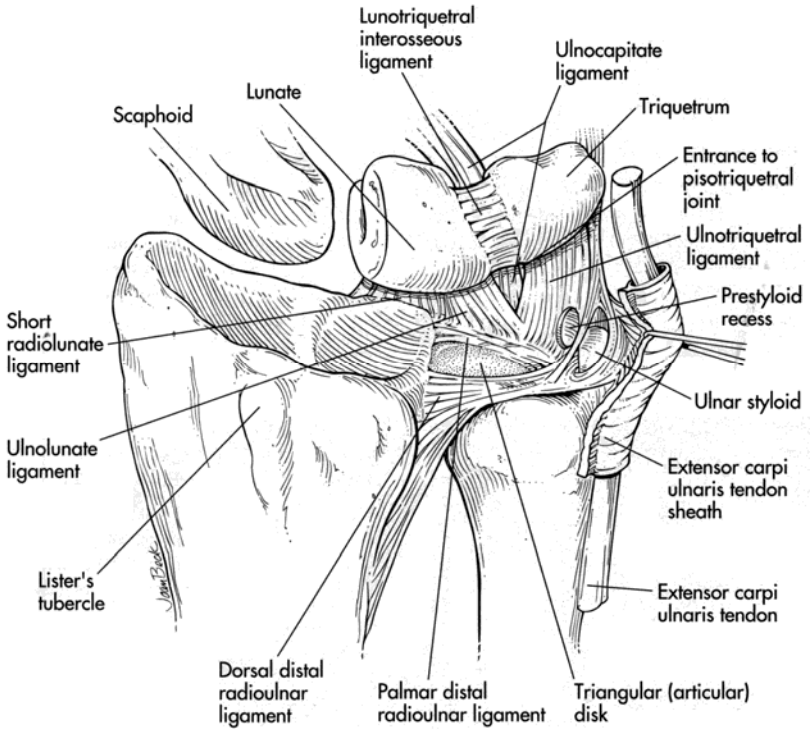

Figure 2.2-5: The ulnocarpal triangular fibrocartilage complex [20]

2.3 RETINACULAR AND MUSCULAR ANATOMY

The retinacular system of the wrist is in place to maintain a normal relationship between the tendons crossing the wrist and its capsular structures. The flexor and extensor retinacula are circumferential distal extensions of the deep antebrachial fascia. The retinacula serve as pulleys for extrinsic tendons, redirecting the line of action of the tendons passing by them, and they serve as an interface to protect their confined contents from direct pressure.

The radial attachment of the flexor retinaculum is found on the palmar surfaces of the scaphoid and trapezium, and the ulnar attachment is found on the pisiform and hamate. This encloses the region of the wrist commonly called the carpal tunnel (Figure 2.1-3). The carpal tunnel contains all the flexor tendons of the forearm except for the flexor carpi ulnaris (FCU) and flexor carpi radialis (FCR). The FCU is the only forearm muscle with an insertion actually on the carpus; the FCU attaches to the proximal surface of the pisiform, with the aforementioned pisohamate and pisometacarpal ligaments acting as an extension of the FCU tendon. The FCR is found within a separate tunnel where the antebrachial fascia splits to form a fibro-osseous septum. This septum forms the sheath of the FCR tendon that inserts on the tubercle of the trapezium, staying palmar and radial to the carpal tunnel. The FCR tendon inserts on the palmar aspect of the base of the second metacarpal. The FCU and FCR are the main flexors of the wrist (Figure 2.3-1).

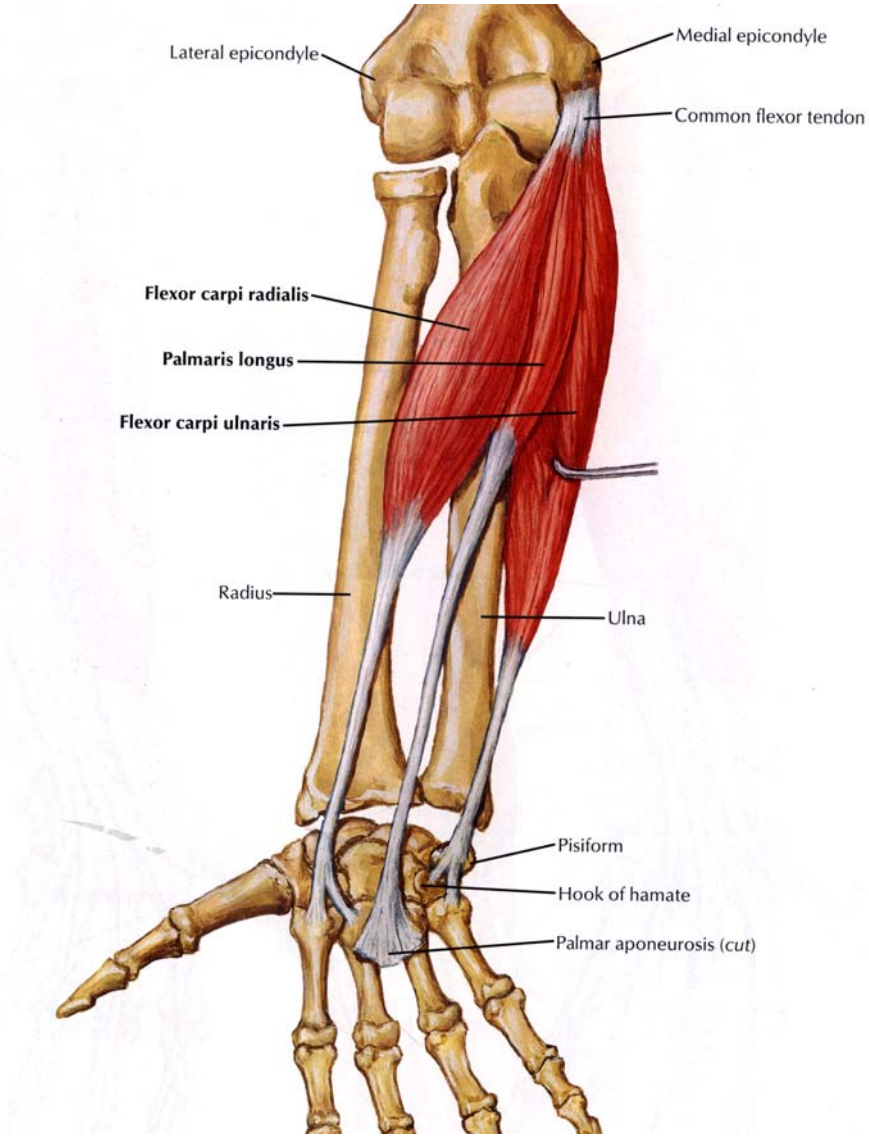

Figure 2.3-1: Flexors of right forearm (palmar view) [60]

The dorsal retinaculum of the wrist is also derived from the deep forearm fascia and generally contains six major compartments, numbered in sequence from radial to ulnar (Figure 2.3-2). The first compartment is found on the dorsoradial surface of the distal radius and contains the abductor pollicis longus (APL) and extensor pollicis brevis (EPB) tendons. The second compartment spans the dorsum of the wrist from the termination of the first extensor compartment to the radial side of Lister's tubercle and contains the extensor carpi radialis longus (ECRL) and extensor carpi radialis brevis (ECRB) tendons. The third compartment contains the

extensor pollicis longus (EPL) tendon and lies just ulnar to Lister's tubercle. The fourth extensor retinaculum compartment, containing the extensor digitorum communis (EDC) and extensor indicis proprius (EIP), lies on the most ulnar portion of the dorsal surface of the radius. The fifth compartment is found in the region just dorsal to the distal radioulnar joint and contains the tendon of the extensor digiti quanti (EDQ). The sixth compartment is located on the dorsal-ulnar surface of the distal ulna and contains the tendon of the extensor carpi ulnaris (ECU). The main tendons of use in wrist extension are contained in extensor retinaculum compartments two and six, which house the ECRB, ECRL, and ECU.

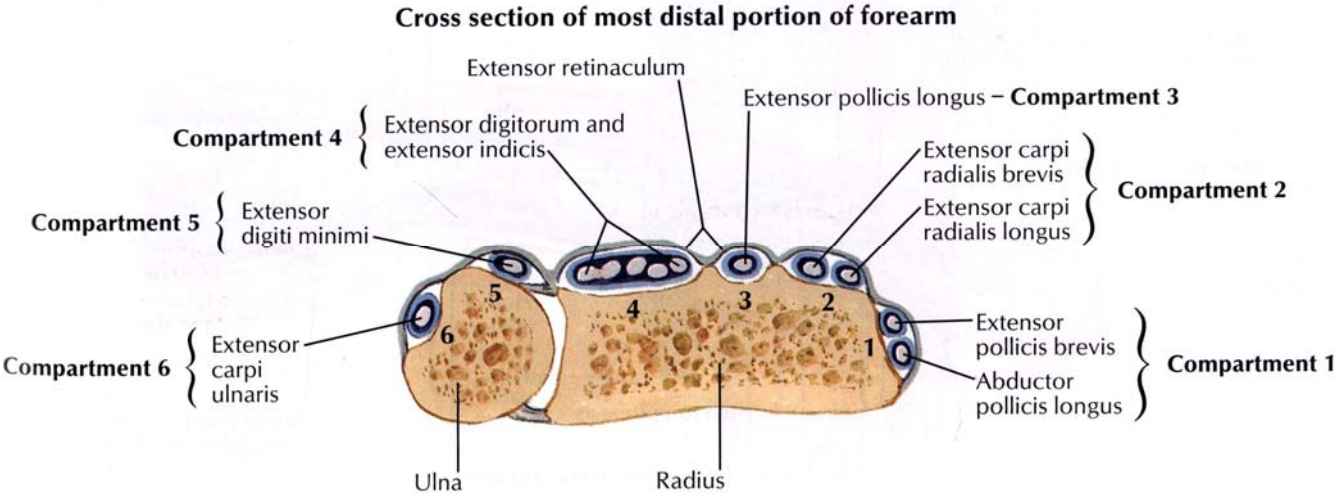

Figure 2.3-2: Extensor retinaculum compartments [60]

3. THREE DIMENSIONAL SOLID BODY MODEL

Rigid body modeling of the wrist predicts both soft tissue and bony surface contributions of the fifteen bones in the carpus and integrates the articular contact between those bones. A precise three-dimensional (3-D) reproduction of the wrist is essential when beginning to create an accurate rigid body model. To accomplish this, high resolution computed tomography (CT) scans were obtained from a cadaveric specimen to translate the bony geometry into a representative stack of 2-D images. Commercially available software was then used to transform the 2-D images into 3-D solid bodies. Upon obtaining an accurate solid body representation of the wrist, COSMOSMotion was used to create ligamentous and muscular forces to reproduce soft tissue constraints.

3.1 COMPUTED TOMOGRAPHY (CT)

A right fresh frozen upper extremity, including the shoulder joint, was harvested from a 52 year old white male cadaveric specimen. The arm was free from any obvious deformities, and the appendage did not appear to have any musculoskeletal abnormalities that would change normal biomechanical function. The appendage was placed onto the table of a SOMATOM Sensation 64 helical scanner (Siemens AG, Forcheim, Germany) (Figure 3.1-1). Consideration was given to the positioning of the wrist as close to neutral as possible by inspection. The position of the wrist defined as neutral flexion/extension and neutral radial/ulnar deviation by

Wu et al is when the third metacarpal long axis is parallel to the long axis of the radius.[85] Therefore, the long axis of the radius and third metacarpal of the cadaver were positioned roughly parallel to each other and normal to the transverse plane of the scanner. In the end, it was determined that the wrist was positioned only slightly out of the neutral position demonstrating 0.73 degrees of flexion and 7.63 degrees of ulnar deviation. These initial angles were taken into consideration in the final range of motion measurements discussed in Chapter 4.

Scans were taken in high resolution 0.4 millimeter increments in order to better capture the tight spaces between the articular surfaces. The scan totaled 2283 2-D slice images. For this model, only the slices containing the distal radius and ulna and the bones of the carpus were needed, while the remaining slices were taken for use in future modeling. Each 2-D image had a resolution of 512x512 pixels with each pixel containing 12 bits of data. Each of these images shows the density of different regions within that particular slice with bone being the densest and soft tissue being the least dense.

Figure 3.1-1: Cadaver specimen on CT table in neutral position

3.2 MASK CREATION

Once the right upper extremity was scanned, the commercially available medical imaging software MIMICS (Materialise's Interactive Medical Imaging Control System, Materialise, Ann Arbor, MI) was used to transform the 2-D CT images into 3-D triangulated bodies. The stack of DICOM (Digital Imaging and Communications in Medicine) images was imported in order of image capture. The CT scan produces voxels, the three-dimensional equivalent of a pixel, and MIMICS isolated voxels according to Hounsfield units, where the grayscale value within each voxel is constant.

MIMICS was then used to threshold out certain "noisy" voxels in these images. For the solid body model, only the bony bodies are needed. The CT images contain the bone, all soft tissue surrounding the bone, and the CT patient table as well. The most effective and dramatic way to eliminate all of the extraneous voxels and yield only bony surfaces is to adjust the global threshold value in MIMICS. By assigning a global threshold value, MIMICS automatically turns on any mask voxels where the corresponding CT number is equal to or above the assigned value and eliminates any voxel that is less than the assigned volume.

This thresholding process removed data from the CT images according to the radiodensity of each pixel, and thus allowed the user to remove the less dense material and leave the more dense bone. In thresholding, the user can select from various ranges of Hounsfield units (HU) that allow the desired tissue pixels to become active (bright) and all unwanted pixels to become inactive (dark). The Hounsfield scale is a standardization of the relative linear attenuation coefficient of a radiographed body compared to that of water. The preset thresholding option for bone that is native to MIMCS is 226 to 1743 HU, however this value did not necessarily represent the best value for capturing the entirety of the bony surfaces. Trabecular

bone has a much lower density and correspondingly lower linear attenuation coefficient. The thresholding value was adjusted downward until a satisfactory value including all bony regions with limited noise and soft tissue interference was reached (Figure 3.2-1). This value of 180 to 1743 Hounsfield Units captures the majority of trabecular and cortical bone, while not including other soft tissues. These sets of arranged images sharing common threshold values are grouped into “masks” within MIMICS for further editing.

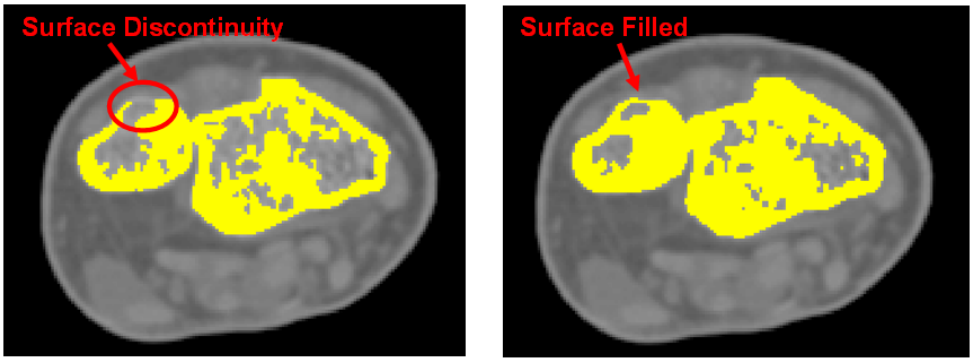

Figure 3.2-1: Use of thresholding to include more cortical and trabecular bone in distal radius and ulna

3.3 MASK EDITING AND THREE-DIMENSIONAL BODY CREATION

The simplest method for mass editing the mask was using the crop and multiple slice edit tools incorporated in the MIMICS software. As stated previously, the entire upper extremity, including the shoulder joint, was scanned, but for the purpose of this model, only the carpus and its articulations were needed. The cropping function is parallel to any traditional cropping tool, and can be used in concert with the multiple slice editing function. In the multiple slice editing tool, changes made to one 2-D DICOM image can be copied up or down multiple slices to expedite the separation process. Using these tools, the proximal portion of the upper extremity was cropped and removed from the mask leaving only the distal radius and ulna along with the carpus, metacarpals and phalanges. This vastly reduced the file size by eliminated numerous 2-D slices that were not needed in this study. By this simple modification, the number of 2-D slices decreased from 2283 images to 644 images.

The cropping tool was used to deselect active voxels that were outside the smallest area that contained the bony surface of the wrist. Once this was done, the multiple slice editing tool was used to deselect those highlighted voxels that were considered extraneous and not part of the bony surface. As seen in Figure 3.3-1, the outlying pixels from the CT table can be easily distinguished from the outer surface of the bone by cropping, and the slice editing tool was used to delete the extra pixels from the image to separate bone from all other tissues and surfaces.

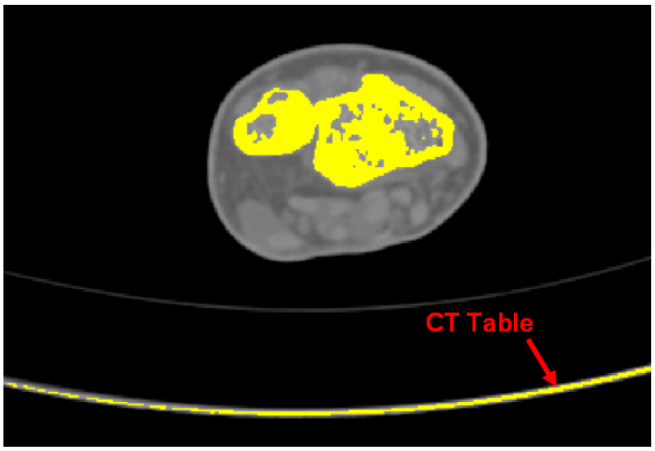

Figure 3.3-1: Materials with a high linear attenuation are present in scan

Once an overall mask with a set thresholding value was chosen that included all osseous surfaces of interest with minimal noise, each individual bone was given its own respective mask in order to simplify mask manipulation and to allow subsequent individual 3-D body acquisition later in the model acquisition process. This was particularly important in differentiating respective articulating surfaces where bones are in close proximity to one another, which is inherently present in the wrist. Each bone must be carefully separated from the neighboring bones in order to create the individual articulating surfaces in the solid model (Figure 3.3-2). Often, a mask contained jagged edges around the bony surface due to the porosity of trabecular bone or very thin cortical bone. The thresholding value chosen captured the majority of the bony surface geometry, but sometimes it contains discontinuities that incorrectly display the surface geometry of the model. Because the accuracy of the solid body model rested on the accuracy of the surface geometry of the articulating surfaces, manual editing was used to compensate for the surface irregularities. For every mask representing an individual bone, the manual slice edit tool was used to fill in gaps in the surface contour to ensure precise surface geometry as well as separate each bone.

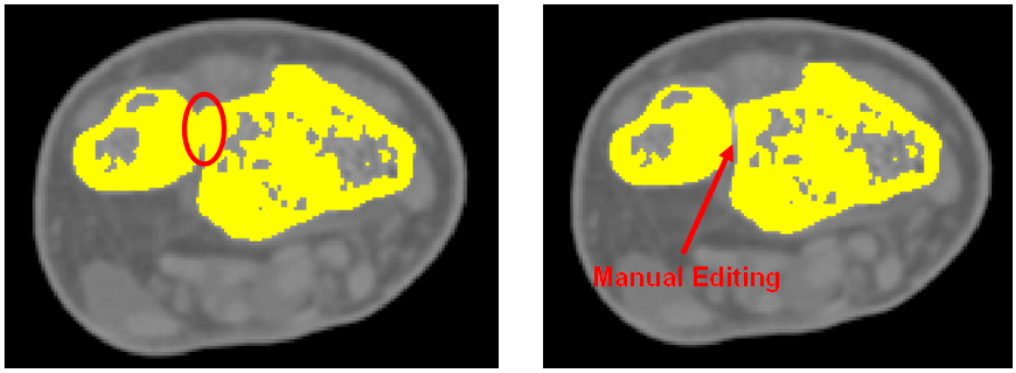

Figure 3.3-2: Manual slice editing to separate distal radius and ulna

MIMICS is able to analyze each CT slice in a given mask and produce a set of 2-D contours called polylines that outline active voxels creating closed loops of cortical bone within each slice. Once the cortical shell of the bone had been captured by the polyline contours, the inactive voids representing trabecular bone or medullar space could be filled using the fill polylines command. Thus, by ensuring the cortical shell was captured and then filling the interior voids, each mask was made solid without manually filling low attenuation areas. These lines can also be used as a check to ensure that the entire surface geometry was captured and there are no cavitations in the polylines (Figure 3.3-3). If a void existed, the slice had to be manually edited to include all bone not represented in the mask. Once the fifteen bones of interest had each been defined by a separate continuous mask, MIMICS was used to perform a cavity fill to create a solid body for each bone (Figure 3.3-4). MIMICS created the solid bodies by interpolating the voxel space between the 0.4 mm image slices, and then surfaces of each bone were triangulated.

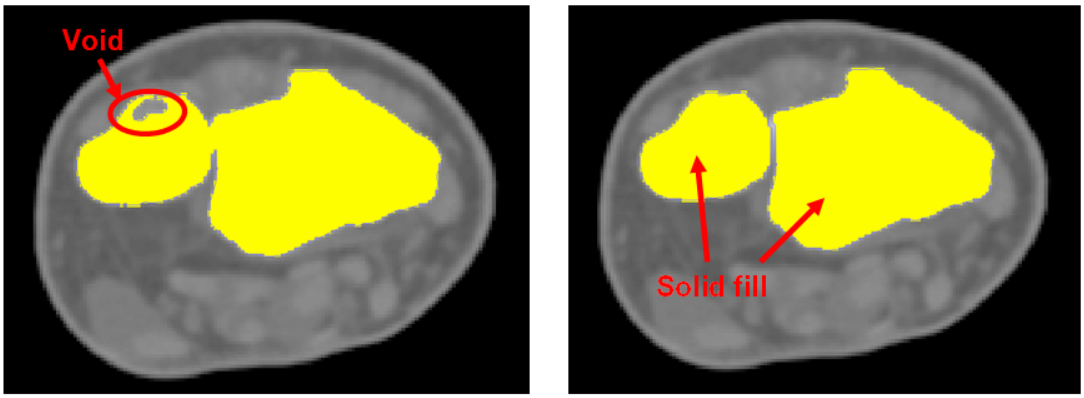

Figure 3.2-3: MIMICS screen capture illustrating use of polylines to check boundary of bony surfaces

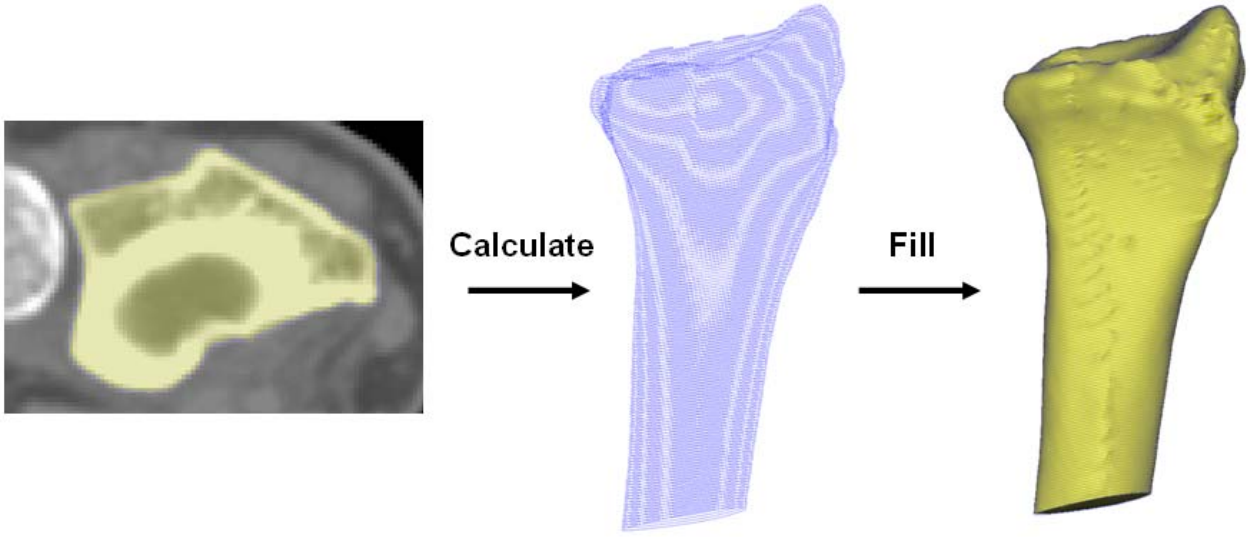

Figure 3.3-4: Interpolation of polylines to create solid body of distal radius

3.4 THREE-DIMENSIONAL BODY REMESHING

After ensuring that the surface geometry was accurate and there were no gaps or extraneous noise, the surface of each solid body was modified to increase quality and reduce the file size. MIMCS created the 3-D bodies by detecting the boundaries within each slice and then created a linear interpolation between successive slices in a given mask. These combined surfaces were represented through triangulation in the remesh module. Originally, the solid bodies contained thousands of triangular facets for each bone in a variety of sizes and angular ratios. Each triangular facet is described by twelve Cartesian coordinates: three for each vertex of the triangle and three more for the directional unit vector. These triangular facets were modified using the MIMICS remeshing module with two surface modification operations: triangle reduction and smoothing. In remeshing, MIMICS can selectively remove and combine triangles resulting in a smooth 3-D body with a more manageable number of triangles. A perfect mesh would consist of all equilateral triangles. While this may not be completely possible, a more consistent and regular mesh performs better in computational simulations.

The triangle reduction surface modification in MIMICS eliminates highly acute triangles, with a single triangle reduction algorithm reducing the initial mesh size of over 100,000 triangles down into the tens of thousand making the model much more manageable and efficient. When the model has over 100,000 triangles, SolidWorks has difficulty importing the solid bodies. MIMICS uses a shape threshold to evaluate the acuteness of triangles and a parameter called “R-in/R-out normalized ratio” is used to quantitatively evaluate the shape quality of the surface triangulations. R-in/R-out is a ratio of twice the radius of an inscribed circle to the radius of an ascribed circle and that value is then normalized to two creating a dimensionless value between 0 and 1. An equilateral triangle would have a value of 1, and triangles with a very low value

usually contain highly acute and obtuse inner angles. The threshold value was set at 0.3, and all triangles below the ratio were effectively eliminated. Depending of the initial quality of the mesh, this function would have an insignificant to minor effect on the total number of triangles but would greatly improve the resulting quality of the mesh. [2]

After the threshold was set, the next step in triangle reduction was evaluating triangle edge angle. Here a threshold angle was assigned that defined the minimum angle to preserve shape geometry. This meant that any two triangles that meet with an angle below this value could be approximated as a single facet in one plane, and any two triangles that met at an angle above this value were identified as representing a unique curvature and thus preserved to keep the original surface contours. The flip threshold angle was set at 15 with a geometric error 0.05 to ensure that the total 3-D volume was virtually unaffected from the triangle reduction.

Next, a smoothing operation was performed to remove some of the small cavitations and discontinuities on the bony surface. This process examines each triangular vertex position and evaluates them according to the weighted contributions of its neighboring triangles. The smoothing operations looks at triangles sharing a common vertex and assigns weights to the adjoining triangles given according to the Smoothing-Factor ratio. When this ratio is low, the initial position of the vertex of the adjoining triangles is predominately responsible for the new vertex position, while if the ratio is high (approaching 1), then weights of all adjacent triangles are considered equally. Each vertex was no longer fixed, and this method of smoothing then moved the vertices according to Equation 3-1 through 3-3 given below.

Specifically, the adjoining triangles sharing a common vertex v^* have other vertices ($v1$, $v2$,…,vk). The difference between the common vertex coordinates and the vertex coordinates of

the adjoining triangles is given a weight (W1) according to the Smoothing-Factor in MIMICS such that:

$$\sum_i W_1(x_i - x) \tag{3-1}$$

$$\sum_i W_1(y_i - y) \tag{3-2}$$

$$\sum_i W_1(z_i - z) \tag{3-3}$$

Where (xi, yi, zi) are the Cartesian coordinates of the ith vertex of the adjoining facets. The results of Equations 3-1 through 3-3 are the new coordinates of the common vertex after applying the smoothing operation. Multiple iterations were needed to reach convergence, and for both the smoothing and triangle reduction functions, fifteen was generally the maximum number of iterations performed. Figure 3.4-1 demonstrates the remeshing process and end result.

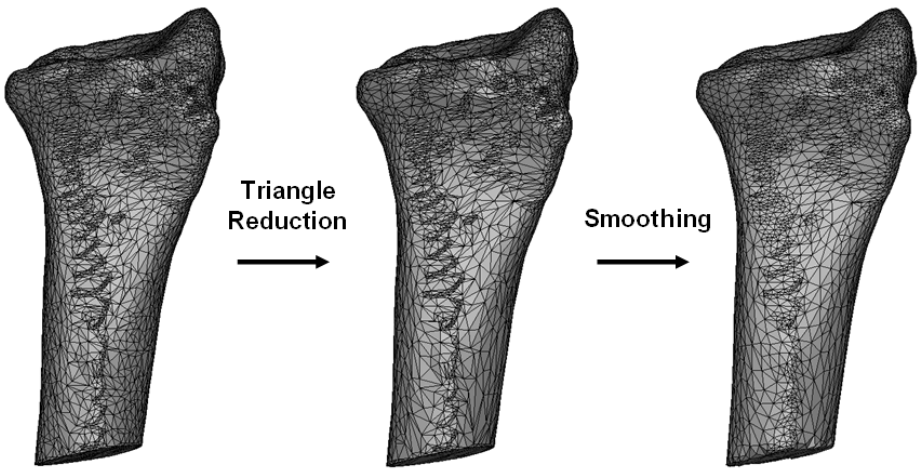

Figure 3.4-1: STL triangulation (left) of distal radius with smoothing (middle) and triangle reduction (right)

3.5 SOLIDWORKS

All bones considered in the wrist complex came out of remeshing with less than 10,000 high-quality triangular facets. Each solid body had a smooth surface, and was exported as a stereolithography (STL) file. The STL file is ideal for computer modeling, as it is compatible with nearly all 3-D modeling software packages. SolidWorks is a commercially available mechanical CAD (computer aided design) software that has the ability to import these files and display the 3D geometry of the solid bodies. Therefore, each bone's STL file was imported separately and saved as its own part to later be joined in an assembly. When SolidWorks imports these files, each vertex on a triangular facet is assigned a 3-D point, and each triangular facet is rebuilt in 3-D space to create a single body.

3.5.1 Assembly and Reference Planes

Solidworks has the ability to add multiple parts together to create an assembly that allows each solid body free movement with respect to each other. Before these parts were allowed to move freely, they were arranged in their correct anatomical position. To do this, a blank assembly was created in SolidWorks, and the radius solid part was loaded into the design space. The radius was fixed in space to prevent further movement and to provide a reference point for each subsequent bone being added to the design space. Then each bone was individually loaded into the design space with the radius, and had their reference planes "mated" to the radius' reference planes. The relative positions of each bone was kept consistent from the CT scan to the SolidWorks design space by keeping the bones defined in terms of the CT scanner's reference frames. Therefore, by mating each bone's reference planes to the radius reference planes respectively, the bones were each oriented in their anatomical position, as shown in Figure 4.5-1.

The reference planes and coordinate systems were then defined according with recommendations by Wu et al on behalf of the International Society of Biomechanics.[85] Separate coordinate systems are necessary to describe relative motion between any two adjacent bones. Global wrist motion, as used in this range of motion study, is defined as the motion of the third metacarpal with respect to the radius; this motion is achieved by movement of the carpal bones with respect to the radius as well as the articulations between the eight carpal bones with respect to each other. The wrist was scanned in an approximately neutral position, and reference systems were created for the radius and thrid metacarpal using anatomic landmarks.

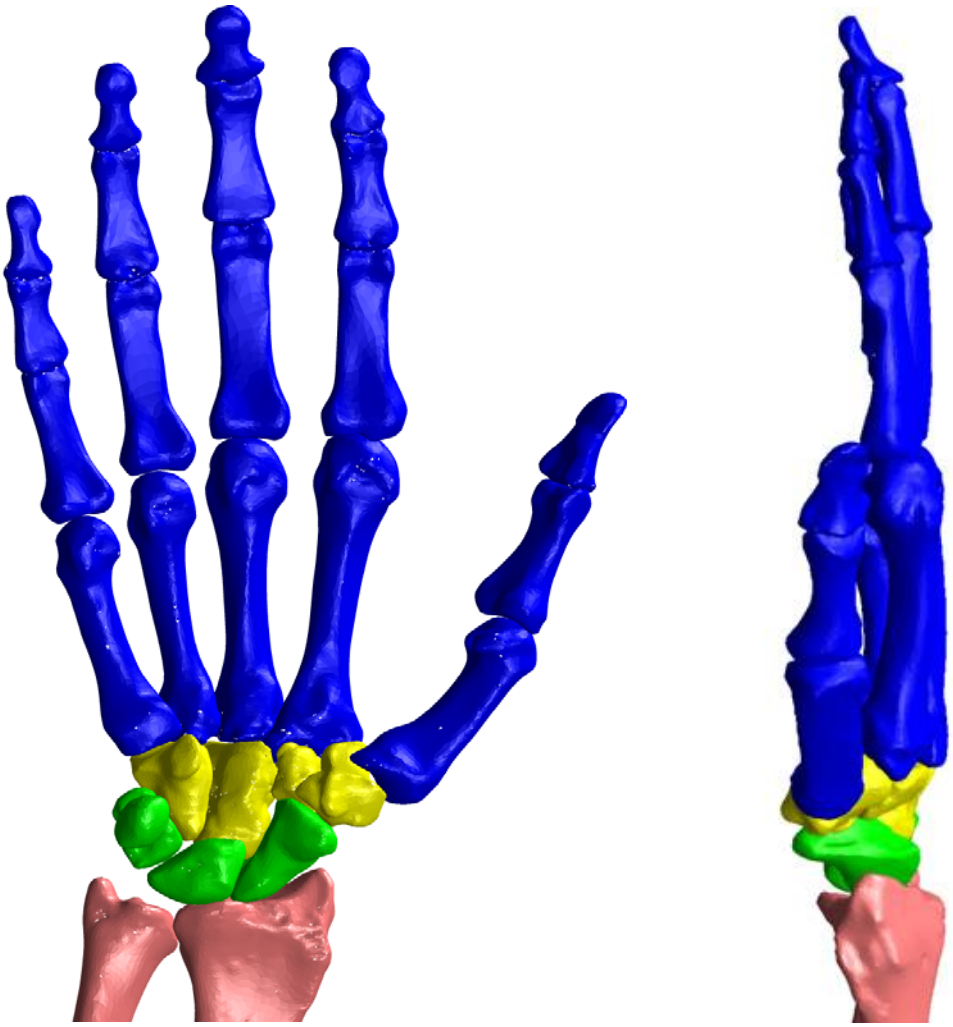

Figure 4.5-1: Palmar (left) and lateral (right) view of computational model

The coordinate system designated for the radius is given with the palm forward (anterior) and the thumb lateral, while the dorsum of the hand and forearm face posterior. For a right arm, the positive y-axis is directed proximally, the positive x-axis is directed volarly, and the positive z-axis is directed radially. This coordinate system was chosen in coordination with the ISB recommendations.[85] The origin of the radius was defined as the midway point between the distal radius at the level of the interfacet prominence between the radioscaphoid and radiolunate fossae, and the proximal radius at the level of the depression in the proximal radial head. The y-axis was then defined as the line parallel to the long shaft of the radius from the origin to the middle of the interfacet prominence. The z-axis is the line perpendicular to the y-axis, and in a plane defined by the tip of the radial styloid, the base of concavity of the sigmoid notch and the origin. Finally, the x-axis is the common line perpendicular to the y- and z-axis (Figure 4.5-2). SolidWorks was used to create sketches of points and connecting lines corresponding to the aforementioned anatomical landmarks to set up the coordinate system in the computational model.

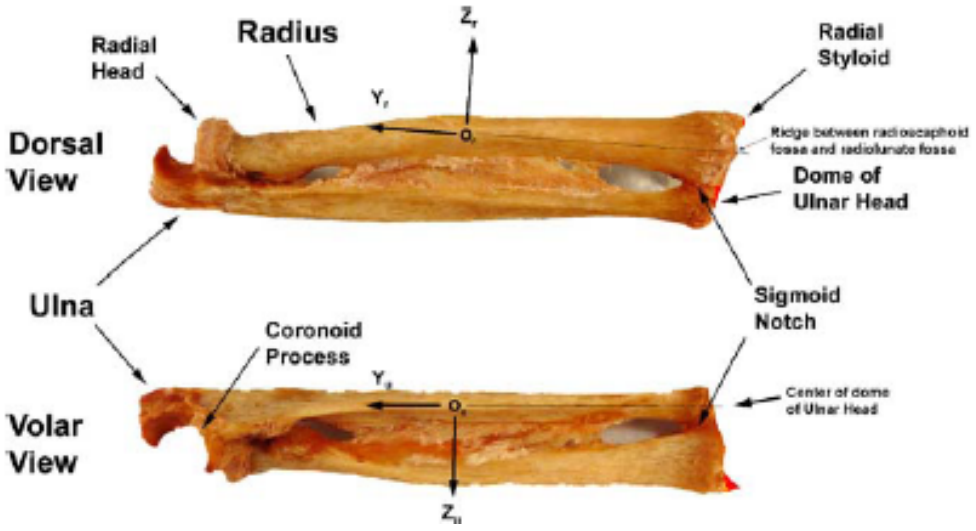

Figure 4.5-2: Radial and ulnar coordinate systems [85]

Similarly for the third metacarpal, the origin was located midway between the base and head of the bone at the approximate center in the transverse plane. The y-axis, or long axis, was defined the line parallel to a line from the center of the distal head to the midpoint of the base. The x-axis is determined by choosing a sagittal plane that will split the metacarpal into mirror images (Figure 4.5-3). Finally, the z-axis is the common line perpendicular to the x- and y-axis of the third metacarpal. Like the radius definitions, the third metacarpal coordinate system was created by sketches of points and lines in Solidworks between relevant anatomical landmarks.

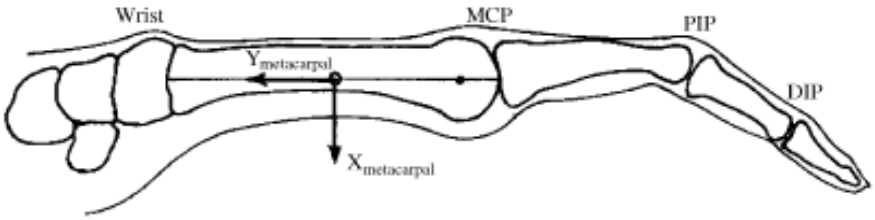

Figure 4.5-3: Coordinate system for the metacarpals [85]

The coordinate systems of the radius and third metacarpal create frames of reference that aid in capturing simulation data. The motion data in the range of motion study was collected in the anteroposterior (AP) plane and mediolateral (ML) plane. The AP plane is defined by the x- and y-axis of the radius, while the ML plane is defined by the y- and z-axis; these reference planes were used to measure flexion/extension and radial/ulnar deviation respectively. Using these definitions, it is also possible to capture angular changes in the eight individual carpal bones with respect to the neutral wrist position. Thus, when the wrist is in neutral position, the coordinate systems for each carpal bone (Figure 4.5-4) should be parallel with the radial coordinate system. The origin of these coordinate systems is located at the volumetric centroid of the bone.

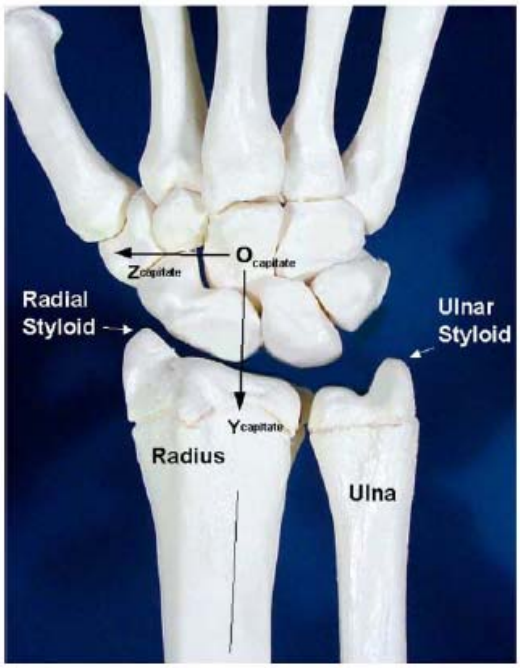

Figure 4.5-4: Capitate coordinate system as an example of carpal coordinate systems [85]

3.5.2 COSMOSMotion

COSMOSMotion is a rigid body simulation package available in SolidWorks that enables users to simulate motion by imposing forces, displacements, and boundary conditions for interactions between the bodies. In the wrist model, constant force vectors representing muscles, tension only spring elements representing ligaments, dampers representing viscoelastic effects and contact parameters reflective of the material stiffness were used to dictate the motion and interaction between the bony “parts” of the assembly. The COSMOSMotion add-on package can also calculate results for any number of variables such as displacements and forces and apply gravitational forces. The resulting rigid body model was controlled by only muscle contraction, ligament stiffness, and highly accurate 3D articular surface contacts.

COSMOSMotion uses the ADAMS solver to model the dynamics of the wrist joint, and ADAMS has a number of variable parameters available to change solver settings. The most basic motion study properties included setting frames per second to 50, 3D contact resolution to its maximum, and geometric accuracy to high. The frames per second setting was a major contributor to computation time, and this value was chosen to provide plenty of data in the motion study while keeping computation time reasonable. 3D contact resolution and geometric accuracy were set to high in order to reduce the amount of error present in the motion study. Gravitational effects were included in the model by orienting gravity along the fixed radius, and subsequently, a force was applied at the centroid of each bone. Once these basic values were set, the advanced motion analysis options were explored.

ADAMS uses a series of algorithms to iteratively solve the simulation using equations of motion and any constraints imposed on the model. A set of coupled differential and algebraic equations is used to define the equations of motion in COSMOSMotion, and a numerical solution to these equations is obtained by integrating the differential equations while satisfying the algebraic constraint equations at every time step. A set of differential equations is numerically stiff when there is a wide spread between high and low frequency eigenvalues, while the high-frequency eigenvalues are overdamped. The speed of the solution of the equations depends on the numerical stiffness of the equations. Stiffer equations result in slower solutions, therefore a stiff integration method is the most efficient way to solve a stiff system. ADAMS provides the user a number of integrators, however the Gear Stiff Integrator (GSTIFF) was chosen because it is a fast and accurate method for computing displacements for a wide range of motion analysis problems. [1]

There are also a number of other variable parameters that the user can change in COSMOS that have effects on capturing events as well as the inherent error. These values, highlighted in Figure 3.5-5 below, were assigned with a goal of achieving the most stability, least error and fastest computation time. These values were obtained by both recommendations for the ADAMS solver, trial and error processes, and communications within the lab. The accuracy and minimum step value were set to an extremely low value to ensure that the GSTIFF integrator would capture the smallest timed events in the model as well as produce the least amount of error. The Jacobian was set at 100% to reevaluate the matrix at every time step to capture all rigid body motion, and maximum iterations was set at fifty to provide sufficient iterations to converge on a solution and capture all motion. Once all motion parameters had been set, soft tissue anatomy and constraints could be created and the model could move on to motion simulations.

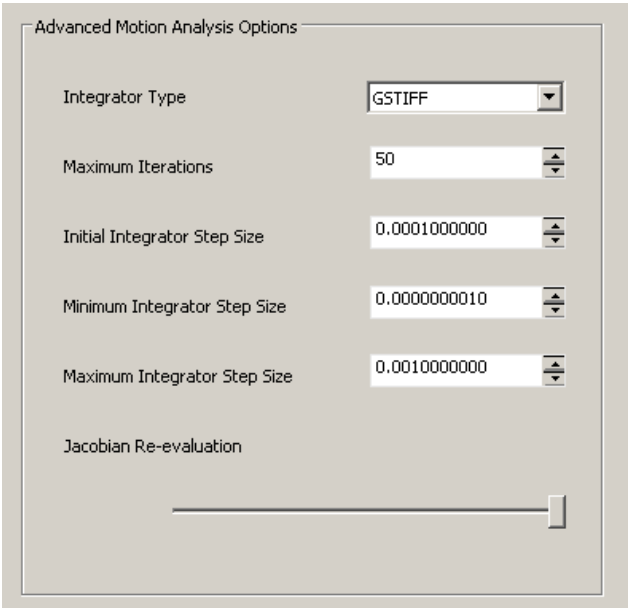

Figure 3.5-5: COSMOSMotion Rigid Body Motion Solver Settings

Once the solid bodies were imported and all other simulation parameters were set, the surface to surface contact settings needed to be set. In this model, the only things prescribing the motion of the 3D solid bodies were the defined connecting soft tissues that will be discussed and the surface contact parameters of the bones themselves. COSMOSMotion has a 3D contact feature that checks for overlap of the solid bodies at each time step in the simulation. If an overlap is detected, SolidWorks calculates the volume of overlap and penetration depth, and COSMOSMotion applies a force at the centroid of the overlapping volume directed outward against both bodies. The magnitude of this force is determined by Equation 3-4, where F_n is the separating force, k is the material stiffness (N/mm), g is the penetration depth, e is the exponent, $c_{\max}$ is the maximum damping force, $d_{\max}$ is the penetration depth at maximum damping, and $\frac{dg}{dt}$ is the penetration velocity. A number of these parameters were user defined in COSMOSMotion. The material stiffness, exponent, max damping, penetration depth, and geometric accuracy can all be altered to change the way that the bodies interact with each other. The geometric accuracy was set to its maximum to ensure accurate model geometry and overlap volume detection. A high stiffness value of 10,000 N/mm was chosen to keep overlap at a minimum. The penetration depth was set at very minimal 0.001 mm, the exponent was set at 1.75, and the damping coefficient was set at 50 (N/mm-s).

$$F_n = k * g^e + Step\left(\frac{dg}{dt}, 0, 0, c_{\max}, d_{\max}\right) \qquad (3\text{-}4)$$

Generally, the changing of these values does not drastically change the results of the simulation. Only stiffness, penetration depth, and exponent have any effect at all, as damping coefficient only affects time and not end position. A series of simulations were run to obtain the

chosen parameters. The parameters that provided end results that were the smoothest and most consistent with minimal computation time and overlap were utilized for the model. A material stiffness value of 10,000 N/mm was chosen to provide a stiff material to keep overlap at a minimum. This value was also low enough to prevent ringing and increased computation time, as stiffer bodies tend to cause integration difficulties. Most material exponent defaults provided in SolidWorks ranged from 1.5 to 2, and a median value of 1.75 was used in the model. Geometric accuracy was set to a maximum and penetration depth to a minimum to ensure that each triangulated body was faithfully represented and overlap of these bodies was kept minimal. Friction inside the joint was considered negligible and was therefore omitted.

3.6 MODELING OF LIGAMENTOUS STRUCTURES

The ligamentous structures present in the wrist were represented as linear tension only forces. The orientation and attachment sites for the ligaments were gathered from anatomic books and scientific literature. The mechanical properties of the ligaments were based on published cadaveric experiments, and as with any research, there was abundant variation across the literature. The ligaments were modeled in COSMOSMotion as straight line force vectors, and the forces were based on their dynamic length.

3.6.1 Origins and Insertions

The origins and insertions of the modeled ligaments were based on anatomic texts and articles describing the ligaments of the wrist in reference to the adjacent bony segments. [8,9,11,18,20,54,57,60,70,71,82] There is considerable variation in the literature concerning the ligamentous anatomy of the wrist. This may be a result of the relatively high number of ligamentous constraints in such a small capsular joint. Certain texts omit various ligaments, while others combine what some consider two separate structures into one. The ligaments created in this model reflect the ligamentous anatomy described in Chapter 2 and are summarized in Table 3.6-1.

Each ligament was given at least four attachment points representing the broad insertion of many of the ligaments. Originally, each ligament was represented by only two points (one insertion and one origin), but this amount of constraint was not sufficient. Many of the ligaments in the wrist have very wide insertions and origins, and a single line of action force could not adequately reproduce the amount of constraint provided by a ligament. Therefore, each

ligamentous structure was reproduced by creating two forces representing the medial and lateral or distal and proximal margins of the ligament. This required two points on each adjoining bone. Interosseous ligaments were given eight attachment points (four dorsal and four palmar), because these ligaments continuously span the joint space between adjacent bones and appear on the palmar and dorsal aspects of the wrist. Anatomical landmarks referenced in literature were identified on the solid bodies and were used to accurately reproduce the ligament origins and insertions. Figure 3.6-1 through Figure 3.6-5 show the modeling of the ligamentous constraints present in the carpal region of the model.

The insertion and origin points for each ligament were sketched as 3-D points coinciding with nodes on the triangulated surface of the two adjoining bones. During the solid body creation process described in section 3.3, vertices from the triangulated surface were available to use as attachment sites for ligamentous constraints. Lines of action for all soft tissue ligaments were represented as straight line vectors between the origin and insertion. The RSC ligament has its origin on the radius and courses distally to insert on the scaphoid and the capitate. Therefore, to adequately represent the two insertions, the ligament had to be represented by two different elements, a radioscaphoid (RS) portion and radiocapitate (RC) portion as shown in Figure 3.6-1. Similarly, the STT ligament has its origin on the distal scaphoid and courses distally to insert on the trapezium and trapezoid. This ligament was represented in the model by three elements, two inserting on the trapezium and a third inserting on the trapezoid as show in Figure 3.6-3. The distal radioulnar ligaments were not modeled because the radius and ulna were fixed in space, thus preventing any relative motion between them. The intermetacarpal and carpometacarpal ligaments were represented by only one linear-tension band each and are shown in the Figure 3.6-5 below.

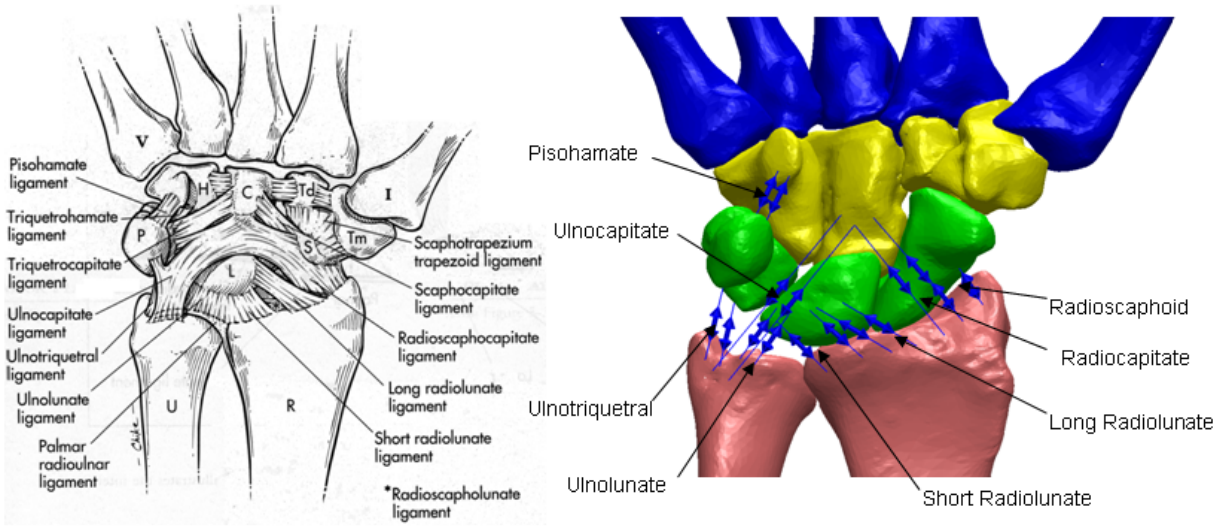

Figure 3.6-1: Modeling of pisohamate ligament and palmar extrinsic ligaments

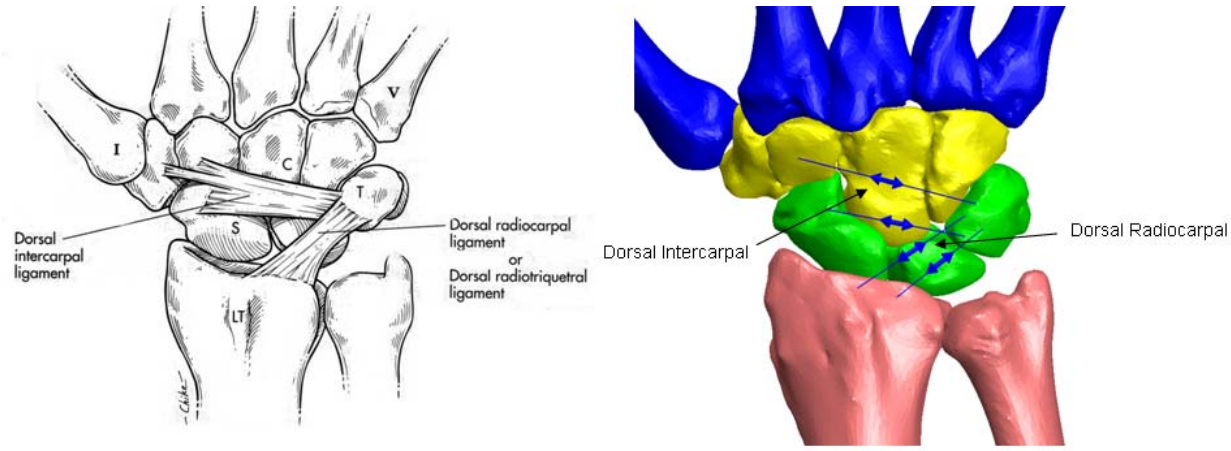

Figure 3.6-2: Modeling of the dorsal radiocarpal and dorsal intercarpal ligaments

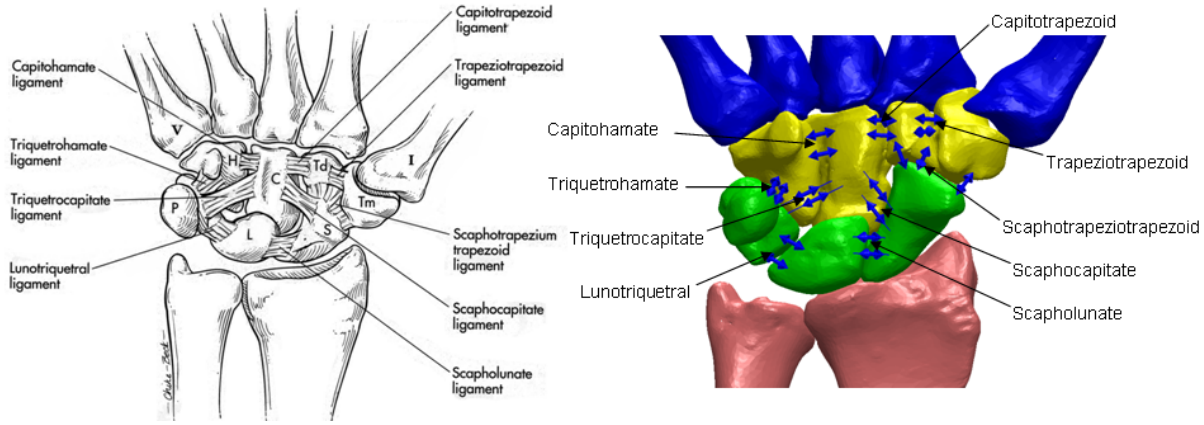

Figure 3.6-3: Modeling of palmar intrinsic ligaments

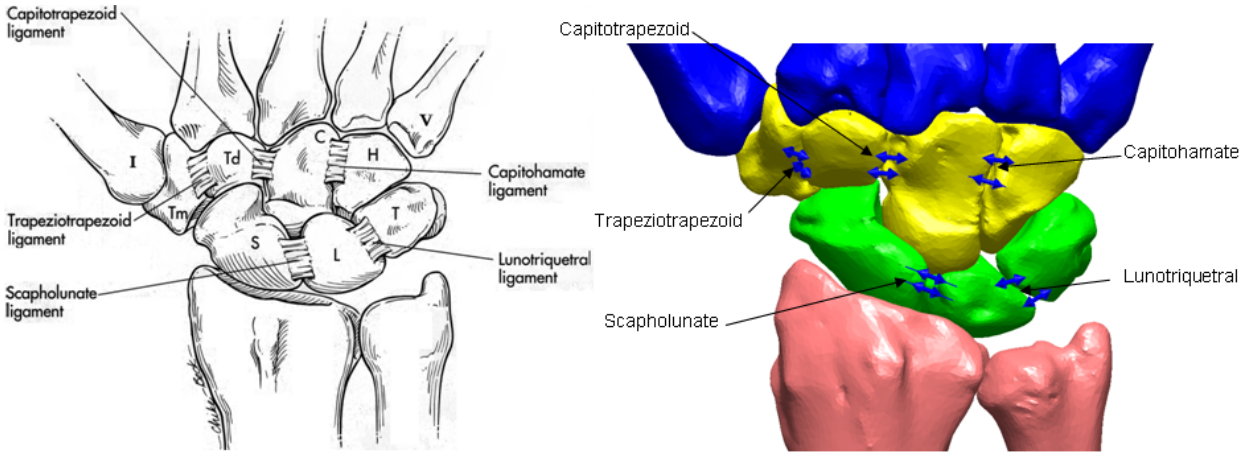

Figure 3.6-4: Modeling of dorsal intrinsic ligaments

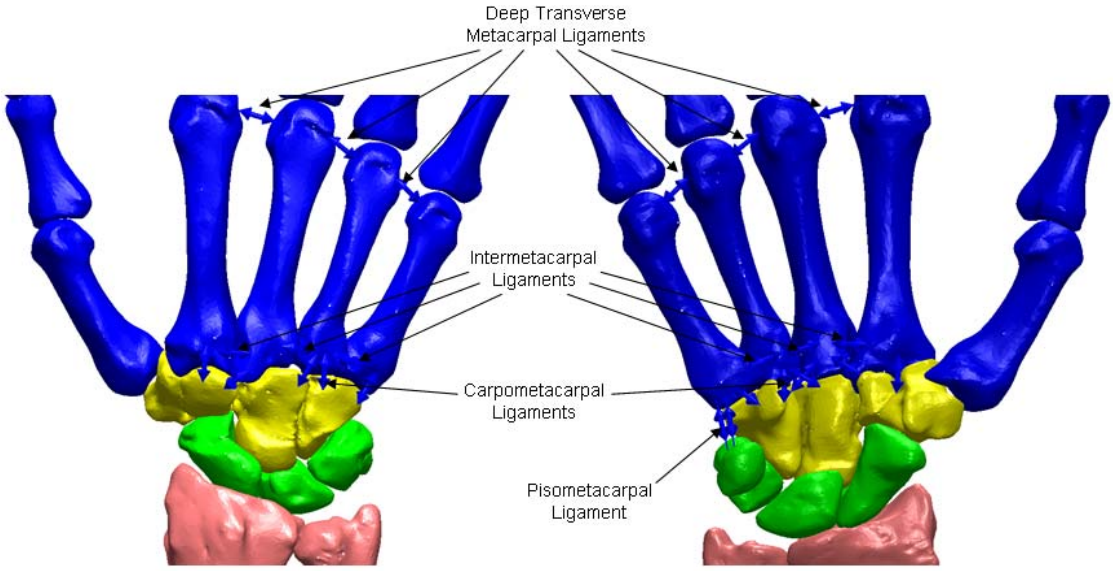

Figure 3.6-5: Modeling of carpometacarpal and intermetacarpal ligaments

3.6.2 Ligament Properties and Modeling

Each ligament's mechanical properties were modeled based on published cadaveric data and previous modeling studies. In the event that a ligament's mechanical properties were not available in a publication, the average value of that ligaments group properties (intrinsic or extrinsic) was used. Various scientific publications provide stiffness, modulus, in situ strain, and stress free length data for a number of ligaments. To model the ligaments, stiffness values (N/mm) were used in place of modulus values, because modeling of the ligaments did not incorporate their cross-sectional areas. If a modulus value was published, these values could be converted into stiffness values by factoring out geometry (Equation 3-5). The ligament stiffness values given in Tables 3.6.1 and 3.6.2 were obtained from load-displacement data published in literature [53] or determined from mechanical testing of bone-ligament-bone preparations. [32,53,74,75] The stiffness values for all ligaments considered in the model varied from 40 to

350 Nmm^{-1}. The carpometacarpal and intermetacarpal ligaments are not listed in the tables below; these ligaments were assigned a stiffness of 100 Nmm^{-1}. These stiffness values chosen in the model were also in general agreement with Nowak's and Savelberg's ligament mechanical properties studies. [62,73]

$$Stiffness = Modulus * \frac{Width * Thickness}{Length} \qquad (3\text{-}5)$$

Ligaments were modeled as tension-only spring elements that provide no resistance to compression. COSMOSMotion does not have a tension-only spring element feature built into the program, it provides only simple spring elements that resist tension and compression. Therefore, an action-reaction force vector was applied connecting insertion and origin of each ligament, and a custom FORTRAN code written as an *If* statement was used to express tension in terms of the stiffness, displacement, and stress free length (Equation 3-6).

If((Lig. Length)-(Zero Length): 0, 0, Stiffness*((Lig. Length)-(Zero Length))) (3-6)

Table 3.6.1: Extrinsic Ligament Mechanical Properties

	Abbreviation	Ligament Name	Stiffness (N/mm)	Total Ligament Stiffness (N/mm)
Palmar	LRL-L	Long Radiolunate-Lateral	18.75	37.5
	LRL-M	Long Radiolunate-Medial	18.75	
	RC-L	Radiocapitate-Lateral	25	50
	RC-M	Radiocapitate-Medial	25	
	RS-L	Radioscaphoid-Lateral	25	50
	RS-M	Radioscaphoid-Medial	25	
	SRL-L	Short Radiolunate-Lateral	18.75	37.5
	SRL-M	Short Radiolunate-Medial	18.75	
	UC-L	Ulnocapitate-Lateral	25	50
	UC-M	Ulnocapitate-Medial	25	
	UL-L	Ulnolunate-Lateral	20	40
	UL-M	Ulnolunate-Medial	20	
	UT-L	Ulnotriquetrum-Lateral	20	40
	UT-M	Ulnotriquetrum-Medial	20	
Dorsal	DRC-D	Dorsal Radiocarpal-Distal	37.5	75
	DRC-P	Dorsal Radiocarpal-Proximal	37.5	

The FORTRAN code written in COSMOSMotion required the use of a result plot that tracked the instantaneous magnitude of the distance between the insertion and origin points of each ligament. This distance was automatically inserted into the force function given in Equation 3-6 at each time step. The zero length was the measured distance between the two points where the ligament force vector would be applied present in the model as it was scanned. The function then calculated the difference between the two lengths and used this value to calculate the force in the ligament. If the ligament length is longer than the stress free length, the force is calculated by multiplying the spring stiffness by the difference in the distance. If the ligament length is equal to or shorter than the zero length, there is no tension developed.

Table 3.6.2: Intrinsic Ligament Mechanical Properties

	Abbreviation	Ligament Name	Stiffness (N/mm)	Total Ligament Stiffness (N/mm)
Midcarpal	DIC-D	Dorsal Intercarpal-Distal	25	50
	DIC-P	Dorsal Intercarpal-Proximal	25	
	PH-D	Pisohamate-Distal	25	50
	PH-P	Pisohamate-Proximal	25	
	SC-D	Scaphocapitate-Distal	20	40
	SC-P	Scaphocapitate-Proximal	20	
	STT-L	Scaphotrapeziotrapezoidal-Lateral	50	150
	STT-C	Scaphotrapeziotrapezoidal-Central	50	
	STT-M	Scaphotrapeziotrapezoidal-Medial	50	
	TC-D	Triquetrocapitate-Distal	20	40
	TC-P	Triquetrocapitate-Proximal	20	
	TH-L	Triquetrohamate-Lateral	25	50
	TH-M	Triquetrohamate-Medial	25	
	FR-1	Flexor Retinaculum-1	32.5	130
	FR-1	Flexor Retinaculum-2	32.5	
	FR-1	Flexor Retinaculum-3	32.5	
	FR-1	Flexor Retinaculum-4	32.5	
Interosseous	DCH-D	Dorsal Capitohamate-Distal	81.3	325
	DCH-P	Dorsal Capitohamate-Proximal	81.3	
	PCH-D	Palmar Capitohamate-Distal	81.3	
	PCH-P	Palmar Capitohamate-Proximal	81.3	
	DCT-D	Dorsal Capitotrapezoid-Distal	75	300
	DCT-P	Dorsal Capitotrapezoid-Proximal	75	
	PCT-D	Palmar Capitotrapezoid-Distal	75	
	PCT-P	Palmar Capitotrapezoid-Proximal	75	
	DLT-D	Dorsal Lunotriquetral-Distal	87.5	350
	DLT-P	Dorsal Lunotriquetral-Proximal	87.5	
	PLT-D	Palmar Luntotriquetral-Distal	87.5	
	PLT-P	Palmar Luntotriquetral-Proximal	87.5	
	PT1	Pisotriquetral-1	25	100
	PT2	Pisotriquetral-2	25	
	PT3	Pisotriquetral-3	25	
	PT4	Pisotriquetral-4	25	
	DSL-D	Dorsal Scapholunate-Distal	57.5	230
	DSL-P	Dorsal Scapholunate-Proximal	57.5	
	PSL-D	Palmar Scapholunate-Distal	57.5	
	PSL-P	Palmar Scapholunate-Proximal	57.5	
	DTT-D	Dorsal Trapeziotrapezoidal-Distal	37.5	150
	DTT-P	Dorsal Trapeziotrapezoidal-Proximal	37.5	
	PTT-D	Palmar Trapeziotrapezoidal-Distal	37.5	
	PTT-P	Palmar Trapeziotrapezoidal-Proximal	37.5	

Each ligament component also included a damping element to resist rapid development of ligament tension. The damper tool in COSMOSMotion was used to apply a linear damping coefficient of 0.25 N*s/mm to each straight line distance between origin and insertion point. The force provided by the damper is proportional to the velocity acting in the opposite direction of the two bone's relative motion. This damper does provide some viscoelastic behavior, but the function of the damper was to prevent high speed motion in the computational model, not provide physiologic time dependant behavior.

3.7 MUSCULAR STRUCTURES

The four prime wrist motors represented in this study include the ECRL, ECU, FCR and FCU. The FCR and FCU loaded together produces flexion, the ECRL and ECU loaded together produces extension, the FCR and ECRL loaded together produces radial deviation, and the loading the ECU produces ulnar deviation. Active contractions of these muscles were modeled by straight line, constant magnitude force vectors inserted onto their respective bony insertions and directed toward their respective bony origins. Due to limitations in the COSMOSMotion modeling package, the computational model was unable to account for the wrapping of tendons. Therefore, MIMICS was used to isolate each distal muscle tendon (Figure 3.7-1) and muscle forces were directed along the shortened tendons (Shown in Chapter 4). Tendons were located in MIMICS by using the anatomic texts and descriptions provided in Chapter 2.

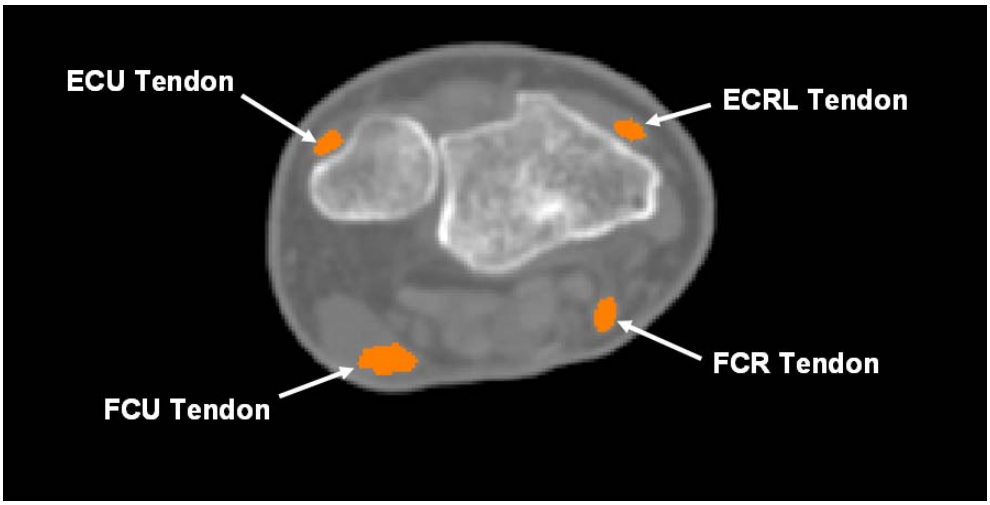

Figure 3.7-1: Cross-sectional view of muscle tendons in MIMICS

When possible, the muscle force vectors were shortened to coincide with the proximal termination of the flexor and extensor retinacula. Because the retinacula act as a fulcrum for the tendons, the force vectors were then lying on the physiological line of action for this tissue and the redirection and wrapping of the tendons could be neglected. For instance, the FCR is firmly fixed in a fibro-osseous groove formed in part by the tuberosity of the scaphoid and trapezium. This tendon travels directly underneath of the flexor retinaculum, and upon exit, it travels proximally up the forearm and wraps around the radius and ulna to its insertion on the humerus. For modeling simplicity, the line of action origin was located where this tendon exits the carpal tunnel. A similar modeling approach was taken for the FCU and for the extensor tendons on the dorsum of the hand. The values of the muscular soft-tissue structures modeled are given in Table 3.7.1. A translational damper of 15 N/sec*mm was also added to each muscle force. The damper helped to control rapid acceleration and prevent ringing between bodies. The dampers do not affect the end position of the bodies, only the time required to reach the final state.

Table 3.6.1: Muscle Mechanical Properties

Abbreviation	Muscle Name	Anatomic Origin	Model Origin	Insertion	Force (N)
FCR-L	Flexor Carpi Radialis, Lateral Insertsion	Medial epicondyle of the humerus (common flexor tendon)	FCR tendon where tendon exits carpal tunnel	Second and third metacarpal base	11.12
FCR-M	Flexor Carpi Radialis, Medial Inerstion				11.12
FCU-L	Flexor Carpi Ulnaris, Lateral Insertion	Medial epicondyle of the humerus (common flexor tendon) and medial border of olecranon	FCU tendon at distal ulna	Pisiform	11.12
FCU-M	Flexor Carpi Ulnaris, Medial Insertion				11.12
ECRL-L	Extensor Carpi Radialis Longus, Lateral Insertion	Lower one-third of the lateral supracondylar ridge of the humerus	ECRL tendon where tendon passes proximal extent of extensor retinaculm	Dorsum of the second metacarpal base	11.12
ECRL-M	Extensor Carpi Radialis Longus, Medial Insertion				11.12
ECU-L	Extensor Carpi Ulnaris, Lateral Insertion	Lateral epicondyle of the humerus (common extensor tendon)	ECU tendon where tendon passes proximal extent of extensor retinaculm	Fifth metacarpal base (medial side)	11.12
ECU-M	Extensor Carpi Ulnaris, Medial Insertion				11.12

4. RANGE OF MOTION STUDY

Pervaiz and colleagues performed a cadaveric study analyzing the range of motion effects of distal pole scaphoid excision and triquetral excision following radioscapholunate (RSL) fusion. [65] RSL fusion is a proven surgical procedure for treatment of isolated radiocarpal arthritis that alleviates pain and stiffness, however, it significantly reduces wrist motion results which is a common complaint of patients receiving the procedure. This experimental study was thus performed on cadaveric upper extremities to evaluate different techniques to improve the motion. The results of the cadaveric study and computational model were compared and used to validate the model.

4.1 CADAVERIC STUDY

A brief description of the cadaveric study performed previously is given [65]. Ten fresh-frozen, upper-extremity cadaver specimens ages 49 to 81 (Average age 65 ± 13) were used. All specimens were free of any evidence of wrist trauma, arthritis, or previous surgery. A custom designed apparatus (Figure 4.1-1) was used to hold each specimen, as well as provide weight activated motion of the wrist. The radius and ulna were fixed in a vertical position while the tendons of the FCR, FCU, ECRL, and ECU were loaded by way of a synthetic wire and five pound weight in sequence to produce flexion, extension, radial deviation and ulnar deviation. The FCR and FCU were loaded together to reproduce flexion, the ECRL and ECU together to

reproduce extension, the FCR and ECRL together to reproduce radial deviation, and the ECU to reproduce ulnar deviation.

Two-dimensional photographs were used to track the movement of black markers placed strategically in the bones (two on the long axis of the radius and two on the long axis of the third metacarpal) and measure the range of motion of the wrist complex (Figure 4.1-1). The digital photographs were imported into Image J software (National Institutes of Health, Bethesda, MD), and the angles between the two sets of markers were measured to calculate flexion-extension and radial-ulnar deviation range of motion.

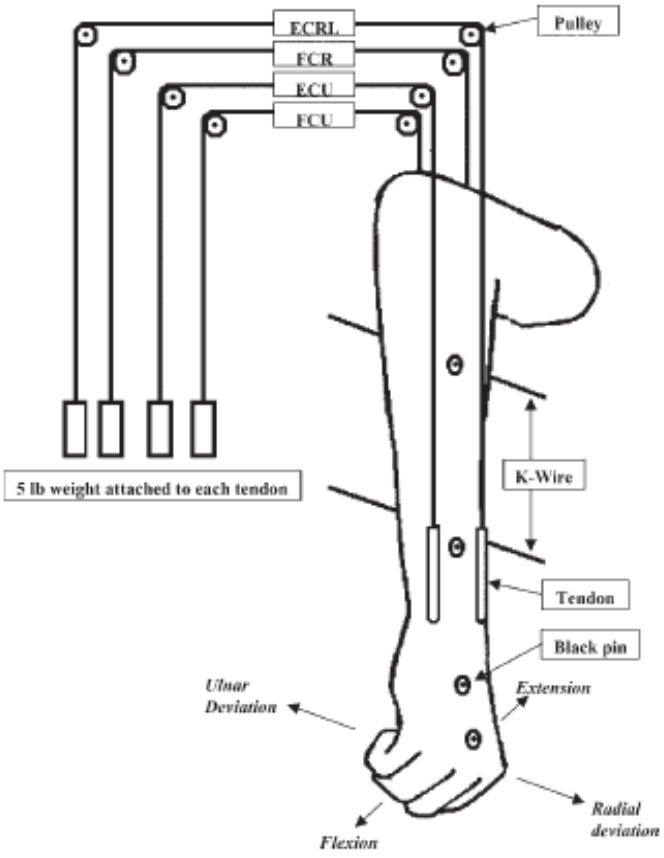

Figure 4.1-1: Schematic of loading apparatus [65]

Figure 4.1-2: Radiographs of RSL fusion (A), distal pole excision (B) and triquetral excision (C) [65]

The range of motion study was conducted for four specific states: intact (normal), RSL fusion, RSL fusion with distal scaphoid pole excision, and RSL fusion with distal pole excision and triquetrum excision. To represent the RSL fusion state, two 0.0625 inch K-wires were drilled across both the radioscaphoid and radiolunate joints to fix the radiocarpal joint (Figure 4.1-2). Scaphoid distal pole excision was accomplished by an osteotomy just distal to the waist of the scaphoid. After removal of the distal pole, the volar capsule and ligaments were repaired using 4-0 sutures. Finally, the triquetrum was excised and all excisions were checked via radiograph (Figure 4.1-2).

Thus, the digital images provided experimental data for four motions and positions of the wrist – flexion, extension, radial deviation, ulnar deviation – in four states of the wrist complex – intact, RSL fusion, RSL fusion + distal pole excision, RSL fusion + distal pole excision + triquetral excision.

4.2 COMPUTATIONAL MODEL METHODS

The experimental procedure described by Pervaiz et al was replicated in the 3-D SolidWorks design space. Just as in the experimental study, the radius and ulna were fixed and constrained from motion. This was achieved simply by using the “fix” feature native to SolidWorks. “Fixing” a bone in the design space prevents the part from moving, while all other bones in the carpus were free to move or “float”. The third metacarpal was mated or “fixed” to the capitate bone. It has been proven that the third metacarpal and capitate move as one unit, and in the model the bones did not move relative to each other.[64] All soft-tissues present in the cadaveric study were actively modeled as appropriate in the computational study. This included all ligaments being activated, and the muscle force vectors being loaded alternately to produce flexion, extension, radial deviation and ulnar deviation. Two constant force vector values of 11.12 N (22.24 N total) were assigned to each tendon modeled to represent the tension of the 5 lb weight hung on the FCR, FCU, ECRL, and ECU tendons in the experimental study (Figures 4.2-1 and 4.2-2). The two blue arrows represent the muscle force vector in the COSMOSMotion module. These two force vectors represent the medial and lateral margins of the tendons and the line of action of the muscle tendon. The FCR and FCU were loaded together to reproduce flexion, the ECRL and ECU to produce extension, the FCR and ECRL for radial deviation, and the ECU for ulnar deviation as stated previously. Flexion/extension and radial/ulnar deviation angle was recorded for each wrist surgical state.

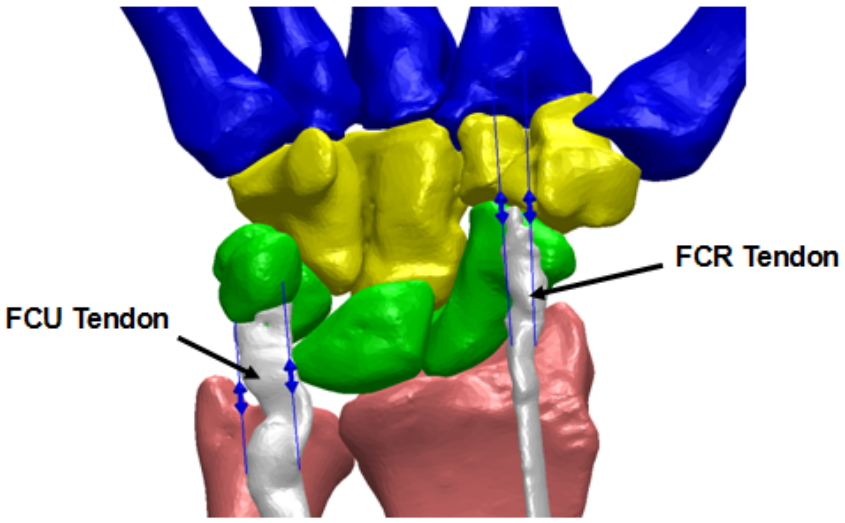

Figure 4.2-1: Muscle force vectors along respective flexion muscle tendons

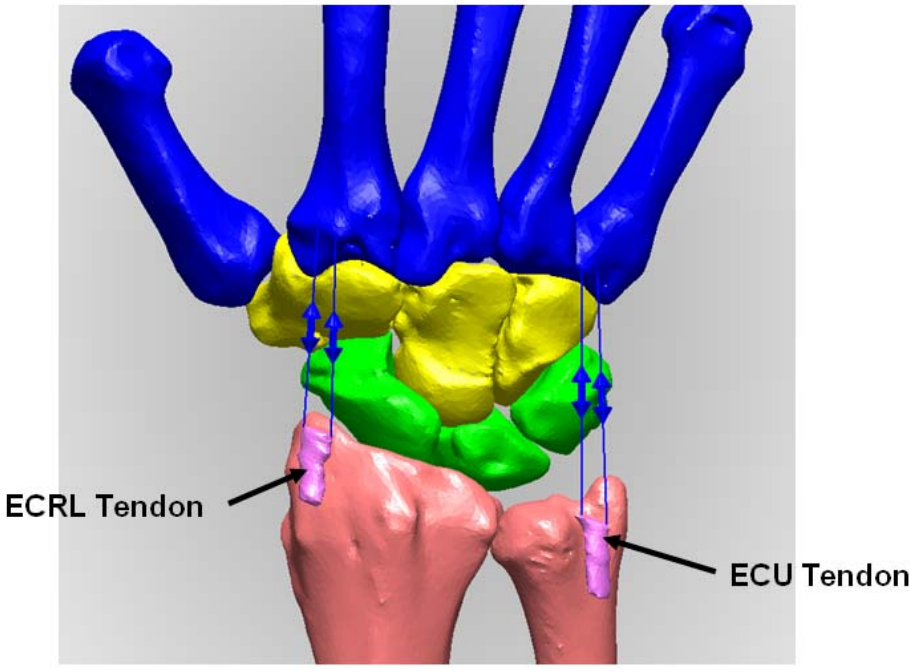

Figure 4.2-2: Muscle force vectors along respective extension muscle tendons

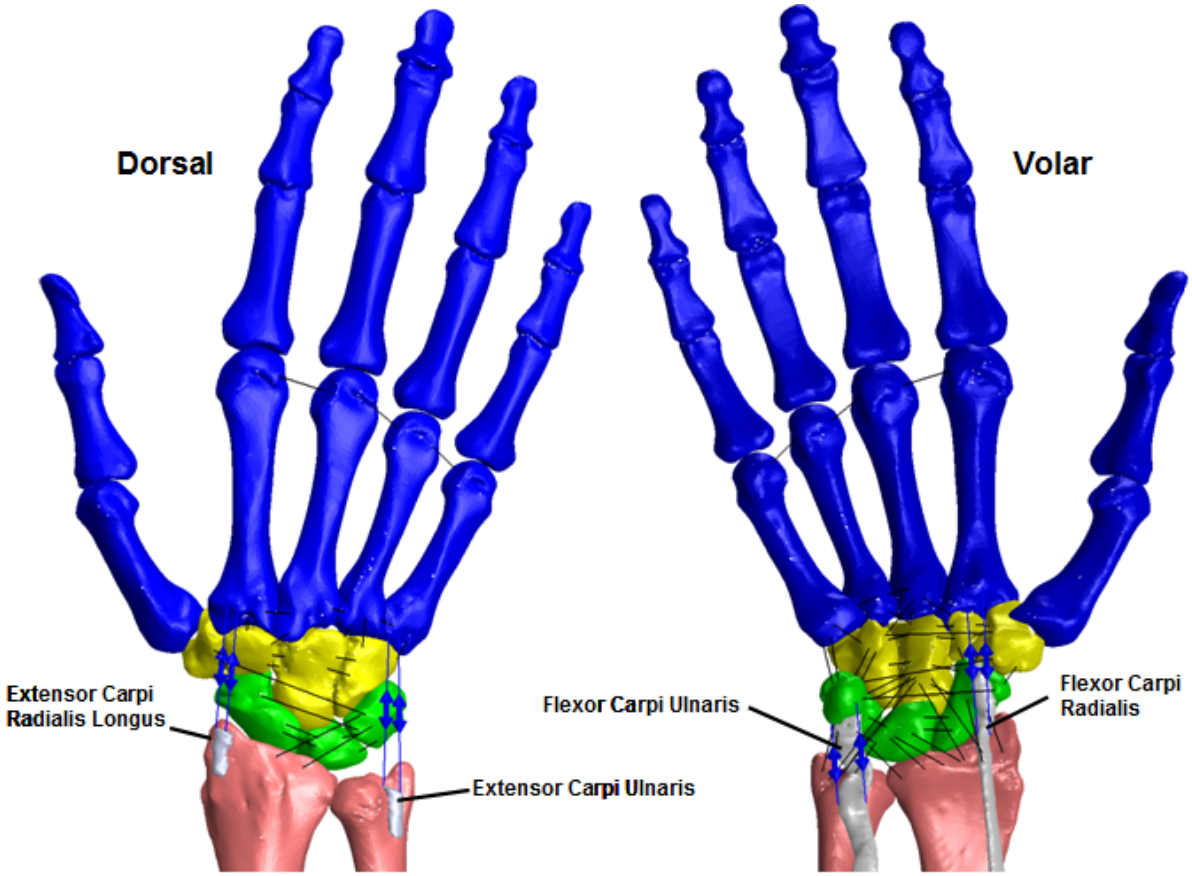

Figure 4.2-3: Volar and dorsal view of model with all bones and constraints present

4.2.1 Data Acquisition

Pervaiz and colleagues imported two dimensional digital photographs into the Image J software to measure flexion/extension angle in the coronal plane and radial/ulnar deviation in the sagittal plane. Similarly, lines created in the SolidWorks design space were used to track the motion of the wrist joint complex (Figure 4.2-4). For flexion and extension, two lines were created in the coronal plane; one line was drawn parallel to the long axis of the radius, while the second was drawn parallel to the long axis of the third metacarpal as defined by the ISB (Chapter 3). The angle between these two lines was tracked to determine the range of motion of the wrist

joint. Likewise, the radial and ulnar deviation angle was calculated by tracking the angle between two lines drawn along the long axis of the radius and the long axis of the third metacarpal in the sagittal plane (Figure 4.2-4).

In order to track the angle between the flexion/extension and radial/ulnar deviation lines, a result plot was used to measure the angle at every time step. Measurements taken at every time step were needed to ensure that the simulation time was sufficient for the model to reach an equilibrium state. In COSMOSMotion, angles can be plotted using the angular displacement result plot tool. For these plots to track the angle between the radius and the third metacarpal, three points are needed: one on each of the long axis lines and the point of intersection between the two lines (Figure 4.2-5). Therefore, two different angular displacement result plots were needed: flexion/extension angle and radial/ulnar deviation angle in the coronal and sagittal planes, respectively. Flexion angle for the intact state of the wrist is demonstrated below. These result plots were used to track the motion for the four surgical states: intact, RSL fusion, RSL fusion plus scaphoid distal pole excision, and RSL fusion with scaphoid distal pole excision plus triquetral excision.

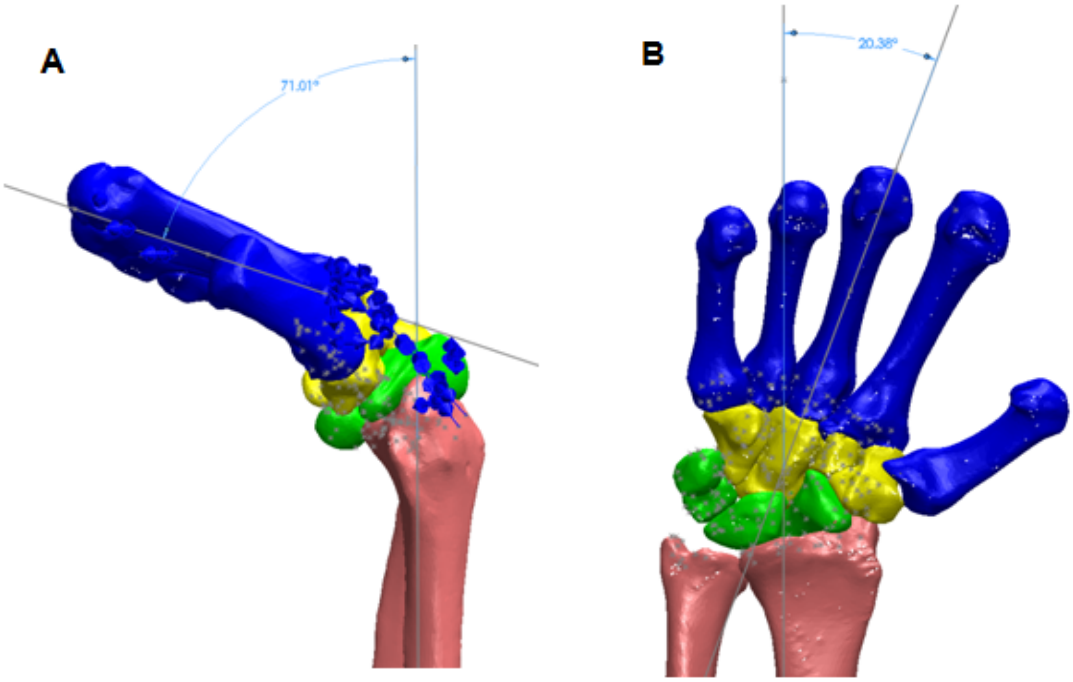

Figure 4.2-4: Flexion angle in the coronal plane (A) and radial deviation angle in the sagittal plane (B)

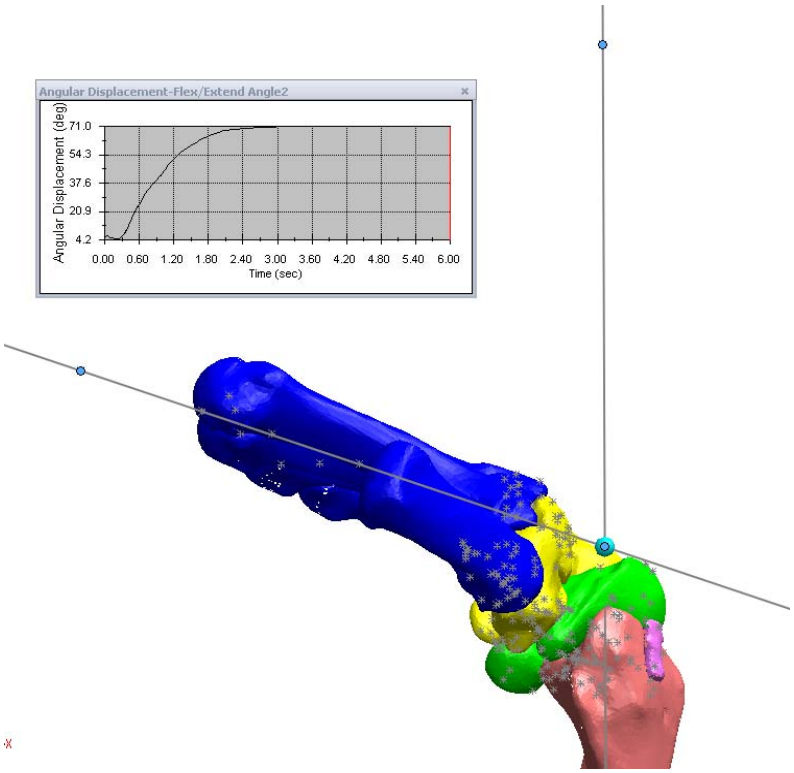

Figure 4.2-5: Result plot feature of COSMOSMotion demonstrating flexion angle

4.2.2 RSL Fusion, Scaphoid Distal Pole and Triquetrum Excision Replication

The wrist was imported into the design space in an intact state. The cadaver specimen used to develop the model was free of any obvious trauma or previous surgeries. Therefore, the model in the design space is already in the intact (normal) state with all bones of the carpus present and free to move with motion dictated by modeled ligamentous and muscular soft tissues. In the experimental study, RSL fusion was simulated by using K-wires to fix the scaphoid and lunate to the radius. In the computational model, RSL fusion was achieved by simply "mating" the scaphoid and lunate to the radius. The "mate" feature in Solidworks creates a junction between the three bones, and because the radius is fixed in space, the three bones are fixed in space (Figure 4.2-6). Once activated, the radius, scaphoid, and lunate will not move with respect to all other bones in the wrist joint complex. In the figure below, the highlighted purple bones (scaphoid and lunate) are "fused" to the orange bone (radius).

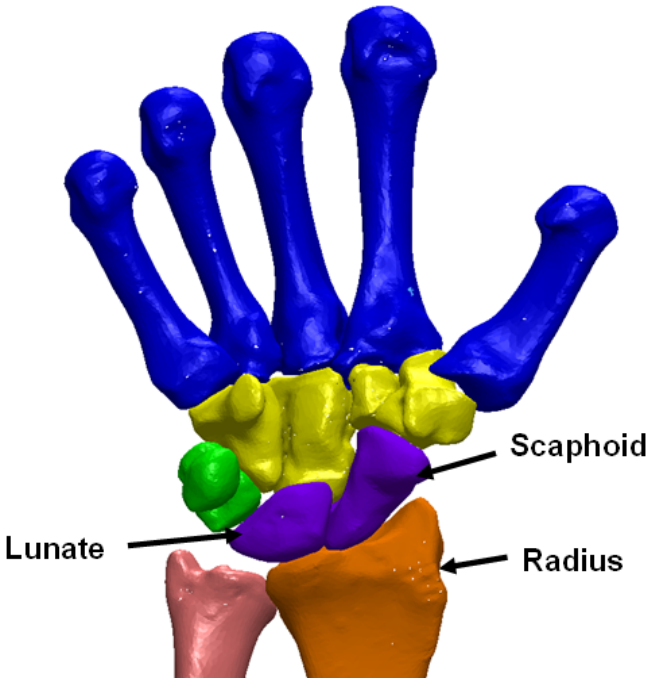

Figure 4.2-6: Simulated RSL fusion in computational model

Pervaiz et al went on to excise the distal pole of the scaphoid via volar approach. Digital radiographs taken post osteotomy showed approximately 50% resection. The osteotomy level was marked just distal to the waist of the scaphoid, and the cut was performed perpendicular to the long axis of the scaphoid in sagittal plane. In order to replicate the procedure followed by the experimental study, the scaphoid was duplicated into two different configurations. Solidworks allows creation of different part configurations with the ability to interchange these parts seamlessly. Therefore, the normal intact scaphoid and distal pole excised state could be interchanged without creating an entirely new model for this surgical state or altering any other features of the model.

For the alternate model configuration, the distal pole was excised by first creating a line representative of the long axis of the scaphoid in the sagittal plane (Figure 4.2-7). A second plane, perpendicular to the long axis, was created that intersected the scaphoid just distal to the waist. This plane was used to cut the distal portion of this part and delete the distal pole in this configuration. Distal pole excision was comparable between the model (Figure 4.2-8), the experimental study (Figure 4.1-2), and postoperative surgical results [5].

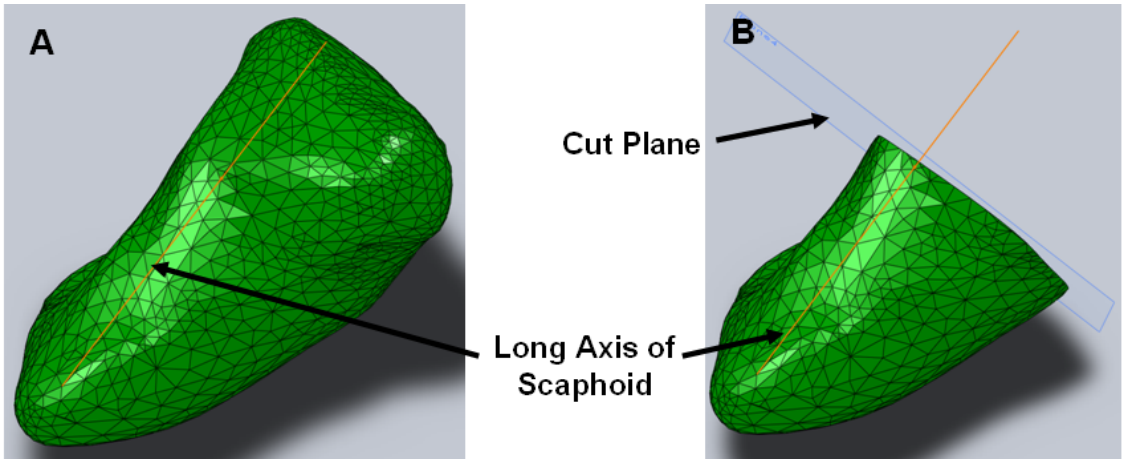

Figure 4.2-7: Scaphoid bone taken out of model (A) and distal pole excised (B)

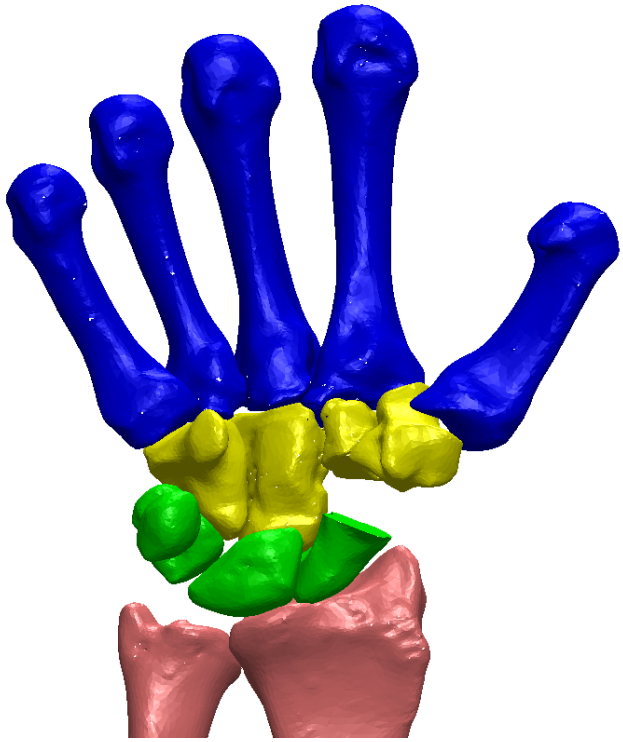

Figure 4.2-8: Scaphoid distal pole excised in computational model

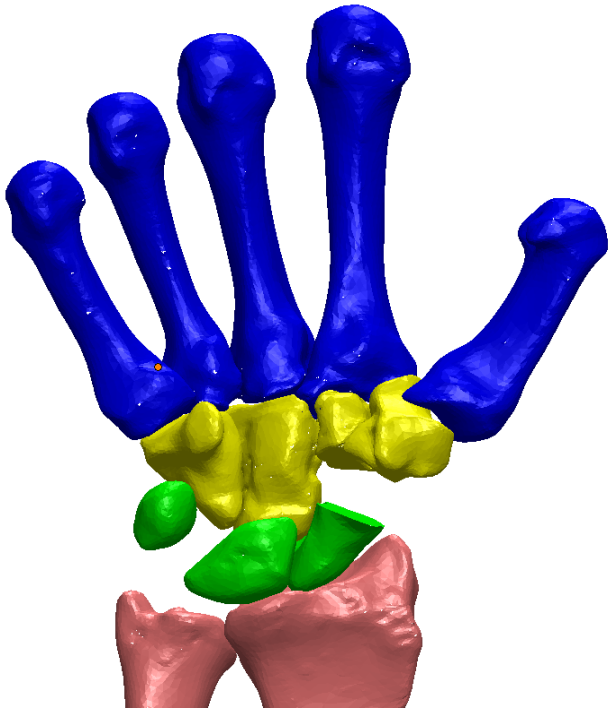

Figure 4.2-9: Representation of triquetral excision in computational model

The final surgical state included excision of the triquetrum. This was achieved experimentally by gentle cutting all of the ligaments attached to the bone and removing it through an incision in the dorsal capsule. This was reproduced in the Solidworks design space by suppressing the entire bone. When the bone is suppressed, it is removed from the design space, and therefore, all ligaments attached to the bone were also inactive (Figure 4.2-9).

4.3 RESULTS

COSMOSMotion was used to track and record a variety of variables in the model including angles, distances, and forces. The program's ability to track all of these variables simultaneously allows direct comparison of the results from multiple model configurations to one another. The range of motion of the model was tracked to directly compare the model to the cadaveric experiment. While this was the only parameter analyzed in the cadaveric experiment, other variables, including contact force and ligament tensions, can be predicted and used in hopes of locating potential areas of concern in other areas of the wrist.

Validation of the model was executed by comparing the range of motion results from sixteen individual 12 second simulations of the model for each surgical state to the results of the Pervaiz cadaver study. Just as was conducted in the cadaveric experiment, comparisons of the range of motion results in the normal, RSL fusion, RSL fusion with scaphoid distal pole excision, and RSL fusion with scaphoid distal pole excision and triquetral excision were calculated and exported in COSMOSMotion. Results for range of motion for both the cadaveric experiment and computational model are given in Figures 4.3-1 through 4.3-4. The results from the cadaveric experiment represent an average across ten specimens, and the error bars shown represent one standard deviation. Results plots were used to track angle with respect to time to obtain the angle measurements, and each plot was viewed to ensure that the model had reached a steady state and motion had ceased. These plots can be found in Appendix A.

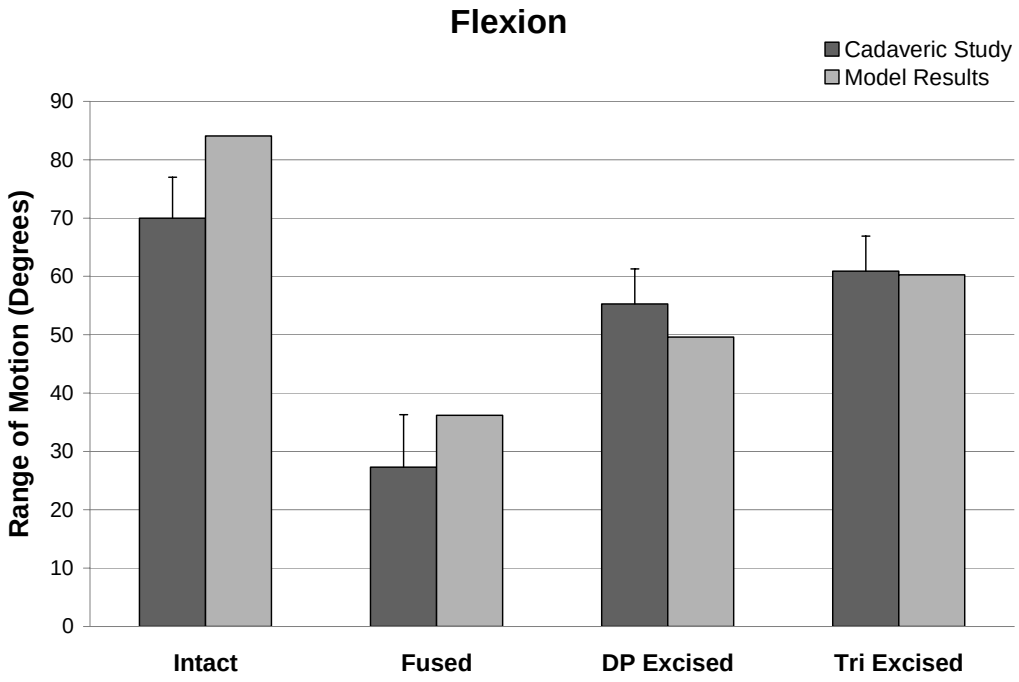

Figure 4.3-1: Flexion range of motion results comparison between cadaver and model

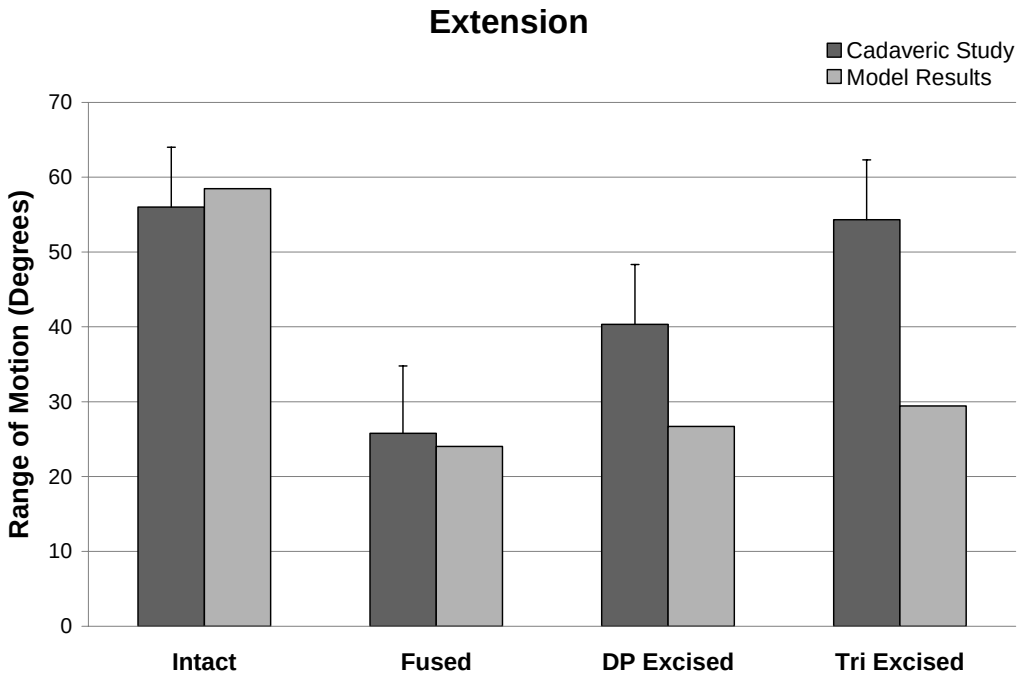

Figure 4.3-2: Extension range of motion results comparison between cadaver and model

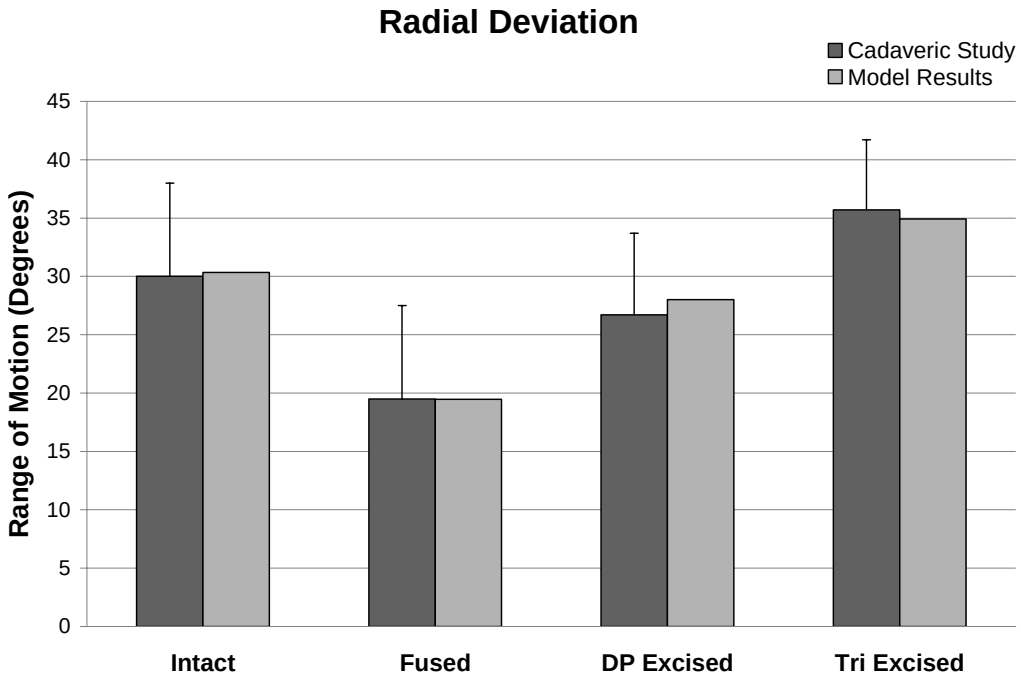

Figure 4.3-3: Radial deviation range of motion results comparison between cadaver and model

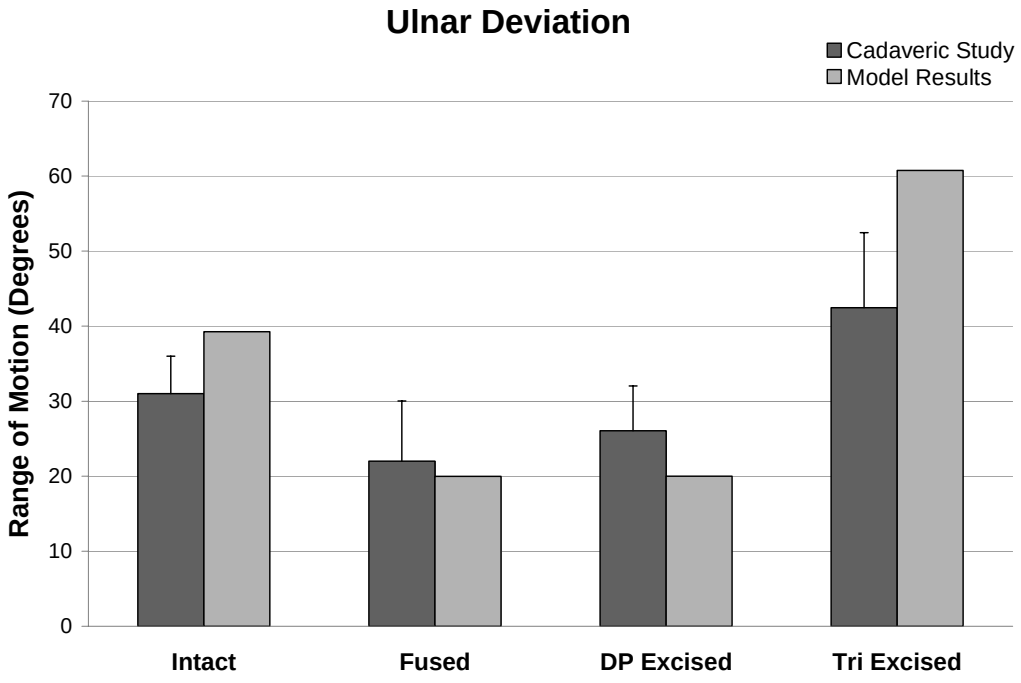

Figure 4.3-4: Ulnar deviation range of motion results comparison between cadaver and model

The range of motion values predicted by the model showed similar trends and magnitudes to those seen in the cadaveric experiment For the normal (intact) wrist, the model predicted 84° of flexion, 58° of extension, 30° of radial deviation, and 39° of ulnar deviation. Range of motion in the model decreased after simulated RSL fusion for each motion with results showing 43% of normal for flexion, 41% of normal for extension, 64% of normal for radial deviation, and 51% of normal for ulnar deviation. Distal pole excision after simulated RSL fusion resulted in increased range of motion for three of the four motions; range of motion increased to 59% of normal for flexion, 46% of normal for extension, and 92% of normal for radial deviation. Excision of the triquetrum coupled with RSL fusion and distal pole excision increased all four motions increasing flexion to 72% of normal, extension to 50% of normal, radial deviation to 115% of normal, and ulnar deviation to 155% of normal.

In flexion, the model was accurately able to reproduce the trend relationship between the normal and surgically altered states Figure (4.3-1). Motion decreased following RSL fusion, and then increased with subsequent distal pole and triquetral excision. Motion increase was greatest following distal scaphoidectomy and modest gains were seen following triquetrectomy, emulating experimental results. Only the intact (normal) results fell outside of one standard deviation of the measured experimental results.

Although less pronounced, the model was also able to reproduce the same trends in extension. The normal (intact) state and RSL fusion state magnitudes were predicted to be within one standard deviation of the experimental results. Following RSL fusion, the model accurately predicted the loss in motion. Subsequent scaphoid distal pole excision and triquetral excision brought modest gains, however (Fig. 4.3-2).

The computational model and the experimental study showed nearly identical trends and magnitudes in radial deviation, as each simulation was within the cadaver study's standard deviation (Fig. 4.3-3). Model motion decreased following RSL fusion, and increased with scaphoid distal pole excision and triquetral excision, with motion improving most after distal pole excision. Radial deviation predictions correlate the best with experimental measurements.

In ulnar deviation, the model was able to accurately reproduce the trends seen in the experiment (Figure 4.3-4). Range of motion following RSL fusion matched that of the Pervaiz study, and the model showed minimal improvement following scaphoid distal pole excision, reinforcing the lack of a statistical difference found between the two states in the experiment. Normal (intact) and triquetral excision states were over-predicted by the model.

The surgically altered experimental and computational model ROM results are presented as a percentage of the intact range of motion state (Table 4.3.1). The trend for changes to motion in all states as predicted by the model correlate well with the experimental findings with most values within the reported range.

Table 4.3.1: Range of motion for intact wrist and percentage of normal for repaired states

	Intact (Normal)	RSL Fusion	Scaphoid DP Excised	Triquetrum Excised
Flexion				
Cadaveric Study	70°±7	39% (26% - 51%)	79% (70% - 87%)	87% (77% - 94%)
Computational Model	84°	43%	59%	72%
Extension				
Cadaveric Study	56°±8	46% (30% - 63%)	72% (57% - 85%)	97% (82% - 111%)
Computational Model	58°	41%	46%	50%
Radial Deviation				
Cadaveric Study	30°±8	65% (40% - 93%)	89% (67% - 113%)	119% (100% - 140%)
Computational Model	30°	64%	92%	115%
Ulnar Deviation				
Cadaveric Study	31°±5	71% (45% - 97%)	84% (65% - 103%)	137% (106% - 171%)
Computational Model	39°	51%	51%	155%

An advantage of computational models is the ability to predict other parameter measures that are not or cannot be easily obtained in experimental studies. SolidWorks and COSMOSMotion were able to track the forces at the midcarpal joint, and present the results in graphical form. In the computational model, the forces at the midcarpal joint were calculated to locate potential areas of arthritic development caused by increases in force as a result of surgical alteration.

In flexion, the forces at the scaphoid-trapezoid articular facet and triquetrum-hamate articulation in the RSL fusion state were more than double what was predicted in the normal state. Distal pole excision relieved the increased pressure at these joints to totals lower than what was predicted computationally in the normal state (Fig. 4.3-5). Scapho-capitate and lunate-hamate contact forces rose sharply with triquetral excision.

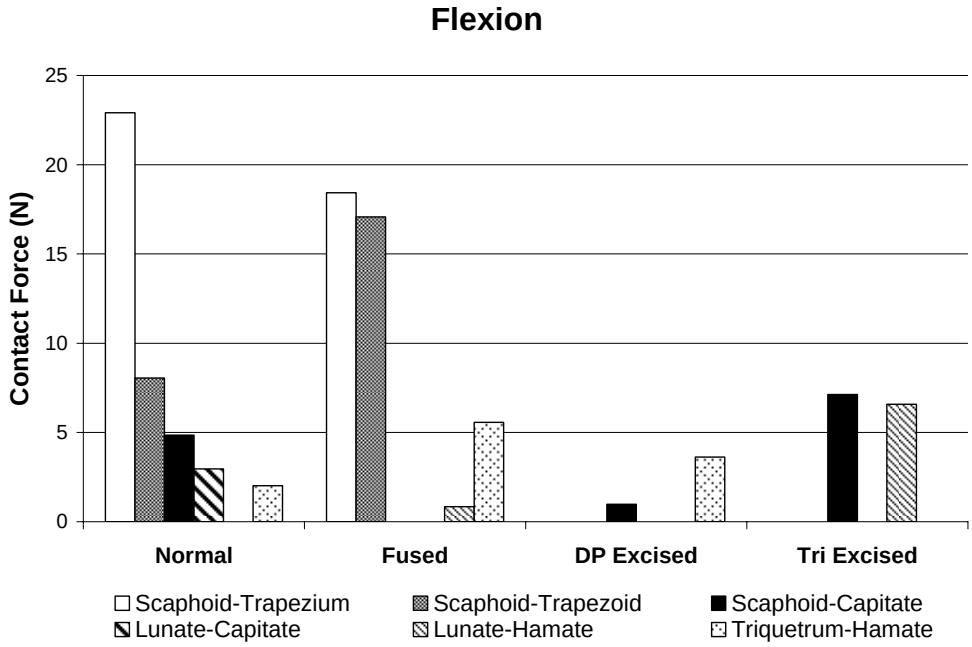

Figure 4.3-5: Contact force in joints predicted by computational model during flexion

In extension, RSL fusion resulted in an increase in contact force at the lunate-capitate joint over intact levels, and this force was further increased to a predicted value twice the normal value when the distal pole and triquetrum were excised (Fig. 4.3-6). All other forces following surgical procedures were at or below their predicted normal values.

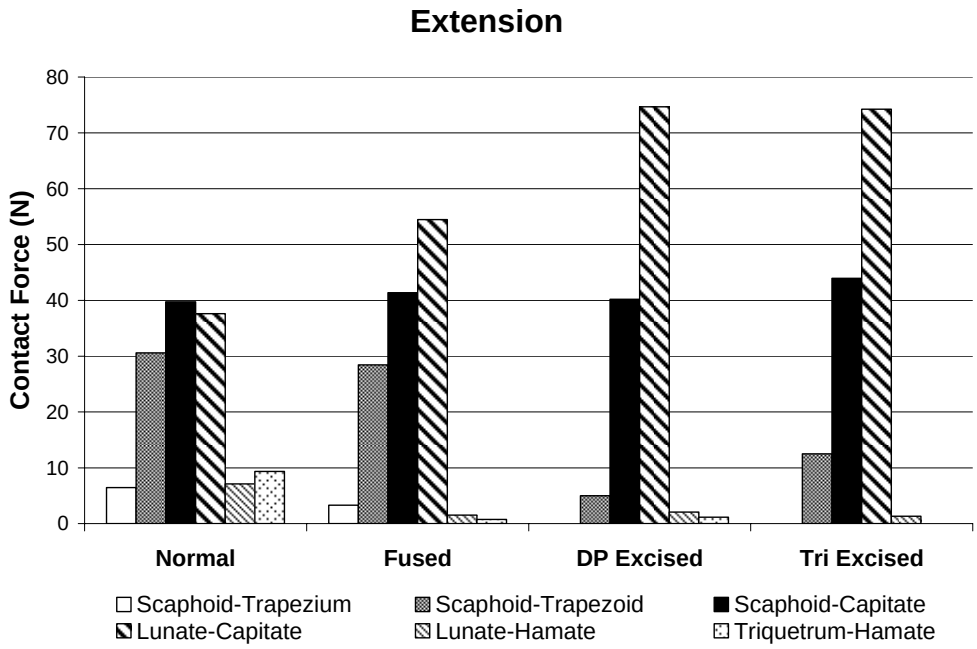

Figure 4.3-6: Contact force in joints predicted by computational model during extension

Radial deviation model results showed an increase in force at the scaphoid-trapezoid joint after RSL fusion over intact levels, and these increases were eliminated with excision of the distal pole. Following distal pole excision, the force at the lunate-capitate joint increased to twice the normal (intact) force (Fig. 4.3-7). The increase in force at the lunate-capitate joint was reduced to a normal value once the triquetrum was excised.

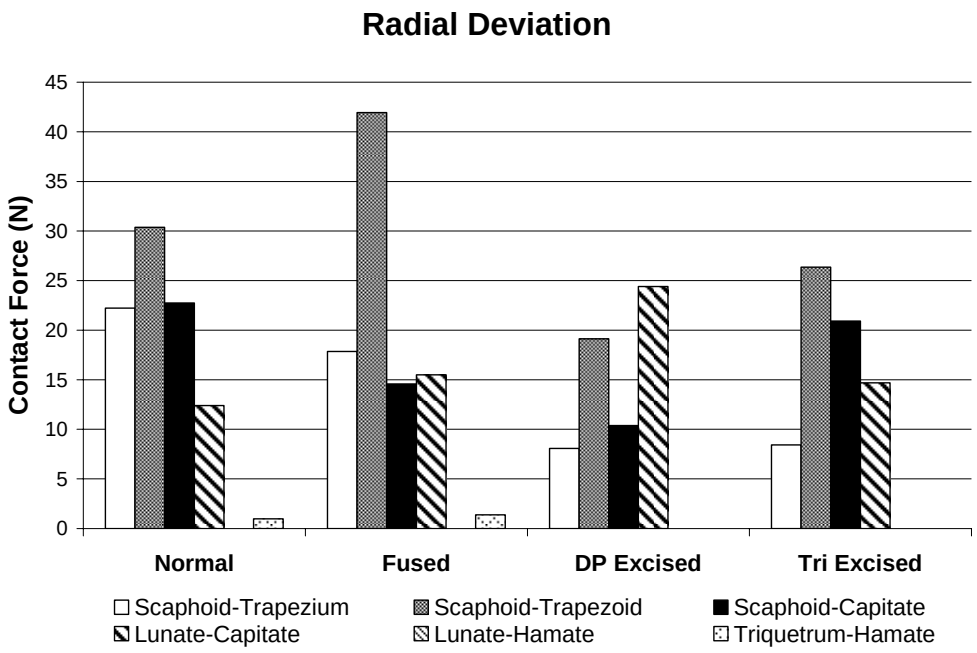

Figure 4.3-7: Contact force in joints predicted by computational model during radial deviation

Finally, in ulnar deviation, force increases were seen at the scaphoid-capitate joint after RSL fusion and at the lunate-hamate joint after scaphoid distal pole excision (Fig. 4.3-8). Neither of these force increases were reduced with subsequent scaphoid distal pole excision or triquetral excision.

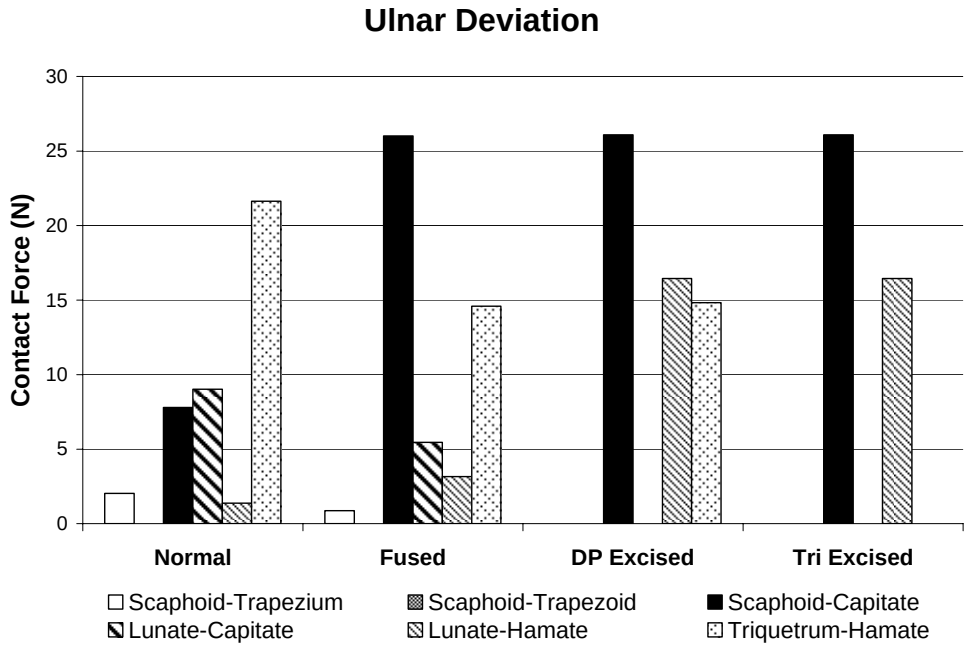

Figure 4.3-8: Contact force in joints predicted by computational model during ulnar deviation

COSMOSMotion was also used to track the tension in ligament elements for each of the surgical states across motions. Of particular interest in this study were the extrinsic and midcarpal intrinsic ligaments that do not insert on the triquetrum. This includes the scaphocapitate, radiocapitate, and ulnocapitate ligaments. Each ligament had a lateral and medial fiber, and the total ligament tension was calculated as the sum of its fibers.

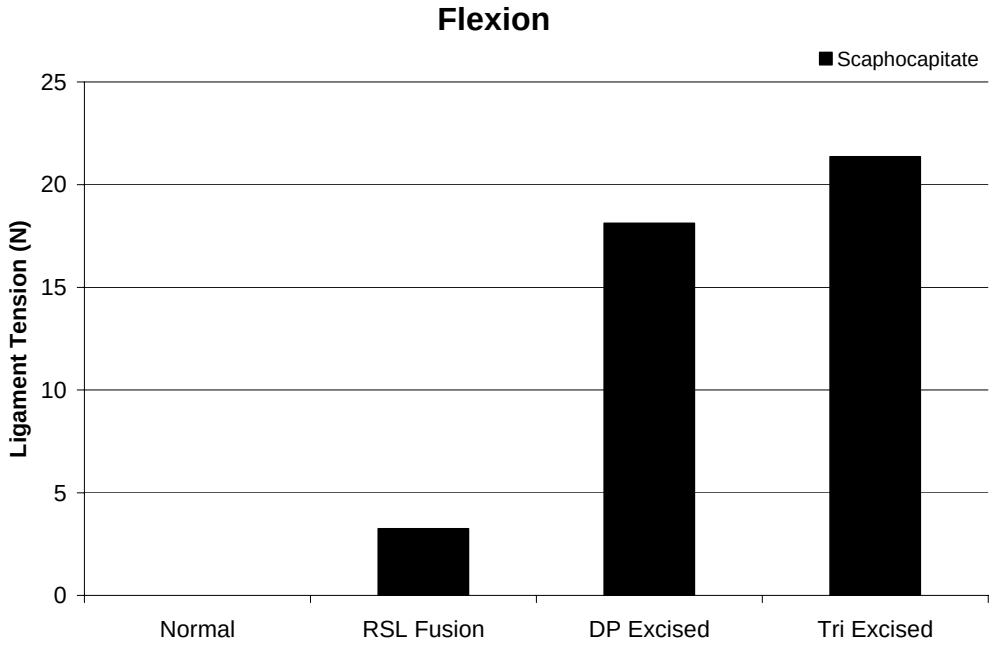

Figure 4.3-9: Magnitude of the scaphocapitate ligament tension developed during flexion

The total tension developed in the scaphocapitate ligament during flexion across surgical states is shown in Figure 4.3-9. The SC ligament showed no tension in the normal state, but following RSL fusion, the tension in the ligament increased with each subsequent surgical change up to 21.4 N following triquetral excision. A sharp increase in tension was seen following distal pole excision (3.3 N to 18.1 N). The RC and UC ligaments did not register tension in any of the surgical states during flexion.

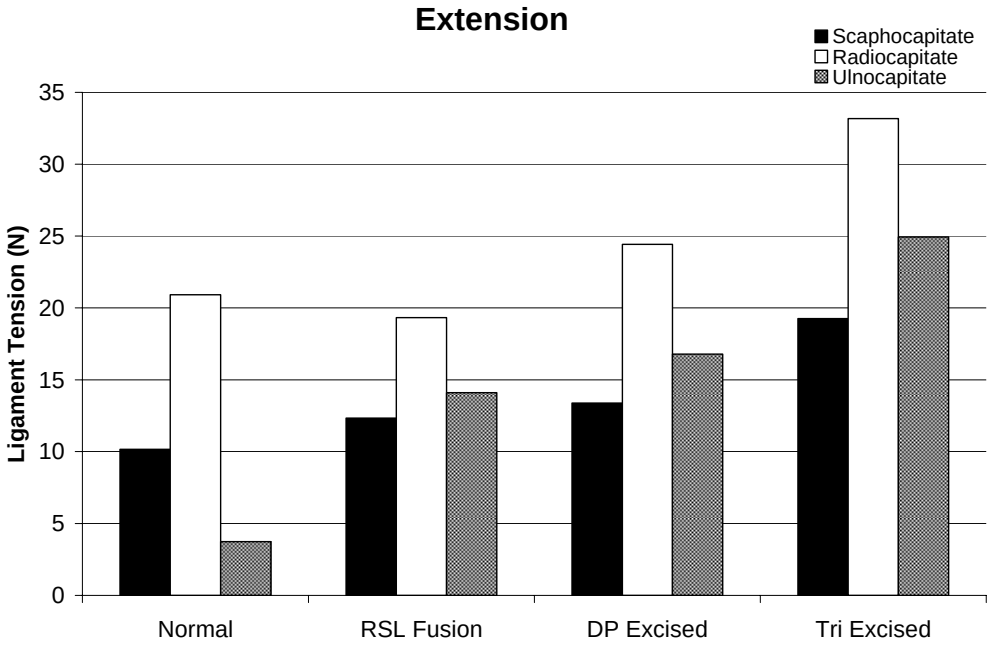

Figure 4.3-10: Magnitude of ligament tensions developed during extension

Total ligament tensions during extension are shown in Figure 4.3-10 as each ligament registered tensions across all surgical states. Ligament tension showed a clear trend of increasing from the normal state to triquetral excision. SC ligament tension showed a steady increase across surgical states and was nearly double the normal value following triquetral excision (10.2 N to 19.3 N). Radiocapitate tension following triquetral excision also predicted values higher than that of the normal state, as predicted tension increased 58% (20.9 N to 33.2 N). Ulnocapitate ligament tension showed the greatest increase between normal and triquetral excised state, as tension increased by nearly 7 times the normal value (3.7 N to 24.9 N).

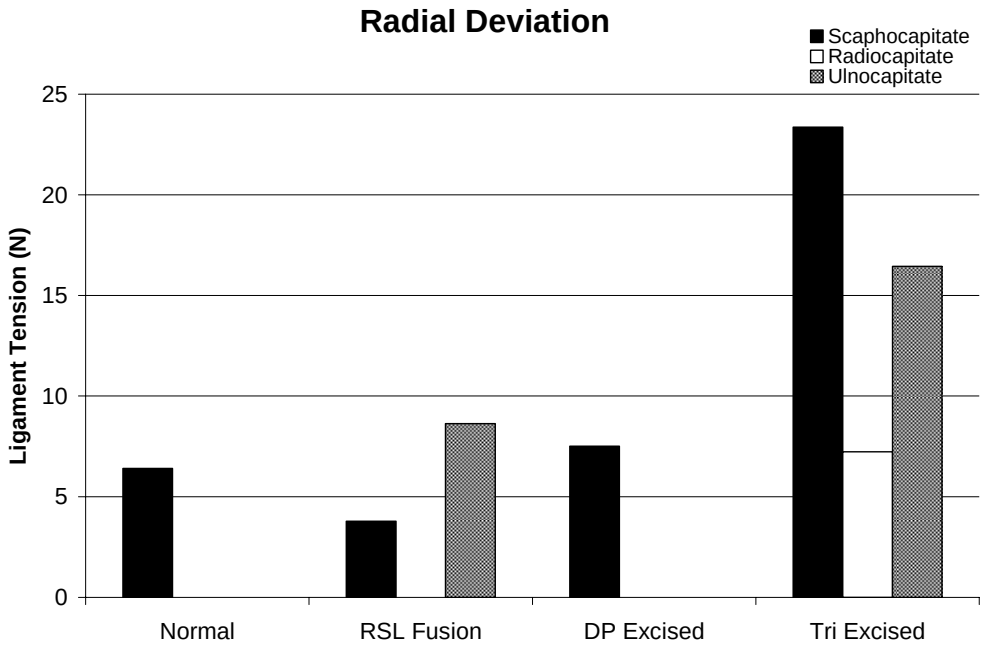

Figure 4.3-11: Magnitude of ligament tensions developed during radial deviation

In radial deviation, similar trends were seen as ligament tension increases were seen in all three ligaments following triquetral excision (Figure 4.3-11). Scaphocapitate ligament tension following triquetral excision was more than triple what it was predicted to be in a normal (intact) state. Radiocapitate tension was not present until after triquetral excision. Ulnocapitate ligament tension was not detected in the normal state, but showed values after RSL fusion (8.6 N) and following triquetral excision (16.4 N) representing a 90% increase in force between the two states.

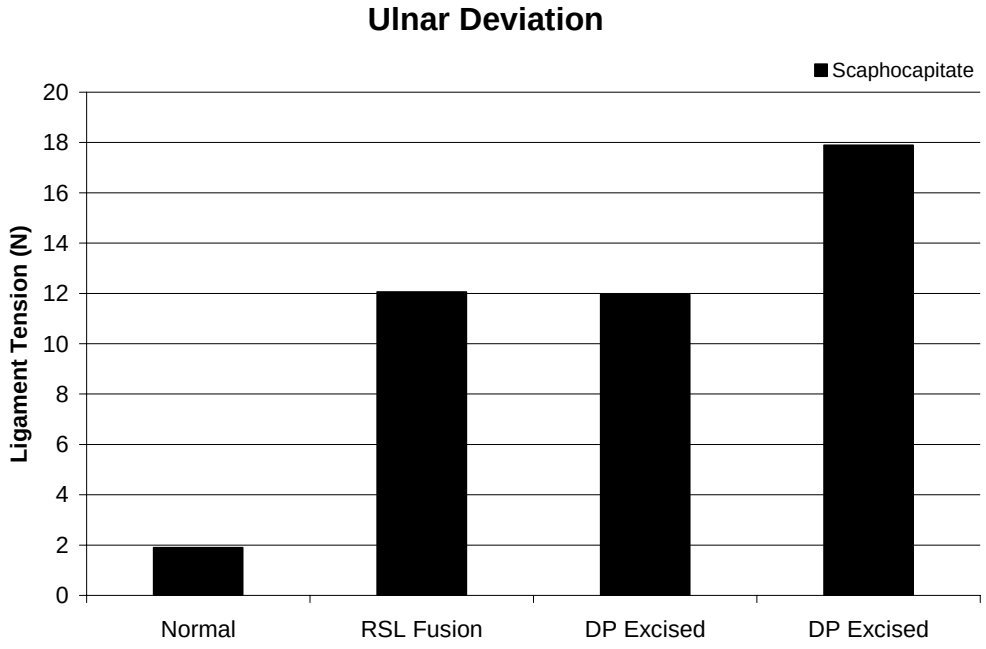

Figure 4.3-12: Magnitude of the scaphocapitate ligament tension developed during ulnar deviation

The total tension developed in the scaphocapitate ligament during ulnar deviation across surgical states is shown in Figure 4.3-12. A sharp increase in tension was seen following simulated RSL fusion, with a further increase after triquetral excision. Total ligament tension following simulated triquetrectomy was over nine times the normal (intact) ligament tension (1.9 N to 17.9 N). The RC and UC ligaments did not register tension in any of the surgical states during ulnar deviation.

4.4 DISCUSSION

The developed computational model was able to reproduce physiologic ranges and trends when compared to experimental results. Our computational model confirmed that RSL fusion significantly reduces motion of the wrist in all four directions, and motion improves following scaphoid distal pole excision and triquetral excision in all directions. Flexion and radial deviation motions improved most with distal pole excision, whereas ulnar deviation motion improved most after triquetral excision. In the computational model, extension did not show significant improvement with distal scaphoidectomy or triquetrectomy. Additionally, the computational model was able to show changes in the forces and tensions in the joints and ligaments, respectively, following RSL fusion, distal scaphoidectomy, and triquetrectomy.

Model range of motion prediction in the normal (intact) state was in general agreement with values obtained experimentally. Extension and radial deviation motions were predicted within one standard deviation and correlated well. Flexion over-prediction of motion was most likely due to the absence of additional soft tissue constraints found in the wrist that could not be modeled, such as skin, muscle tendon, and the extensor retinacula. The higher ulnar deviation prediction by the model can be explained by the absence of the restraint provided by the triangular fibrocartilage complex and its articular disc in the model. Even with over-prediction of motion being attributed to absence of various anatomical soft tissue structures, the motion arcs of the model are similar to other published range of motion experimental studies. Normal (intact) flexion predicted by the computational model was higher than that reported experimentally by Pervaiz *et al* [65] (84° vs 70°±7°), and normal (intact) extension motion was consistent with the experimental data (58° vs 56°±8°). While normal (intact) flexion prediction was higher, the computational flexion-extension arc prediction (142°) was well within the experimental

cadaveric flexion-extension arc measurements reported by McCombe *et al* and Berkhout *et al* [10,55] (141° ±9° and 149° ±19°, respectively). Similarly, normal (intact) radial deviation prediction by the model was exactly the same as the cadaveric experiment, but ulnar deviation was higher in the model. Berkhout measured a larger radial-ulnar deviation arc of 54° (±14°) which approached the model's predicted radial-ulnar deviation arc of 69°, while McCombe measured a smaller radial-ulnar deviation arc (49°±9°). Anatomical variations of the ligamentous anatomy and differences in the measurement and loading procedures could explain the differences between cadaveric specimens across studies.

The model predictions and measured experimental values for range of motion correlated well when simulating radioscapholunate fusion. Following RSL fusion, the scaphoid was not allowed to move relative to the radius and motion decreased substantially in all motion directions. All predicted values fell within one standard deviation of the experimental study, and the values are further validated by the measured motion arcs of Berkhout and McCombe [10,55].

The computational model results showed an increase in all four ranges of motion after scaphoid distal pole excision, with excision of the distal pole having more of an effect on flexion and radial deviation. Removal of the scaphoid distal pole frees up the midcarpal row, increasing motion in the joint. However, excision of the distal pole did not have much effect on extension in the model. Distal scaphoidectomy also did not have much of an effect on the ulnar side of the carpus, as reflected by minimal gains during ulnar deviation. The model did not show an increase in ulnar deviation motion after distal pole excision, which reinforces the lack of a statistical difference between the two surgical states in the experimental study [65].

Excision of the triquetrum brought further gains in range of motion, with its maximum effects on radial (115% motion restored) and ulnar (156% motion restored) deviations, as in the experimental study. This differed from the findings of Berkhout *et al*. [10] where triquetral excision restored the flexion-extension and radial-ulnar deviation arcs to only 88% and 98% of intact levels, respectively. The computational model predicted a 63% restoration of flexion-extension motion and 139% restoration of radial-ulnar deviation motion. Over-prediction of ulnar deviation was most likely due to absence of the triangular fibrocartilage complex.

The computational model was also able to predict carpal forces that could not be obtained easily experimentally without damaging native tissue. By fusing the scaphoid and lunate to the radius, the kinematics of the wrist are altered significantly. The bones of the proximal row do not act as a single unit, and motion of the wrist changes each bone's position through rotation and translation. RSL fusion introduces a blockade to midcarpal joint motion. Clinical studies have shown that, following RSL fusion, patients often develop midcarpal degenerative arthritis [33,59]. Subsequent scaphoid distal pole excision restores motion at the midcarpal joint, as previously shown [10,55,58,65], by removing a strong lever arm that unloads the RSL arthrodesis so that fusion rates improve and secondary midcarpal arthritis decreases. Substantial increases in force following RSL fusion however can be seen at the scaphoid-trapezoid articulation in flexion (113% increase), the lunate-capitate articulation in extension (42% increase), the scaphoid-trapezoid articulation in radial deviation (40% increase), and the scaphoid-capitate articulation in ulnar deviation (225% increase). These increases in force at the midcarpal joint suggest an environment that promotes degenerative arthritis. Excision of the distal pole brought relief of the forces at two of these articulations (scaphoid-trapezoid in flexion and radial deviation). However, the forces at the lunate-capitate joint in extension and scaphoid-

capitate joint in ulnar deviation increased and remained the same, respectively, following RSL fusion with distal pole excision. The increase in force at the lunate-capitate joint following RSL fusion could explain the model's under-prediction of extension motion as it appears the capitate bone is losing motion at this articulation following scaphoidectomy and triquetrectomy. These findings also suggest that removal of the distal pole and/or triquetrum does not entirely relieve the forces induced by RSL fusion and that progressive arthritis is still a possibility in these areas of the midcarpal joint.

The linear tension-only expression used in COSMOSMotion, provided a means of quantifying the tensions in the ligaments during range of motion simulations. The scaphocapitate, radioscaphocapitate, and ulnocapitate ligament tensions were of interest in this experimental study. The triquetrum is the site of many ligamentous attachments, and removal of this carpal bone could transfer stresses from ligaments inserting on the triquetrum to the surrounding ligaments. Ligaments inserting on the triquetrum include the UT, DRC, TC, TH, DIC, LT, and PT ligaments, and all of these ligaments are destroyed when the triquetrum is excised. In addition to removing these ligaments, the extrinsic ligaments inserting on the scaphoid and lunate are also essentially non-functional following RSL fusion. These include the LRL, SRL, UL and SL ligaments. Excision of the scaphoid distal pole also eliminates constraint of the STT ligament. Considering all of the ligaments absent following RSL fusion, distal pole excision, and triquetral excision, it was not surprising to find ligament tension increases in three of the ligaments remaining that span the midcarpal joint. The extent to which these ligaments experienced an increase was quite alarming. Research of the literature provided little experimental insight into actual tensions developed in wrist ligaments, mostly due to their small size and difficulty in isolation. Stability of the wrist joint complex was also a concern prior to

conducting the experimental study, but the model showed no sign of being unstable following the two excisions.

Certain assumptions were implemented for the computational model of the wrist presented here. Firstly, the model represents one single wrist specimen which is assumed comparable to the studies in the literature, whereas experimental studies record larger sample sizes allowing more general statistical conclusions to be made. The specimen age (52yo) with no underlying pathologies is reasonable to assume as normal. Ligament *in-situ* strains are not reported for most structures in the wrist complex, and applications of normal strains (~2%) applied to the model ligaments caused deformation of the carpus and were thus not included. Stiffness values not reported in literature for specific ligaments were assigned as averages of similar ligaments stiffness values. This was considered a reasonable assumption given the large variations in stiffness values seen in the literature [32,53,62,74,75]. Linear behavior was also assumed for these structures which could overestimate their restraining role. Further, it was not possible to model all soft tissues present in the wrist, including skin and other forearm muscle tendons, nor was it possible to model the wrapping effect of ligaments and muscles. These structures would provide a restraining force to the bones of the carpus, and thus range of motion results in the model could be over-estimated. Ligament-bone overlap was visually inspected at each maximum position. Spanning ligaments entering bone interior was minimal with most intrusion occurring in flexion. Also, articular cartilage was not captured by CT imaging and was not modeled which could change joint surface anatomy. However, cartilage thickness variations over joint surfaces are typically such that the small differences from the underlying bone shape would not appreciably alter conclusions. Additionally, the exact cut plane of the scaphoid distal pole in the experiment is unknown. Visual inspection of the experimental radiographs (Figure

4.1-2B) after distal pole excision compared to the computational model with distal scaphoidectomy (Figure 4.2-8) provides a similar AP view. Therefore, while the precise cutting plane and angle was not quantified in the cadaver study, any difference in cut planes is not thought to have an effect on model range of motion predictions. Finally, one notable anatomical structure omitted from the wrist model is the TFCC. While the ligaments of this structure are included, the articular fibrocartilage disc and meniscal homologue were not captured by CT. The effects on ulnar deviation range of motion were seen in normal (intact) and triquetral excision results, as range of motion values for these states were over-estimated when compared to experimental results.

5. CONCLUSION

The human wrist is a complex organization of bones and tissue structures, consisting of multiple small joints whose interactions provide the wrist its great degree of mobility. Normal carpal mechanics rely on the complex interactions between the ligaments and carpal bone morphology. This makes wrist investigations increasingly prevalent and the need for cadaver specimens constant. With the cost and availability of cadavers for experimental testing presenting a challenge, computational modeling is becoming an attractive relief. Theoretical modeling and simulation techniques are, therefore, an important tool for musculoskeletal investigation and should be used to compliment cadaveric testing in solving wrist-related biomechanical problems.

The computational model presented here used 3D bony contact, ligamentous constraints, and muscle loading to drive joint function. It has demonstrated an ability to efficiently study joint range of motion and mechanics, as well as compute parameters that are difficult to capture experimentally. The software packages used for modeling are widely available, and the approach taken in this study reduces the need for proprietary software to analyze musculoskeletal joints. This technique is versatile and provides the ability to predict the behavior of injury or corrective procedures.

Validation of the model was conducted by simulating a cadaveric study by Pervaiz et al (2009), where wrist range of motion following RSL fusion was examined. The cadaveric

experimental setup was replicated in the SolidWorks environment, and the model was able to accurately predict the range of motion trends and most magnitudes for various surgical states following RSL fusion. In addition to replicating range of motion results, the model is able to predict parameters that are not easily obtained experimentally, such as magnitudes for midcarpal joint force and ligament tensions. The ability of the model to predict these additional parameters present an opportunity for the model to locate areas of concern following surgical alteration.

The computational model results are promising, however, further model refinements to the soft tissue constraints could greatly improve its accuracy and applicability. First, a better understanding of the mechanical properties of the ligaments of the wrist is needed. Ligament properties are varied and widespread across the literature, and cadaver experiments providing more detailed stiffness and *in situ* strains in wrist ligaments could increase model accuracy. Also, modeling the viscoelastic load-elongation behavior to the ligaments in COSMOSMotion would provide a more physiologic soft-tissue constraint to the model. Furthermore, ligaments and muscles in the model were represented as straight line vectors between origin and insertion points. The wrapping constraint of these soft-tissues was not included, and more attempts at modeling wrapping would benefit the model's physiologic accuracy. More specific to the wrist, the inclusion of the triangular fibrocartilage complex's cartilaginous disc and intricate interaction between the TFCC ligaments to the model could improve the model's prediction of ulnar deviation. Next generation models should also explore the inclusion of cartilage on the rigid body surfaces to provide a physiological smooth surface.

The ability of the current model to predict range of motion behavior in cadaver studies is encouraging. This model and modeling approach are expected to have value as a potential predictive clinical tool for patient-specific preoperative planning. Future applications range from

use in academia or the hospital, including further cadaveric investigations, patient specific biomechanical analysis, or implant design. The ability of the current model to obtain large amounts of data in a short amount of time make it extremely versatile, and the use of rigid body modeling should become more widespread in musculoskeletal research.

Literature Cited

1. COSMOSMotion Training Manual. Santa Monica, CA: Structural Research and Analysis Corporation; 2006.

2. MIMICS 12.0 Help Pages. Ann Arbor, MI: Insight Software Consortium; 2003.

3. An KN, Himeno S, Tsumura H, Kawai T, Chao EY. Pressure distribution on articular surfaces: application to joint stability evaluation. J Biomech. 1990;23(10):1013-1020.

4. An K, Berger RA, Cooney WPI. Biomechanics of the Wrist Joint. 1st ed. Springer; 1991.

5. Baratz M, Rosenwasser M, Adams B, Kozin S. Wrist Surgery: Tricks of the Trade. 1st ed. Thieme; 2006.

6. Barker TM, Kirtley C, Ratanapinunchai J. Calculation of multi-segment rigid body joint dynamics using MATLAB. Proc Inst Mech Eng H. 1997;211(6):483-487.

7. Benham MP, Wright DK, Bibb R. Modelling soft tissue for kinematic analysis of multi-segment human body models. Biomed Sci Instrum. 2001;37:111-116.

8. Berger RA. The ligaments of the wrist. A current overview of anatomy with considerations of their potential functions. Hand Clin. 1997 Feb;13(1):63-82.

9. Berger RA. The anatomy of the ligaments of the wrist and distal radioulnar joints. Clin. Orthop. Relat. Res. 2001 Feb;(383):32-40.

10. Berkhout MJ, Shaw MN, Berglund LJ, An KN, Berger RA, Ritt MJ. The Effect of radioscapholunate fusion on wrist movement and the subsequent effects of distal scaphoidectomy and triquetrectomy. Journal of Hand Surgery (European Volume). 2010 4

11. Brown RR, Fliszar E, Cotten A, Trudell D, Resnick D. Extrinsic and intrinsic ligaments of the wrist: normal and pathologic anatomy at MR arthrography with three-compartment enhancement. Radiographics. 1998 May;18(3):667-674.

12. Büchler P, Ramaniraka NA, Rakotomanana LR, Iannotti JP, Farron A. A finite element model of the shoulder: application to the comparison of normal and osteoarthritic joints. Clin Biomech (Bristol, Avon). 2002 Dec;17(9-10):630-639.

13. Carrigan SD, Whiteside RA, Pichora DR, Small CF. Development of a three-dimensional finite element model for carpal load transmission in a static neutral posture. Ann Biomed Eng. 2003 Jun;31(6):718-725.

14. Chao E. Graphic-based musculoskeletal model for biomechanical analyses and animation. Medical Engineering & Physics. 2003 4;25(3):201-212.

15. Chao EY, Armiger RS, Yoshida H, Lim J, Haraguchi N. Virtual interactive musculoskeletal system (VIMS) in orthopaedic research, education and clinical patient care. J Orthop Surg. 2:2-2.

16. Cheung J, Zhang M, Leung A, Fan Y. Three-dimensional finite element analysis of the foot during standing?a material sensitivity study. Journal of Biomechanics. 2005 5;38(5):1045-1054.

17. Cohen ZA, Henry JH, McCarthy DM, Mow VC, Ateshian GA. Computer simulations of patellofemoral joint surgery. Patient-specific models for tuberosity transfer. Am J Sports Med. 2003 Feb;31(1):87-98.

18. Connell D, Page P, Wright W, Hoy G. Magnetic Resonance Imaging of the Wrist Ligaments. Australasian Radiology. 2001 Nov;45(4):411-422.

19. Cooney WP, Garcia-Elias M, Dobyns J. Anatomy and mechanics of carpal instability. Surg Rounds Orthop. 1989;(3):15-24.

20. Cooney WP. The Wrist: Diagnosis and Operative Treatment. 1st ed. Mosby-Year Book; 1998.

21. Cooney W, Lucca M, Chao E, Linscheid R. The kinesiology of the thumb trapeziometacarpal joint. J Bone Joint Surg Am. 1981 Dec 1;63(9):1371-1381.

22. Couteau B, Mansat P, Estivalèzes E, Darmana R, Mansat M, Egan J. Finite element analysis of the mechanical behavior of a scapula implanted with a glenoid prosthesis. Clin Biomech (Bristol, Avon). 2001 Aug;16(7):566-575.

23. Delp SL, Loan JP. A graphics-based software system to develop and analyze models of musculoskeletal structures. Comput. Biol. Med. 1995 Jan;25(1):21-34.

24. Delp SL, Loan JP, Hoy MG, Zajac FE, Topp EL, Rosen JM. An interactive graphics-based model of the lower extremity to study orthopaedic surgical procedures. IEEE Trans Biomed Eng. 1990 Aug;37(8):757-767.

25. Drewniany JJ, Palmer AK, Flatt AE. The scaphotrapezial ligament complex: an anatomic and biomechanical study. J Hand Surg Am. 1985 Jul;10(4):492-498.

26. Ekenstam F. Anatomy of the Distal Radioulnar Joint. Clinical Orthopaedics. 1992;275:14-18.

27. Favre P, Snedeker JG, Gerber C. Numerical modelling of the shoulder for clinical applications. Philos Transact A Math Phys Eng Sci. 2009 May 28;367(1895):2095-2118.

28. Fischli S, Sellens R, Beek M, Pichora D. Simulation of extension, radial and ulnar deviation of the wrist with a rigid body spring model. Journal of Biomechanics. 2009 6;42(9):1363-1366.

29. Fisk GR. The Wrist. J Bone Joint Surg British. 1984;(66B):396-406.

30. Fisk JP, Wayne JS. Development and validation of a computational musculoskeletal model of the elbow and forearm. Ann Biomed Eng. 2009 Apr;37(4):803-812.

31. Fung Y. First Course in Continuum Mechanics. 3rd ed. Prentice Hall; 1993.

32. Garcia-Elias M, An K, Cooney III WP, Linscheid RL, Chao EY. Stability of the transverse carpal arch: An experimental study. The Journal of Hand Surgery. 1989 Mar;14(2, Part 1):277-282.

33. Garcia-Elias M, Lluch A, Ferreres A, Papini-Zorli I, Rahimtoola ZO. Treatment of radiocarpal degenerative osteoarthritis by radioscapholunate arthrodesis and distal scaphoidectomy. J Hand Surg Am. 2005 Jan;30(1):8-15.

34. Garner BA, Pandy MG. A Kinematic Model of the Upper Limb Based on the Visible Human Project (VHP) Image Dataset. Comput Methods Biomech Biomed Engin. 1999;2(2):107-124.

35. Gonzalez RV, Hutchins EL, Barr RE, Abraham LD. Development and evaluation of a musculoskeletal model of the elbow joint complex. J Biomech Eng. 1996 Feb;118(1):32-40.

36. van der Helm FC. Analysis of the kinematic and dynamic behavior of the shoulder mechanism. J Biomech. 1994 May;27(5):527-550.

37. van der Helm F. A finite element musculoskeletal model of the shoulder mechanism. Journal of Biomechanics. 1994 May;27(5):551-553, 555-569.

38. Herren DB, Ploeg H, Hertig D, Klabunde R. Modeling and finite element analysis of a new revision implant for the elbow. Clin. Orthop. Relat. Res. 2004 Mar;(420):292-297.

39. Hirokawa S. Three-dimensional mathematical model analysis of the patellofemoral joint. J Biomech. 1991;24(8):659-671.

40. Holzbaur KRS, Murray WM, Delp SL. A model of the upper extremity for simulating musculoskeletal surgery and analyzing neuromuscular control. Ann Biomed Eng. 2005 Jun;33(6):829-840.

41. Horii E, Garcia-Elias M, An K, Bishop A, Cooney W, Linscheid R, et al. Effect on force transmission across the carpus in procedures used to treat Kienb ck's disease. The Journal of Hand Surgery. 1990 May;15(3):393-400.

42. Ide T, Yamamoto Y, Tatsugi S. Validation study of the rigid body spring model using the metacarpophalangeal joint. Biomechanics in Orthopedics. 1992;:299-306.

43. Iwasaki N, Genda E, Barrance PJ, Minami A, Kaneda K, Chao EYS. Biomechanical analysis of limited intercarpal fusion for the treatment of Kienböck's disease: A three-dimensional theoretical study. Journal of Orthopaedic Research. 1998;16(2):256-263.

44. Kawai T, Takeuchi. A discrete method of limit analysis with simplified element. In: American Society of Engineers, International Conference on Computing in Civil Engineering. 1981.

45. Kwak SD, Blankevoort L, Ateshian GA. A Mathematical Formulation for 3D Quasi-Static Multibody Models of Diarthrodial Joints. Comput Methods Biomech Biomed Engin. 2000;3(1):41-64.

46. Kwak SD, Blankevoort L, Ateshian GA. A Mathematical Formulation for 3D Quasi-Static Multibody Models of Diarthrodial Joints. Comput Methods Biomech Biomed Engin. 2000;3(1):41-64.

47. Lengsfeld M.[1], Pressel T., Stammberger U. Lengths and lever arms of hip joint muscles: geometrical analyses using a human multibody model. Gait and Posture. 1997 Aug;6:18-26.

48. Li G, Gil J, Kanamori A, Woo SL. A validated three-dimensional computational model of a human knee joint. J Biomech Eng. 1999 Dec;121(6):657-662.

49. Li Z, Kota S. Virtual Prototyping and Motion Simulation with ADAMS. J. Comput. Inf. Sci. Eng. 2001;1(3):276-279.

50. Liacouras PC, Wayne JS. Computational modeling to predict mechanical function of joints: application to the lower leg with simulation of two cadaver studies. J Biomech Eng. 2007 Dec;129(6):811-817.

51. Lin H, Nakamura Y, Su F, Hashimoto J, Nobuhara K, Chao EYS. Use of virtual, interactive, musculoskeletal system (VIMS) in modeling and analysis of shoulder throwing activity. J Biomech Eng. 2005 Jun;127(3):525-530.

52. Manal K, Lu X, Nieuwenhuis MK, Helders PJM, Buchanan TS. Force transmission through the juvenile idiopathic arthritic wrist: a novel approach using a sliding rigid body spring model. J Biomech. 2002 Jan;35(1):125-133.

53. Mayfield JK. Patterns of injury to carpal ligaments. A spectrum. Clin. Orthop. Relat. Res. 1984 Aug;(187):36-42.

54. Mayfield JK, Johnson RP, Kilcoyne RF. The ligaments of the human wrist and their functional significance. The Anatomical Record. 1976;186(3):417-428.

55. McCombe D, Ireland DC, McNab I. Distal scaphoid excision after radioscaphoid arthrodesis. J Hand Surg Am. 2001 Sep;26(5):877-882.

56. Moojen TM, Snel JG, Ritt MJ, Venema HW, den Heeten GJ, Bos KE. Pisiform kinematics in vivo. J Hand Surg Am. 2001 Sep;26(5):901-907.

57. Moore KL, Agur AM, Dalley AF. Essential Clinical Anatomy, North American Edition (Point. Fourth Edition. Lippincott Williams & Wilkins; 2010.

58. Murray PM. Radioscapholunate arthrodesis. Hand Clin. 2005 Nov;21(4):561-566.

59. Nagy L, Büchler U. Long-term results of radioscapholunate fusion following fractures of the distal radius. The Journal of Hand Surgery: Journal of the British Society for Surgery of the Hand. 1997 Dec;22(6):705-710.

60. Netter FH. Atlas of Human Anatomy, Professional Edition. 5th ed. Saunders; 2010.

61. Novotny JE, Beynnon BD, Nichols CE. Modeling the stability of the human glenohumeral joint during external rotation. J Biomech. 2000 Mar;33(3):345-354.

62. Nowalk MD, Logan SE. Distinguishing Biomechanical Properties of Intrinsic and Extrinsic Human Wrist Ligaments. J. Biomech. Eng. 1991 Feb 0;113(1):85-93.

63. Palmer AK, Werner FW. The triangular fibrocartilage complex of the wrist--anatomy and function. J Hand Surg Am. 1981 Mar;6(2):153-162.

64. Patterson RM, Nicodemus CL, Viegas SF, Elder KW, Rosenblatt J. High-speed, three-dimensional kinematic analysis of the normal wrist. J Hand Surg Am. 1998 May;23(3):446-453.

65. Pervaiz K, Bowers WH, Isaacs JE, Owen JR, Wayne JS. Range of Motion Effects of Distal Pole Scaphoid Excision and Triquetral Excision After Radioscapholunate Fusion: A Cadaver Study. The Journal of Hand Surgery. 2009 5;34(5):832-837.

66. Pevny T, Rayan GM, Egle D. Ligamentous and tendinous support of the pisiform, anatomic and biomechanical study. The Journal of Hand Surgery. 1995 Mar;20(2):299-304.

67. Piazza SJ, Delp SL. Three-dimensional dynamic simulation of total knee replacement motion during a step-up task. J Biomech Eng. 2001 Dec;123(6):599-606.

68. Prendergast P. Finite element models in tissue mechanics and orthopaedic implant design. Clinical Biomechanics. 1997 Sep;12(6):343-366.

69. Raikova R. A general approach for modelling and mathematical investigation of the human upper limb. J Biomech. 1992 Aug;25(8):857-867.

70. Rohen JW, Yokochi C, Lütjen-Drecoll E. Color Atlas of Anatomy: A Photographic Study of the Human Body (Color Atlas of Anatomy. Sixth Edition. Lippincott Williams & Wilkins; 2006.

71. Rominger MB, Bernreuter WK, Kenney PJ, Lee DH. MR imaging of anatomy and tears of wrist ligaments. Radiographics. 1993 Nov;13(6):1233-1246.

72. Salvia P, Woestyn L, David JH, Feipel V, Van S, Jan S, et al. Analysis of helical axes, pivot and envelope in active wrist circumduction. Clin Biomech (Bristol, Avon). 2000 Feb;15(2):103-111.

73. Savelberg HH, Kooloos JG, Huiskes R, Kauer JM. Stiffness of the ligaments of the human wrist joint. J Biomech. 1992 Apr;25(4):369-376.

74. Schuind F, Cooney WP, Linscheid RL, An KN, Chao EY. Force and pressure transmission through the normal wrist. A theoretical two-dimensional study in the posteroanterior plane. J Biomech. 1995 May;28(5):587-601.

75. Schuind F, An K, Berglund L, Rey R, Cooney III WP, Linscheid RL, et al. The distal radioulnar ligaments: A biomechanical study. The Journal of Hand Surgery. 1991 Nov;16(6):1106-1114.

76. Taleisnik J. The ligaments of the wrist. J Hand Surg Am. 1976 Sep;1(2):110-118.

77. Taleisnik J. The Wrist. Churchill Livingstone; 1985.

78. Triolo RJ, Werner KN, Kirsch RF. Modeling the postural disturbances caused by upper extremity movements. IEEE Trans Neural Syst Rehabil Eng. 2001 Jun;9(2):137-144.

79. Viegas SF, Crossley M, Marzke M, Wullstein K. The fourth carpometacarpal joint. J Hand Surg Am. 1991 May;16(3):525-533.

80. Viegas SF, Patterson RM, Todd PD, McCarty P. Load mechanics of the midcarpal joint. J Hand Surg Am. 1993 Jan;18(1):14-18.

81. Viegas SF, Patterson R, Peterson P, Roefs J, Tencer A, Choi S. The effects of various load paths and different loads on the load transfer characteristics of the wrist. The Journal of Hand Surgery. 1989 May;14(3):458-465.

82. Viegas SF, Patterson RM, Hokanson JA, Davis J. Wrist anatomy: Incidence, distribution, and correlation of anatomic variations, tears, and arthrosis. The Journal of Hand Surgery. 1993 May;18(3):463-475.

83. Watanabe Y, Shiba N, Matsuo S, Higuchi F, Tagawa Y, Inoue A. Biomechanical study of the resurfacing hip arthroplasty: finite element analysis of the femoral component. J Arthroplasty. 2000 Jun;15(4):505-511.

84. Wismans J, Veldpaus F, Janssen J, Huson A, Struben P. A three-dimensional mathematical model of the knee-joint. J Biomech. 1980;13(8):677-685.

85. Wu G, Vanderhelm F, Dirkjanveeger H, Makhsous M, Vanroy P, Anglin C, et al. ISB recommendation on definitions of joint coordinate systems of various joints for the reporting of human joint motion-Part II: shoulder, elbow, wrist and hand. Journal of Biomechanics. 2005 5;38(5):981-992.

86. Zhang M, Mak AF, Roberts VC. Finite element modelling of a residual lower-limb in a prosthetic socket: a survey of the development in the first decade. Med Eng Phys. 1998 Jul;20(5):360-373.

Appendix A

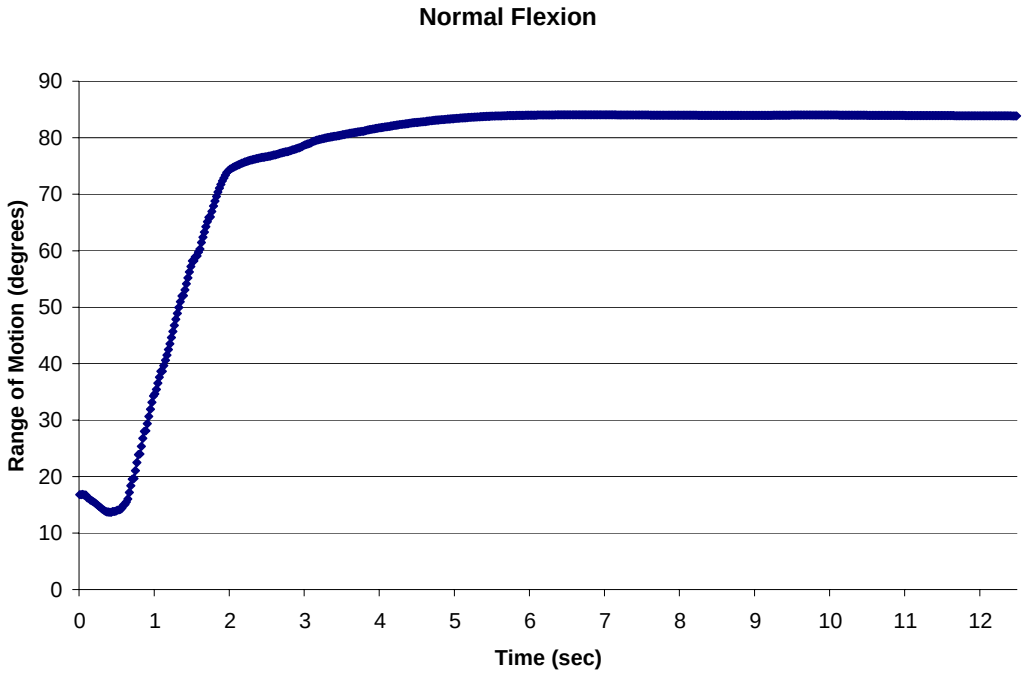
Normal Flexion
Range of Motion (degrees)
0
10
20
30
40
50
60
70
80
90
0
1
2
3
4
5
6
7
8
9
10
11
12
Time (sec)

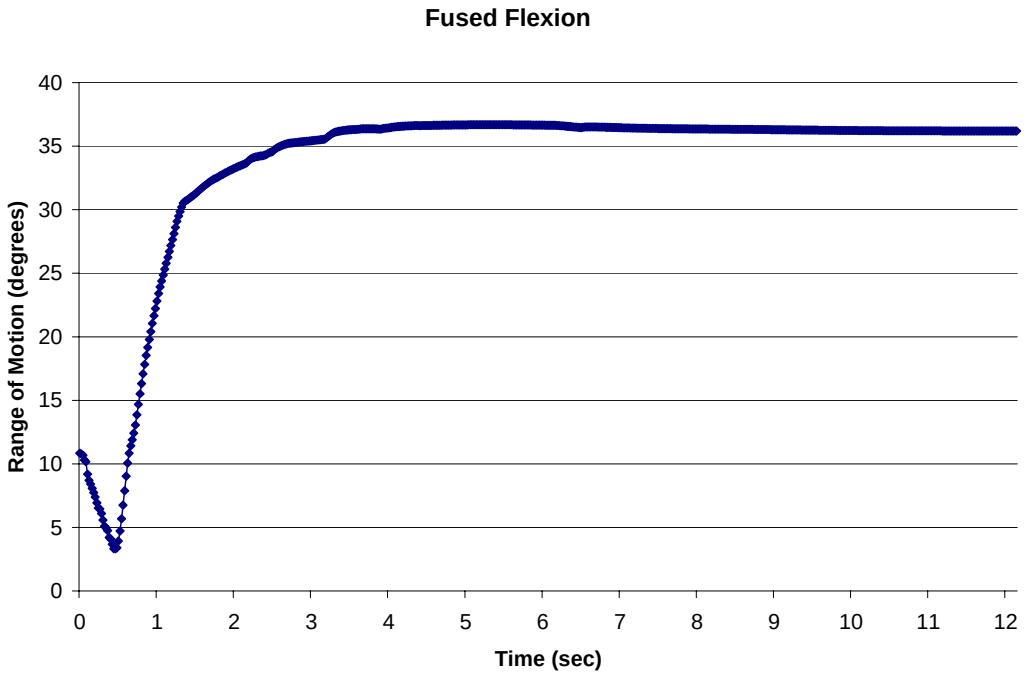
Fused Flexion
Range of Motion (degrees)
0
5
10
15
20
25
30
35
40
0
1
2
3
4
5
6
7
8
9
10
11
12
Time (sec)

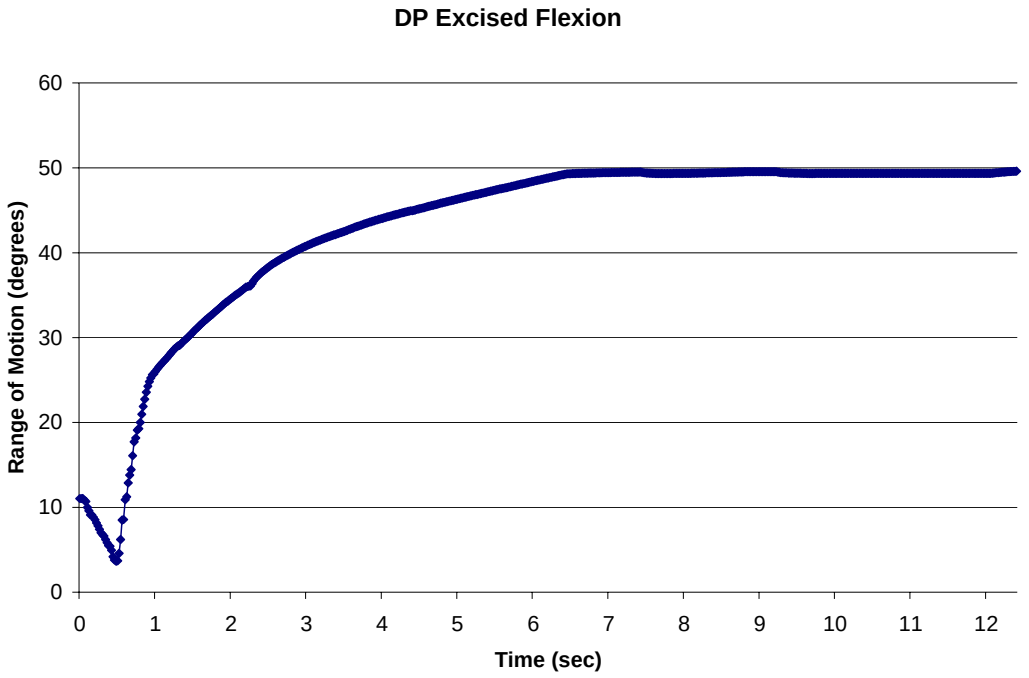
DP Excised Flexion
Range of Motion (degrees)
60
50
40
30
20
10
0
0 1 2 3 4 5 6 7 8 9 10 11 12
Time (sec)

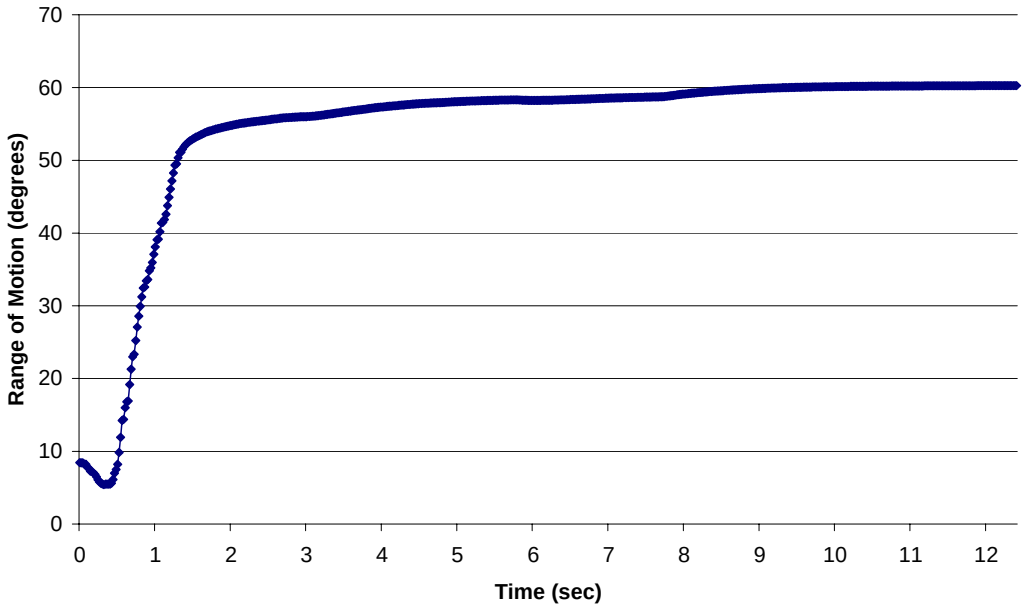
Tri Excised Flexion
Range of Motion (degrees)
70
60
50
40
30
20
10
0
0 1 2 3 4 5 6 7 8 9 10 11 12
Time (sec)

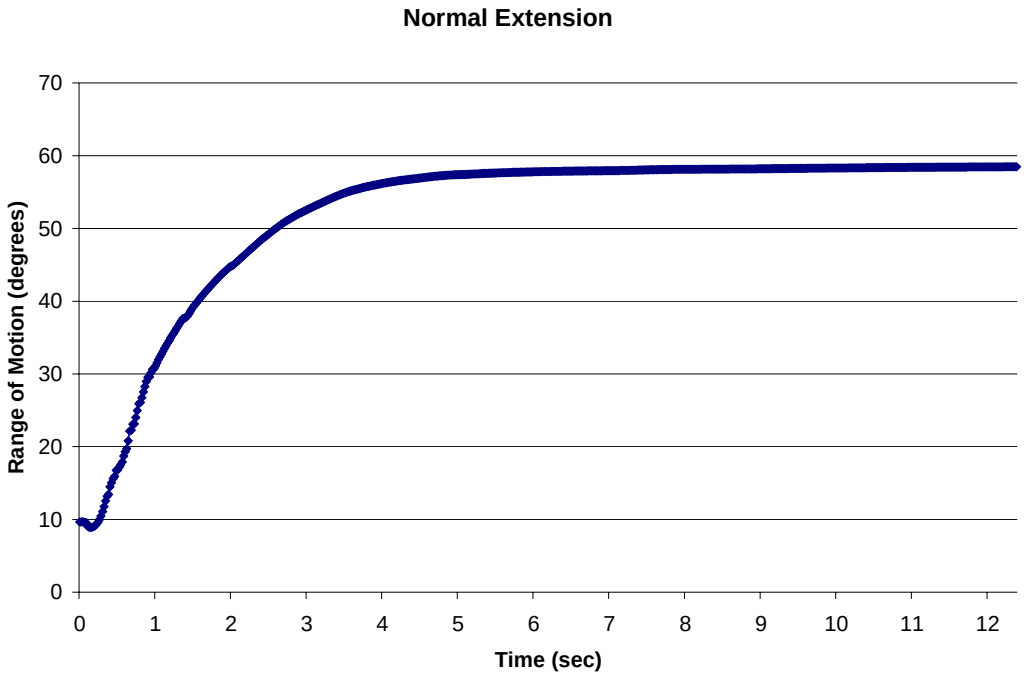
Normal Extension
Range of Motion (degrees)
70
60
50
40
30
20
10
0
0 1 2 3 4 5 6 7 8 9 10 11 12
Time (sec)

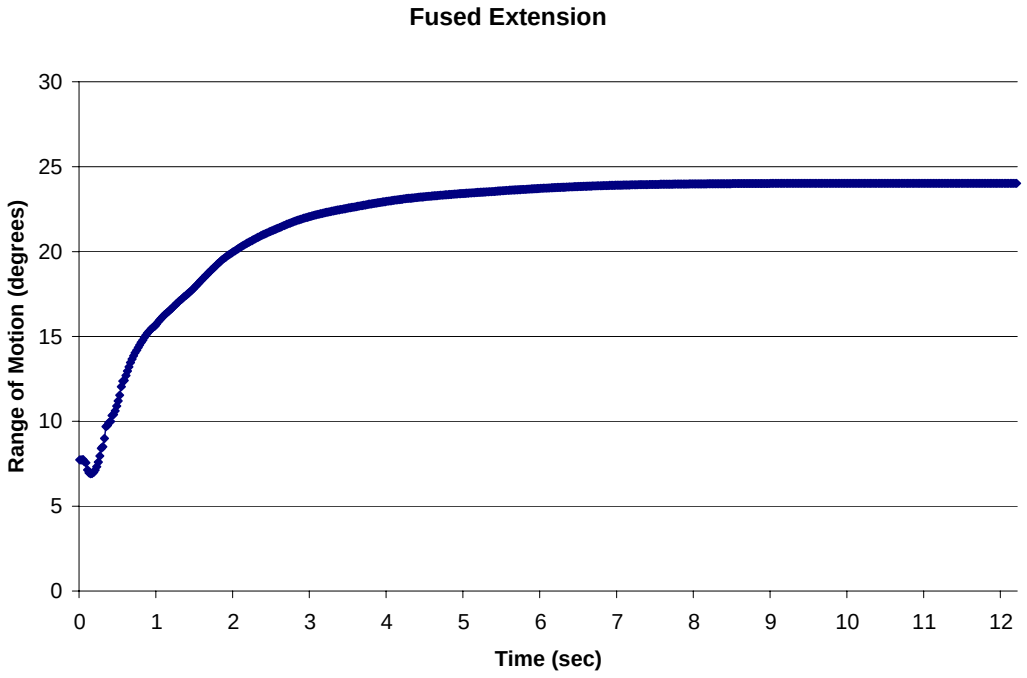
Fused Extension
Range of Motion (degrees)
30
25
20
15
10
5
0
0 1 2 3 4 5 6 7 8 9 10 11 12
Time (sec)

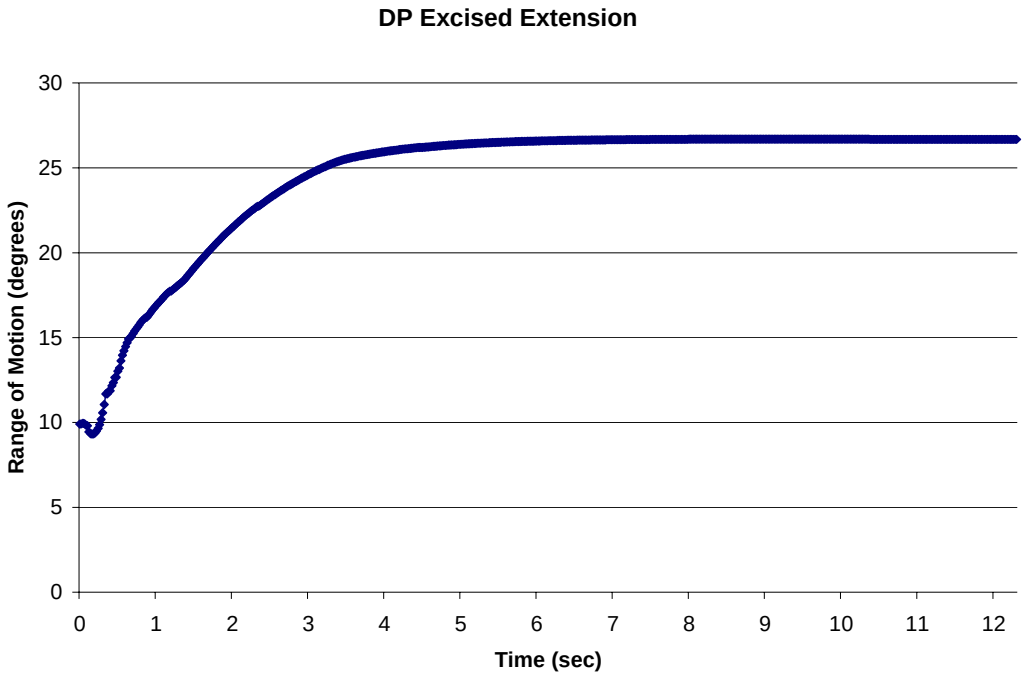
DP Excised Extension
Range of Motion (degrees)
30
25
20
15
10
5
0
0 1 2 3 4 5 6 7 8 9 10 11 12
Time (sec)

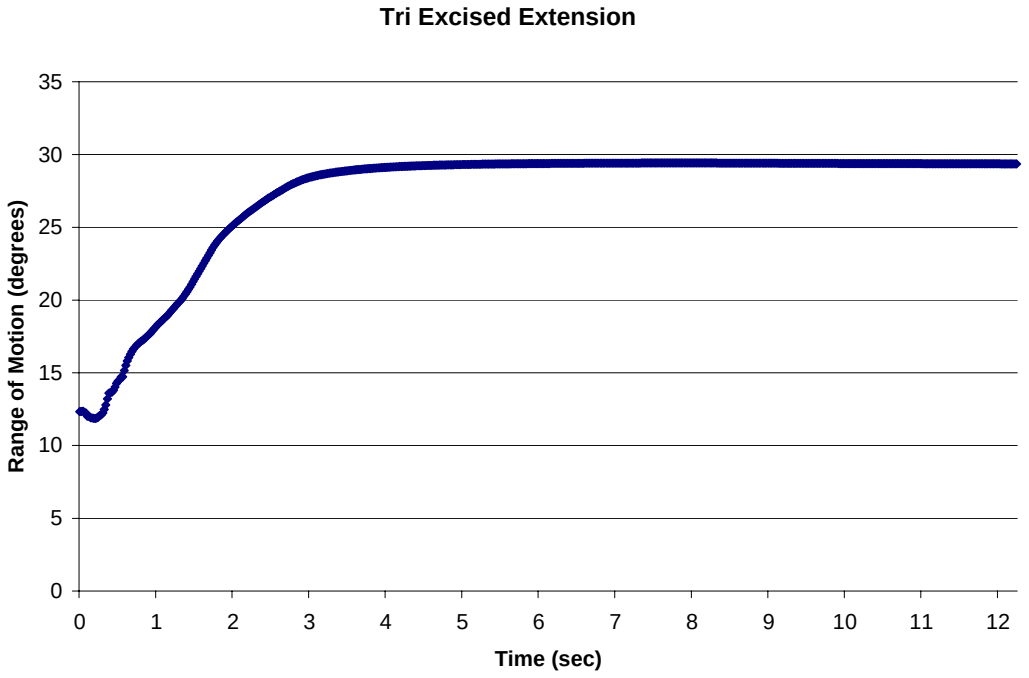
Tri Excised Extension
Range of Motion (degrees)
35
30
25
20
15
10
5
0
0 1 2 3 4 5 6 7 8 9 10 11 12
Time (sec)

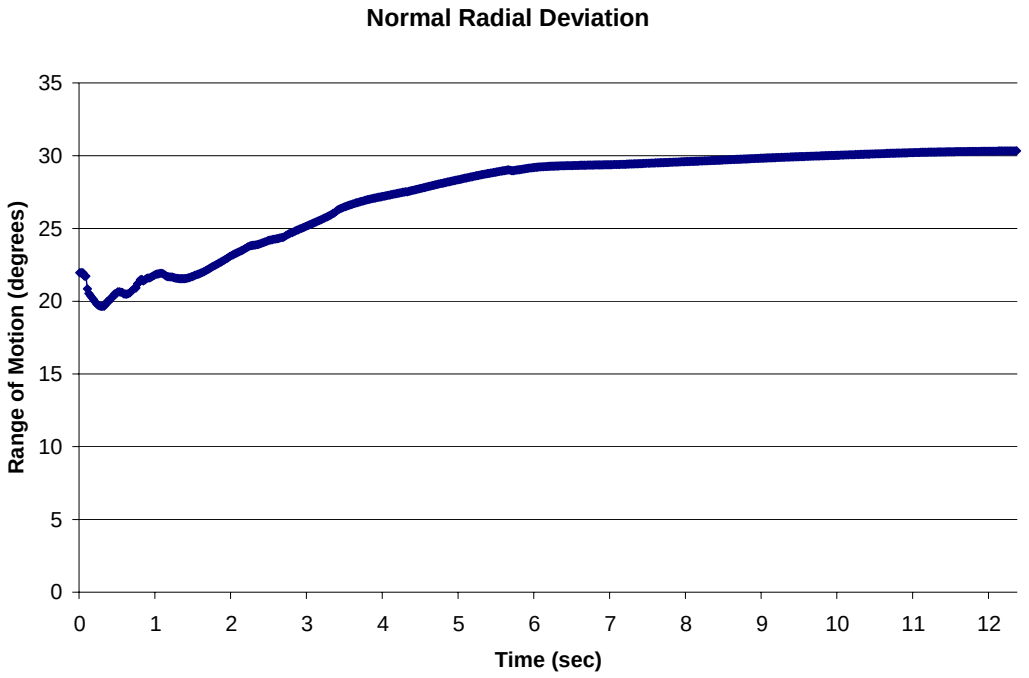
Normal Radial Deviation
Range of Motion (degrees)
35
30
25
20
15
10
5
0
0 1 2 3 4 5 6 7 8 9 10 11 12
Time (sec)

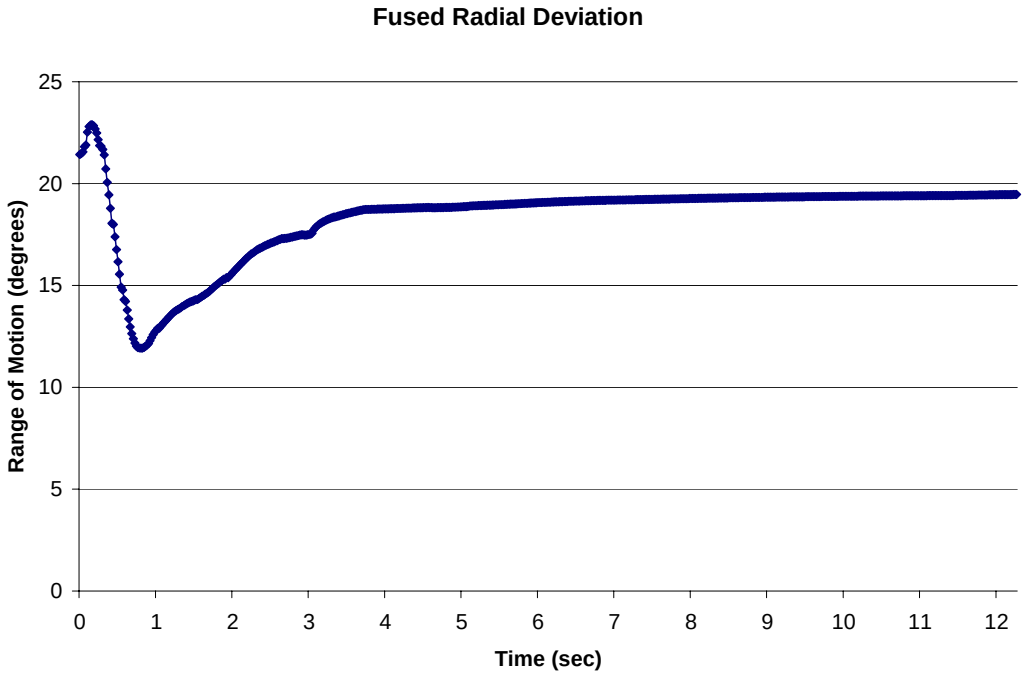
Fused Radial Deviation
Range of Motion (degrees)
25
20
15
10
5
0
0 1 2 3 4 5 6 7 8 9 10 11 12
Time (sec)

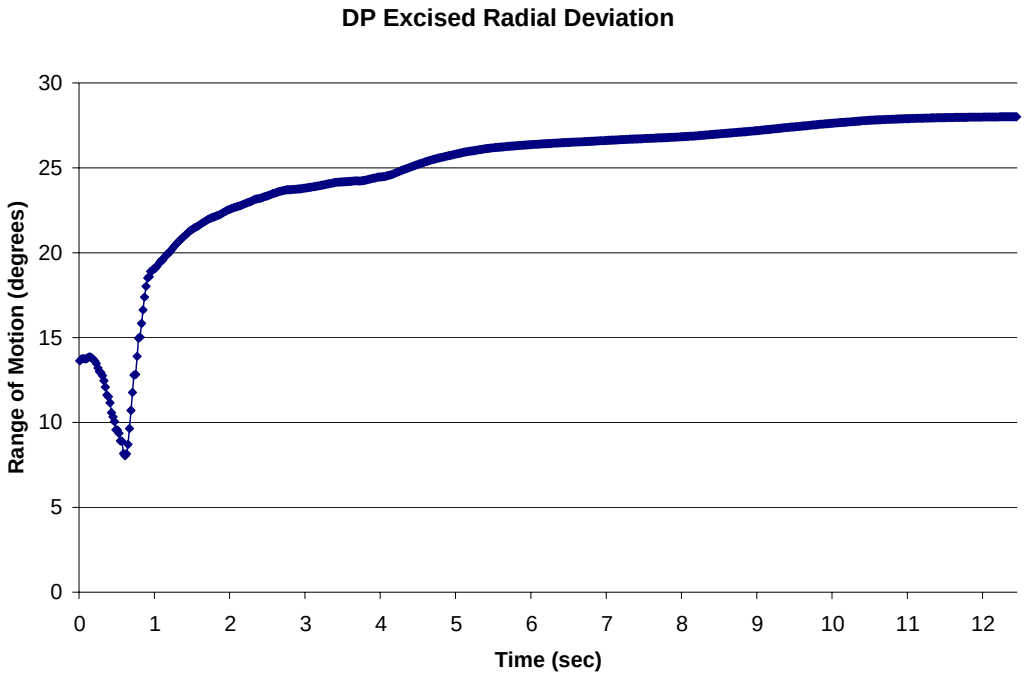
DP Excised Radial Deviation
Range of Motion (degrees)
30
25
20
15
10
5
0
0 1 2 3 4 5 6 7 8 9 10 11 12
Time (sec)

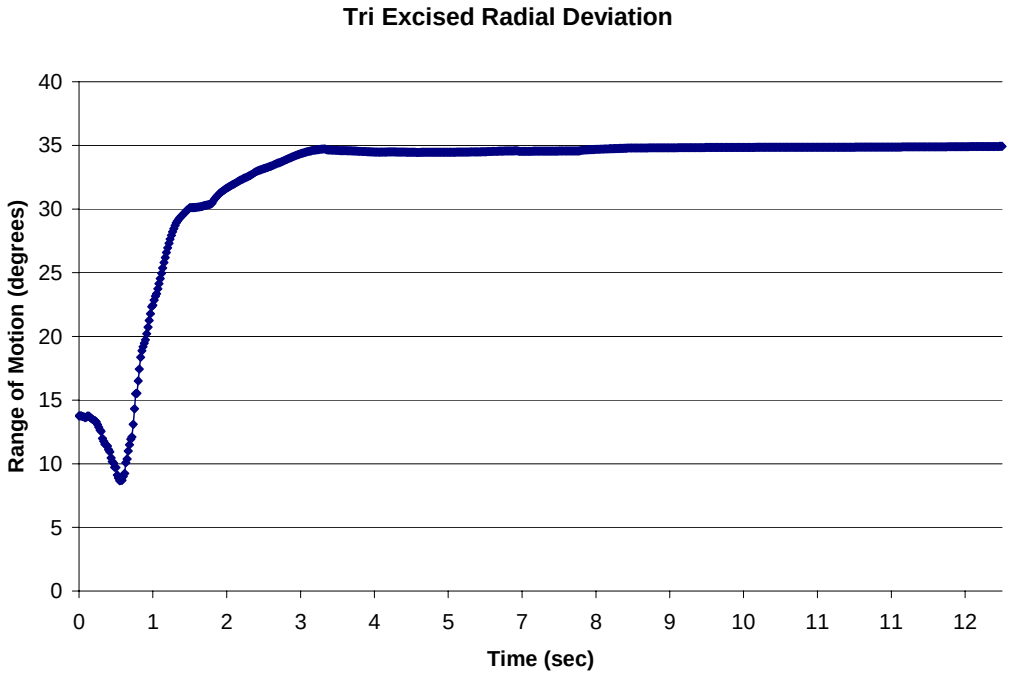
Tri Excised Radial Deviation
Range of Motion (degrees)
40
35
30
25
20
15
10
5
0
0 1 2 3 4 5 7 8 9 10 11 11 12
Time (sec)

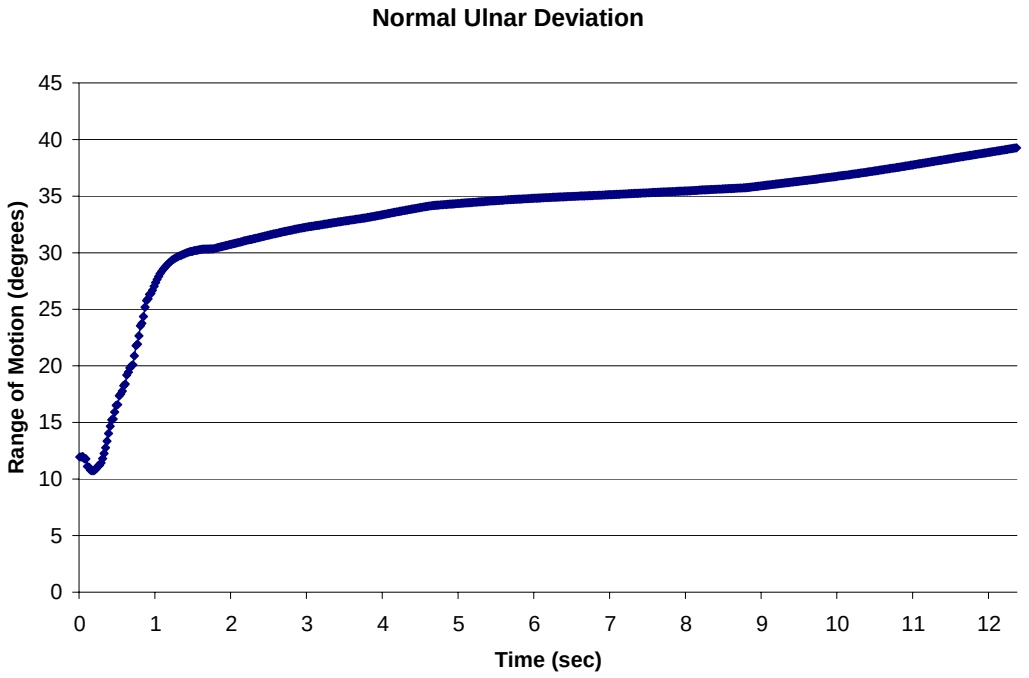
Normal Ulnar Deviation
Range of Motion (degrees)
45
40
35
30
25
20
15
10
5
0
0
1
2
3
4
5
6
7
8
9
10
11
12
Time (sec)

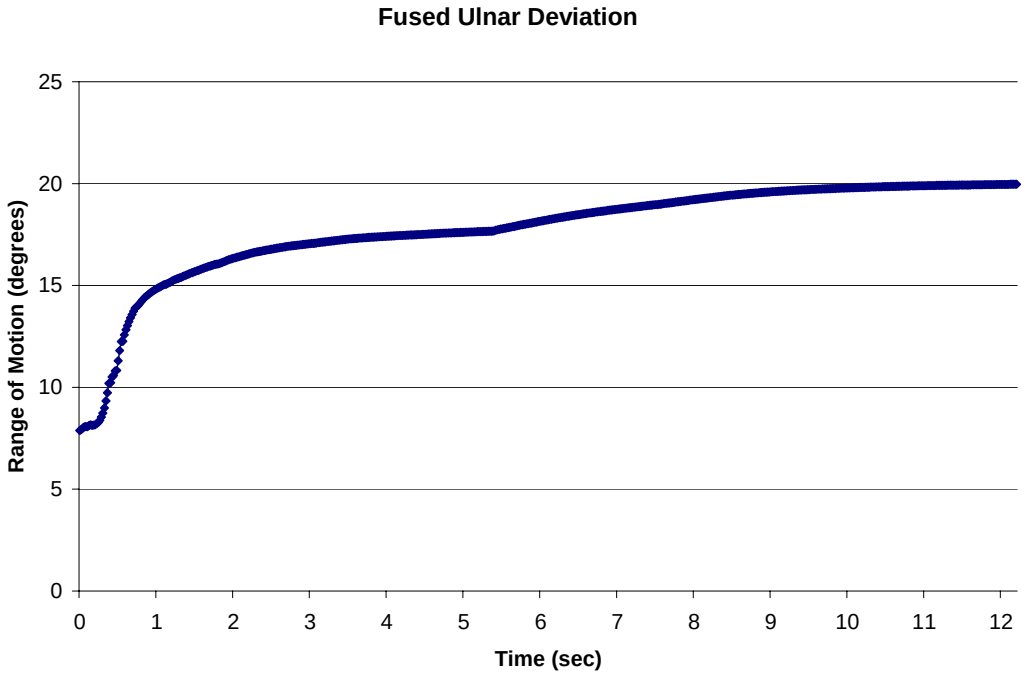
Fused Ulnar Deviation
Range of Motion (degrees)
25
20
15
10
5
0
0
1
2
3
4
5
6
7
8
9
10
11
12
Time (sec)

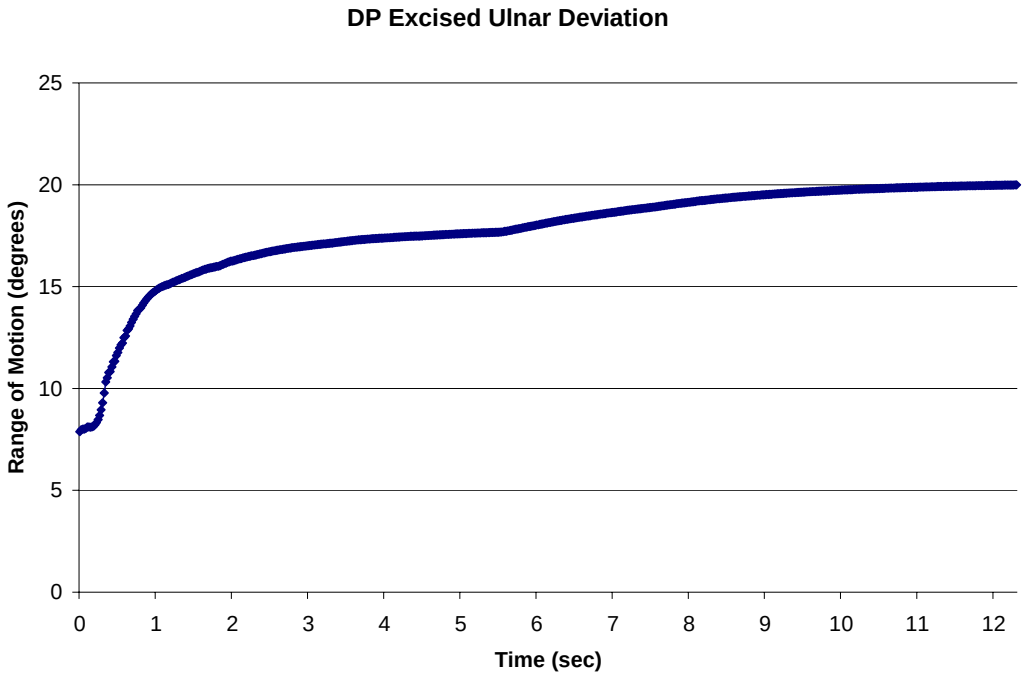
DP Excised Ulnar Deviation
Range of Motion (degrees)
25
20
15
10
5
0
0 1 2 3 4 5 6 7 8 9 10 11 12
Time (sec)

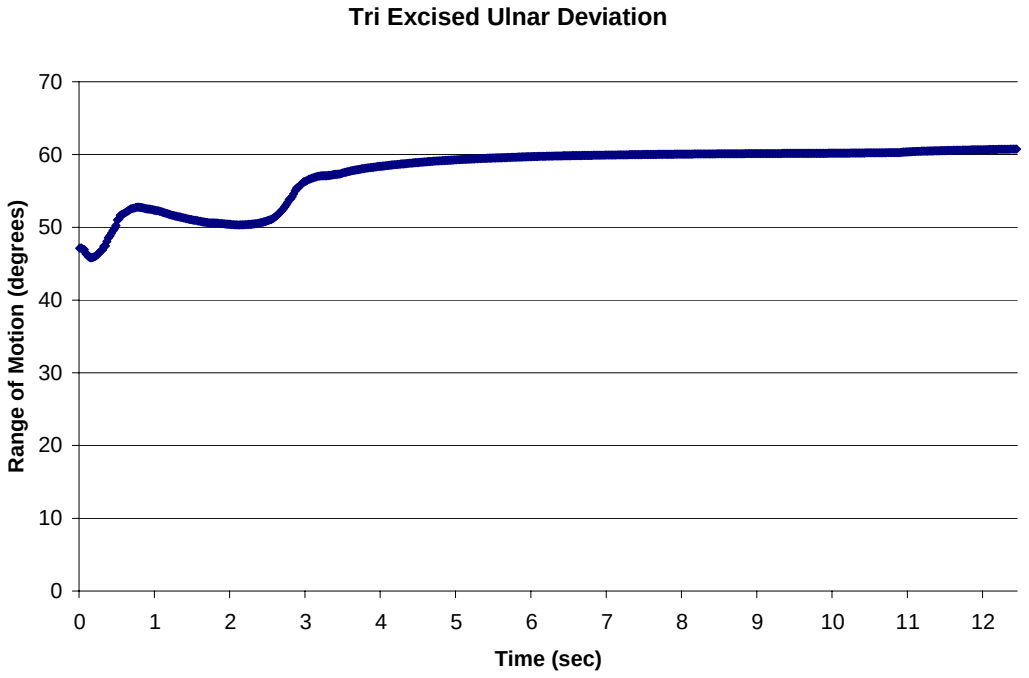
Tri Excised Ulnar Deviation
Range of Motion (degrees)
70
60
50
40
30
20
10
0
0 1 2 3 4 5 6 7 8 9 10 11 12
Time (sec)

VITA

Benjamin Judson Majors was born and raised in Franklin, Tennessee, just outside of Nashville. He attended Centennial High School, where he excelled in sciences and athletics. During high school, Ben's accomplishments included being awarded Eagle Scout and competing on the state high school swim team for four consecutive years. Upon graduation in May of 2002, he was accepted and enrolled at Clemson University where he studied mechanical engineering. He interned at Honeywell Inc. in Greer, SC for two semesters during college, where he worked with gas turbine engines. In 2007, Ben graduated with a Bachelor of Science degree in mechanical engineering with a minor in business administration. Following graduation, Ben lived in upstate South Carolina and worked as a junior project engineer for Techtronic Industries for eight months before deciding to return to school. In the fall of 2008, he moved to the Richmond, VA area and was enrolled in the Master of Science program at Virginia Commonwealth University to pursue his interests in biomedical engineering. Portions of this work were presented at the summer 2010 meeting of the Virginia Academy of Science.